The Neutron-Proton Analyzing Power at $E_n = 7.6$ and 12 MeV and the πNN Coupling Constant

by

Richard T. Braun

Department of Physics
Duke University

Date: _____

Approved:

_____
Werner Tornow, Supervisor

_____
Al Goshaw

_____
Berndt Müller

_____
Richard Walter

_____
Henry Weller

Dissertation submitted in partial fulfillment of
the requirements for the degree of
Doctor of Philosophy in the Department of Physics
in the Graduate School of Duke University

1998

ABSTRACT

(Physics – Nuclear)

The Neutron-Proton Analyzing Power at $E_n = 7.6$ and 12 MeV and the πNN Coupling Constant

by

Richard T. Braun

Department of Physics
Duke University

Date: _____

Approved:

_____
Werner Tornow, Chair

_____
Al Goshaw

_____
Berndt Müller

_____
Richard Walter

_____
Henry Weller

An abstract submitted in partial fulfillment of
the requirements for the degree of
Doctor of Philosophy in the Department of Physics
in the Graduate School of Duke University

1998

The Neutron-Proton Analyzing Power at $E_n = 7.6$ and 12 MeV and the πNN Coupling Constant

by

Richard T. Braun

0.1 Abstract

A series of measurements of the analyzing power, $A_y(\theta)$, for neutron-proton (np) scattering at incident neutron energies of 7.6 and 12 MeV has been performed at the Triangle Universities Nuclear Laboratory (TUNL). The experimental setup is described as well as the data sorting and techniques for the correction of the various background and multiple scattering contributions. Particular attention is given to the correction for multiple scattering involving carbon inside the neutron detectors. The results are given in comparison with predictions made by modified versions of the Bonn B nucleon-nucleon (NN) potential model. The relevance of the data to the determination of the charged pion nucleon-nucleon (πNN) coupling constant, $g^2_{\pi^\pm}/4\pi$, is shown.

Acknowledgements

First and foremost I would like to thank my advisor, Dr. Werner Tornow, without whose confidence and patience this work would never have been completed. For providing the theoretical models presented in this thesis, as well as explaining the results and their implications, I would like to thank Dr. Ruprecht Machleidt. For providing a n-^{12}C phase-shift analysis which extended the range and accuracy of my Monte-Carlo corrections, I would like to thank Dr. Zhenpeng Chen. For providing the calculated observables predicted by the CD-Bonn phase shifts using the Nijmegen code, I wish to thank Dr. Mart Rentmeester. And for many late-night discussions on the np analysis, as well as many other lengthy topics, I am indebted to Dr. Gary Weisel. Experimental work in nuclear physics is a group effort, and to that end I would like to thank the members of the Neutron Time-of-Flight (NTOF) group who assisted me in taking my data. The group at the time of my experiment consisted of Dr. Richard Walter, Dr. Calvin Howell, Dr. Ross Setze, Dr. Dinko González Trotter, Frank Salinas, Chris Roper and Dr. Branko Vlahovic. I would also like to thank the technical staff at TUNL for keeping things in working order, despite my best efforts to break things: Paul Carter, John Dunham, Sidney Edwards and Patrick Mulkey. And most of all, I wish to thank my parents. Without their constant support and encouragement, I never would have made it to this point.

Richard T. Braun

Duke University
February 1998

Contents

List of Figures

List of Tables

Chapter 1

Theory

1.1 Overview

Before 1988 it was thought that the coupling constants for the charged and neutral pions were well known. The values $g^2_{\pi^o}/4\pi = 14.52 \pm 0.40$ obtained by Kroll [Kro81] from pp scattering and $g^2_{\pi^\pm}/4\pi = 14.28 \pm 0.18$ obtained by Koch and Pietarinen [Koc80] from $\pi^\pm p$ scattering were used in potential models without question. This changed in 1988 when the Nijmegen group published the result of their reanalysis of all pp scattering data below 350 MeV [Sto88]. The value they determined, $g^2_{\pi^o}/4\pi = 13.1 \pm 0.1$, was significantly lower than the previously accepted value.

The high accuracy of the pp scattering database allows for the pp phase shifts (and the neutral pion coupling constant) to be fixed to a high degree of accuracy. For the charged coupling constant, the question is more difficult. The np data are not as high quality as the pp data. Additionally, calculations using modern meson-exchange potentials have shown that some of the most basic nuclear properties cannot be predicted correctly anymore using the new lower value of the charged pion coupling constant.

It is proposed that the low-energy np vector analyzing power, $A_y(\theta)$, can provide a sensitive probe to the value of the charged pion coupling constant. After the measurements

described in this thesis were completed, sensitivity studies were done by Machleidt [Mac96a] using a modified version of the Bonn B nucleon-nucleon (NN) potential model to determine the amount of this sensitivity. From these studies it seems that an accurate measurement of $A_y(\theta)$ should provide constraints on the value of the charged πNN coupling constant.

1.2 Nucleon-Nucleon Potential

In order to determine the form of the nuclear interaction, it is necessary to describe those features which are empirically known. These features include 1) the short-range of the force, 2) a "range-dependence" characterized by short, intermediate and long-range behaviors, including a short-range repulsion and an intermediate-range attraction, 3) a spin-orbit component and 4) a tensor component. The nuclear force would then have a form described by the following equation:

$$V(r) = V_c(r) + V_{LS}(r)\ \mathbf{L}\cdot\mathbf{S} + V_{SS}(\vec{\sigma}_1\cdot\vec{\sigma}_2) + V_T(r)\ S_{12}, \tag{1.1}$$

where V_c is the central term, V_{LS} is the spin-orbit term, V_{SS} is the spin-spin term and V_T is the tensor term with the tensor operator, S_{12}, given by

$$S_{12} = 3(\sigma_{\mathbf{1}}\cdot\hat{\mathbf{r}})(\sigma_{\mathbf{2}}\cdot\hat{\mathbf{r}}) - \sigma_{\mathbf{1}}\cdot\sigma_{\mathbf{2}}. \tag{1.2}$$

Today it is believed that quantum chromodynamics (QCD) provides the true underlying theory of nuclear interactions. However due to continuing difficulties in calculating observables with QCD, particularly in the low-energy regime, meson-exchange models of the nuclear interaction continue to play an important role. The theory of meson interaction dates back to Yukawa [Yuk35] who proposed an exchange model similar in form to quantum electrodynamics (QED) with the force mediated by particles of nonzero mass. This model was described in the same terms as QED, with interactions treated by perturbation theory and graphically described by Feynman diagrams (see Fig. 1.1). That the nuclear force could be described by perturbation theory, where in contrast to QED the coupling constants are

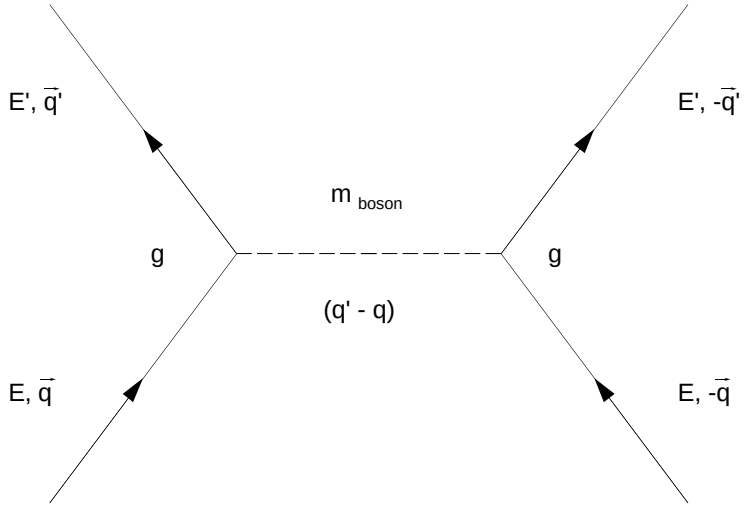

Figure 1.1: Feynman diagram for one-boson exchange in NN scattering in c-m frame. Solid lines denote nucleons, the dashed line a boson of mass $\mathrm{m_{boson}}$.

large, is answered by the fact that the long and intermediate range interactions contain only a finite number of terms. Only at short ranges do interactions of increasing order become divergent, and at this range the meson-exchange theory is expected to break down. At short ranges a phenomenological vertex form factor was introduced to account for the short-range behavior of the nuclear force. Thus in analogy to QED, the solution to the wave equation for meson-exchange theory is the following:

$$\phi = \frac{g}{4\pi}\frac{e^{-\frac{mc}{\hbar}r}}{r} \tag{1.3}$$

where g is the coupling constant which measures the strength of the interaction. This exponential solution falls off more rapidly than $\frac{1}{r}$, providing a short-range force dependent on the mass of the exchanged particle.

Since then many theoretical models have been developed incorporating meson exchange to various degrees while also parameterizing various parts of the interaction potential. Most fall into two types: those based on dispersion theory, as typified by the Paris potential [Lac80], and those based on field theory, typified by the Bonn potential [Mac87]. The Bonn potential represents the most extensive field-theoretical potential based on meson

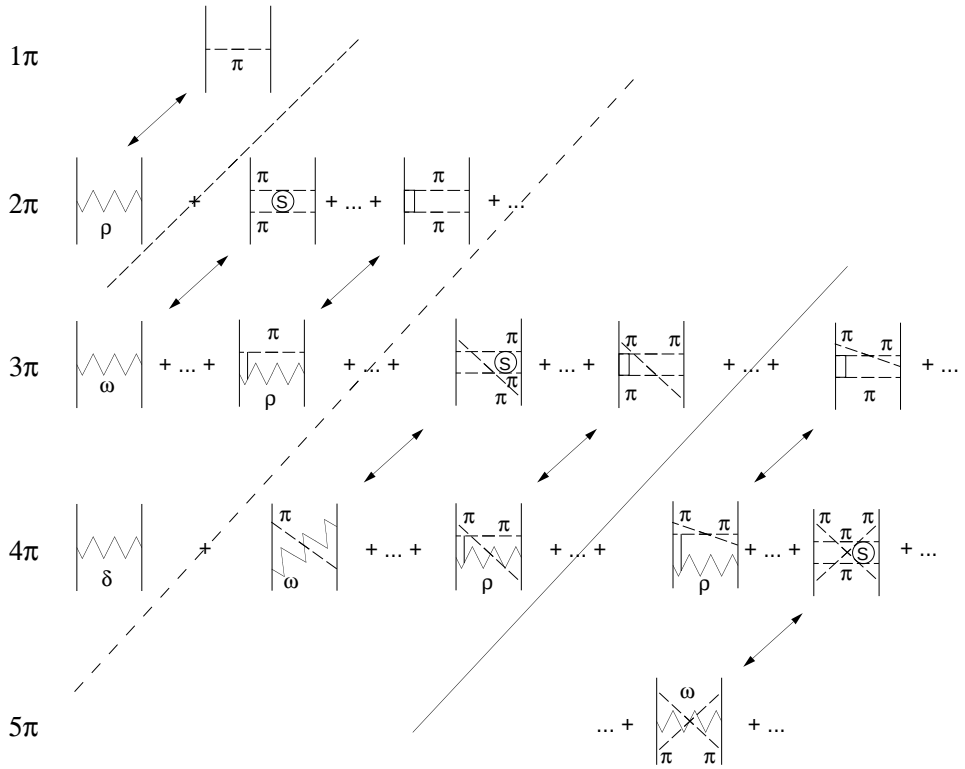

Figure 1.2: Meson-exchange diagrams for the NN interaction. Diagrams above and to the left of the solid line are considered in the full Bonn NN potential. The arrows point to terms that should be grouped together for quicker convergence.

exchange. It includes single-meson exchanges between nucleons as well as multiple-meson exchanges such as the 2π and 3π exchanges. Fig. 1.2 shows a condensed list of the exchange terms included in the full Bonn potential. The diagonal arrows represent terms which converge more quickly when calculated together rather than separately. All exchanges above and to the left of the solid line are included in the full Bonn NN potential. All contributions to the right of the dashed line are considered as providing negligible contributions to the interaction.

The attractiveness of this field-theoretical approach lies in its lack of free parameters. The meson masses and coupling constants are, for the most part, well determined by experiment and cannot be "tuned" to fit the data. The potential is fixed on and off

the energy shell by the number of irreducible diagrams it contains. Further it can be used to calculate interactions in many-body situations and allows for inelastic NN scattering [Mac89].

Machleidt has parameterized the full Bonn potential into several one-boson exchange potentials (OBEP) which lend themselves more readily to investigating specific aspects of the nuclear force. Here the multiple-meson exchanges are modeled in terms of the exchange of single mesons (including the $\pi, \eta, \rho, \omega, \delta$). In addition, to provide the intermediate attraction of the nuclear force, a "fictitious" scalar-isoscalar meson of approximately 500 MeV mass, the σ, is included. This σ meson represents a parameterization of the 2π-exchange and is much simpler to calculate than the actual 2π term. The mass and coupling constant of this meson can be adjusted to provide the best fit to the np data. Machleidt has parameterized 3 such OBE potentials, called Bonn A, Bonn B, and Bonn C, each using slightly different values for the πNN coupling constant as well as different values for the cut-off parameter, Λ_π, in the pion form factors, giving different values for the % D-state contribution to the deuteron, P_D.

1.3 Pion Nucleon-Nucleon Coupling Constant

One of the most basic parameters in a meson-exchange based model of the nuclear interaction is the pion nucleon-nucleon coupling constant. This constant determines the strength of the interaction between the pion and nucleon at their intersection in the Feynman diagram (see Fig. 1.1). The pion, the lightest meson, provides the dominant contribution to the long-range part of the nuclear force. The pseudoscalar pion also contributes heavily to the tensor component of the nuclear force. Due to the large spatial extent of the deuteron, the pion provides the dominant contribution to the nuclear force responsible for the observed properties of the deuteron.

The pion exists as an isoscalar triplet, the three species differentiated by their charges as well as their isospin projection. The pion masses are well known, the neutral pion (π^0)

		Before 1987 (Koch & Pietarinen)	Present (Nijmegen, Arndt)
$\pi^{\pm}$	$g^2_{\pi^{\pm}}/4\pi$	14.28 ± 0.18	13.54 ± 0.05
	$f^2_{\pi^{\pm}}$	0.079 ± 0.001	0.0748 ± 0.0007

		Before 1987 (Kroll)	Present (Nijmegen, Arndt)
π^0	$g^2_{\pi^o}/4\pi$	14.52 ± 0.40	13.47 ± 0.11
	$f^2_{\pi^o}$	0.080 ± 0.002	0.0745 ± 0.0006

Table 1.1: Pion coupling constants before and after Nijmegen analysis.

having a mass of 134.974 MeV and the two charged pions ($\pi^{\pm}$) each having a mass of 139.568 MeV. Since the early 1980's it had been thought that the coupling constants for the pions were also well known. The value for the neutral pion coupling constant had been determined by Kroll [Kro81] from pp data to be $g^2_{\pi^o}/4\pi = 14.52 \pm 0.40$ ($f_{\pi^o} = 0.080 \pm 0.002$), while the value for the charged pion coupling constant as determined by Koch and Pietarinen [Koc80] from $\pi^{\pm}p$ data was given as $g^2_{\pi^{\pm}}/4\pi = 14.28 \pm 0.18$ ($f_{\pi^{\pm}} = 0.079 \pm 0.001$).

It should be noted that in the literature, two forms of the coupling constant are commonly used. These two forms are the pseudovector coupling constant, f_π, and the pseudoscalar coupling constant, $g^2_\pi/4\pi$. The relationship between the two forms is given by:

$$f^2_{NN\pi} = \left(\frac{m_\pi}{2M}\right)^2 g^2_{NN\pi}, \tag{1.4}$$

where m_π is the mass of the pion (charged or neutral as the case may be) and M is the averaged nucleon mass. This relation holds only for the on-shell case. In the following discussion, when a value is given for the coupling constant, both forms will be shown.

The situation changed in 1987 when the Nijmegen group [Ber87] performed a reanalysis of all pp scattering data below 350 MeV and from this determined a lower value for the $g^2_{\pi^o}/4\pi$ coupling constant than had previously been accepted. Subsequent reanalysis by the Nijmegen group of all scattering data, both pp and np, confirmed this lower value for the neutral coupling constant as $g^2_{\pi^o}/4\pi = 13.47 \pm 0.11$ ($f_{\pi^o} = 0.0745 \pm 0.0006$). This value was later verified in an independent analysis by the VPI group [Arn90]. Fears of a large

charge-independence breaking were soon dispelled when the Nijmegen group analyzed the np scattering data over the same energy range and from that determined a lower value for the charged coupling constant as well. The current value for the charged pion coupling constant as determined by the Nijmegen group is $g^2_{\pi^\pm}/4\pi = 13.54 \pm 0.05$ ($f_{\pi^\pm} = 0.0748 \pm 0.0007$). Both the old and new values are summarized in Table 1.1.

The new values differ significantly ($\sim$6%) from the older version, and this difference has profound implications for our understanding of the nuclear force.

1.3.1 Nijmegen Phase-Shift Analysis

The Nijmegen phase-shift analysis considered the energy range from 0–350 MeV. In their analysis, the interaction is divided into "short" and "long" range parts, with the boundary at r = 1.4 fm. Below this range for waves with total angular momentum of J $\leq$ 4, energy-dependent square-well potentials are constructed; higher partial waves are suppressed by the centrifugal barrier. For the long-range part all partial waves are described by an electromagnetic potential and a nuclear potential, the latter of which contains the one-pion exchange (OPE) tail and the long-range heavy-boson exchange of the Nijmegen potential. The local OPE potential is given by

$$V_{OPE}(f_\pi, m_\pi) = \frac{f_\pi^2}{3}\left(\frac{m_\pi}{m_s}\right)^2 \frac{e^{-m_\pi r}}{r}\left[\sigma_1 \cdot \sigma_2 + S_{12}\left(1 + \frac{3}{m_\pi r} + \frac{3}{(m_\pi r)^2}\right)\right] \tag{1.5}$$

where f_π is the πNN coupling constant and m_s is a scaling mass, for which the charged pion mass is typically used. Charge dependence enters in the coupling constant and mass of the pions, with the OPE potential for pp scattering given by

$$V^{pp}_{OPE} = V_{OPE}(f_{\pi^0}, m_{\pi^0}) \tag{1.6}$$

and for np scattering

$$V^{np}_{OPE}(T) = -V_{OPE}(f_{\pi^0}, m_{\pi^0}) + 2(-1)^{T+1} V_{OPE}(f_{\pi^\pm}, m_{\pi^\pm}). \tag{1.7}$$

The isospin T=1 np partial-wave contributions are calculated similarly to the pp case, with the pp OPE component of the nuclear potential (Eqn. 1.6) replaced by the np OPE (Eqn. 1.7). The long-range potentials for the two cases look like

$$\begin{aligned} pp &: V = V_N + V_C \\ np &: V = [V_N - V_{OPE}(pp)] + V_{OPE}(np), \end{aligned} \tag{1.8}$$

where V_C is the Coloumb part of the potential. As in other analyses, the $^1S_0$ phase shift is parameterized independently, due to clear charge-independence breaking in the $^1S_0$ partial wave.

These potentials are then applied to a Schrödinger equation and the resulting phase shifts used to calculate the observables. The χ^2 between the calculated observables and the experimental data is used to adjust the parameters of the partial-wave potentials. As a result of this, the πNN coupling constant is a free parameter of the analysis and is determined by the data.

The quality of a phase-shift analysis is usually stated in terms of χ^2/N_{df}. N_{df} is the number of degrees of freedom in the analysis, which is the difference between the number of data points fitted, $N_{observables}$, minus the number of model parameters, $N_{parameters}$, used to fit the data and is given by

$$N_{df} = N_{observables} - N_{parameters}. \tag{1.9}$$

The analysis then "predicts" the experimental data points and tries to minimize the difference between these predictions and the measured data. The χ^2 is defined as

$$\chi^2 = \sum_{i=1}^{N_{obs}} \left[\frac{x_i^{model} - x_i^{exp}}{\Delta x_i^{exp}} \right]^2, \tag{1.10}$$

where x_i^{model} are the model predictions, x_i^{exp} are the data points and Δx_i^{exp} are the experimental uncertainties in the data. If the model predictions are correct and the data constitutes a statistical ensemble, the minimum possible value for the χ^2 is given by

$$\langle \chi^2_{min} \rangle / N_{df} = 1 \pm \sqrt{2/N_{df}}. \tag{1.11}$$

One additional feature of the Nijmegen analysis is that the database is "pruned" of experimental data that deviate from the predictions of the bulk of the data. Initially all data are included and the parameters are adjusted to obtain a χ^2_{min}. Data which are more than 3 standard deviations off are rejected, and the parameters are adjusted again [Ber90]. Also data with experimental normalizations that contribute more than 9 to the χ^2 are "floated" by the Nijmegen group, with this normalization entering as another parameter. For the *pp* data set, 291 data were rejected from the initial set of 1917 scattering observables. For the *np* data set, of the initial 3298 observables, 932 were rejected.

The final results of the Nijmegen analyses are impressive, with all three analyses (*pp*, *np*, and *pp* + *np*) having $\chi^2/N_{df} \sim 1$. For the energy-dependent *pp* partial-wave analysis with 1787 scattering observables and 1613 degrees of freedom (with an expected minimum of $\chi^2_{min}/N_{df} = 1.000 \pm 0.035$) the result was $\chi^2/N_{df} = 1.108$. For the *np* analysis, with 2514 scattering data and 2332 degrees of freedom (with an expected minimum of $\chi^2_{min}/N_{df} = 1.000 \pm 0.029$) the result was $\chi^2/N_{df} = 1.067$ [Sto93]. For the combined analysis, where both *pp* and *np* data were fit simultaneously, the result was $\chi^2/N_{df} = 1.081$. The Nijmegen group, however, believes the *pp* phase shifts from this combined analysis are not as good as those from the *pp* analysis due to a greater model dependence of the combined analysis.

The Nijmegen analysis was unique in that the *np* phase shifts were determined independently of the *pp* phase shifts. In most *np* phase shift analyses, only some of the partial-wave phase shifts are parameterized, particularly the $^1S_0$ and the *np* isoscalar partial waves, which are not present in *pp* scattering. The remaining isovector partial waves are taken from the *pp* data and usually corrected for charge-independence breaking (CIB) effects.

1.3.2 VPI Phase-Shift Analysis

The Virginia Polytechnical Institute and State University (VPI) phase-shift analysis extends to 1.6 GeV for the pp analysis and up to 1.3 GeV for the np data [Arn94]. In their analysis all partial waves above L = 6 come from one-pion exchange (OPE) in Born approximation and are not free parameters in the analysis. Partial waves of angular momentum L $\leq$ 5 are determined by the data, with corrections made for energy dependence and charge dependence. Below the pion-production threshold, the phase shifts are parameterized in terms of energy-dependent K matrices. The relation is given by

$$K_L(T_{lab}) = B_L^{OPE}(T_{lab}) + \sum_{i=1}^{N} \alpha_{L_i} F_{L_i}(T_{lab}), \tag{1.12}$$

where B_L^{OPE} is the partial-wave projected OPE amplitude in Born approximation and the F_{L_i} contain terms proportional to multiples of the pion mass. Both are functions of Legendre polynomials of the second kind, which can be thought of as partial-wave projections of central forces of Yukawa shape represented in momentum space. The α_{L_i} in Eqn. 1.12 are partial-wave dependent "coupling constants" for the Yukawa terms which allow for the simulation of spin-orbit and tensor forces from the central force Yukawa terms. These "coupling constants" are adjusted during the analysis so as to produce phase shifts with the smallest χ^2. This parameterization is used for all partial waves except for $^1S_0$ and $^3S_1$-$^3D_1$. For the difference in the T=1 np and pp phase shifts, the pion mass difference is taken into account for OPE and the pp phase shifts are calculated in Coloumb distorted-wave Born approximation.

1.4 Theoretical Difficulty?

As mentioned in Sec. 1.3, this change in the accepted values of the pion coupling constants has profound implications for our understanding of the nuclear force. In particular all NN potentials before 1990 were based on the old larger values of the pion coupling constants. The predictions of these models would be quite different using the new smaller

	I	II	III	IV	V	Experiment
Modified coupling constants						
$g^2_{\pi^o}/4\pi$	14.4	13.5	13.5	14.0	13.5	
$g^2_{\pi^\pm}/4\pi$	14.4	13.5	13.5	14.0	14.4	
κ_ρ	6.1	6.1	3.7	6.1	6.1	
Deuteron parameters						
Q_d (fm^2)	0.278	0.266	0.274	0.273	0.275	0.276(3)
A_D/A_S	0.0264	0.0251	0.0257	0.0259	0.0261	0.0256(4) [Rod90] 0.0271(2) [Sto88] 0.0273(5) [Vua89]
P_D (%)	4.99	4.56	5.31	4.75	4.91	
$^3P_0$ pp phase shifts ($^\circ$)						
10 MeV	4.104	3.731	4.105	3.883	3.731	3.729(17) [Sto93]
25 MeV	9.254	8.612	9.968	8.952	8.612	8.575(53) [Sto93]
50 MeV	12.39	11.57	14.40	12.00	11.57	11.47(9) [Sto93]

Table 1.2: Modified Bonn B potential-model predictions.

values of these coupling constants. Also, while the predictions of these models for scattering observables cannot compare with the accuracy of the Nijmegen analysis, NN bound state properties, namely the deuteron properties, which were not considered in the Nijmegen analysis must also be described by these new coupling constant values.

The deuteron, with its large radius, is dominated by the one-pion exchange (OPE), and therefore should be very sensitive to changes (of about 6% in this case) in the pion coupling constants. In addition, the deuteron properties are well known experimentally, severely constraining the potential models. In particular, the quadrupole moment of the deuteron (Q_d) and the asymptotic D- to S-state ratio (A_D/A_S) result from the tensor component of the nuclear force which is due mainly to the pion. Both these properties are known experimentally to $\sim$2%. These properties have been well described by the NN potentials using the old larger values. Therefore, how well do the potentials perform if these new values are considered the correct ones?

To study the sensitivity of the coupling constants more clearly, Machleidt and Li prepared several models based on the Bonn B potential (a OPE version of the full Bonn

potential) in which the pion coupling constants were varied between the old and new values [Mac93]. With these models, predictions were made to see if the deuteron properties and the scattering phase shifts could still be predicted. The models and predictions are summarized in Table 1.2. Note that in all models the value of the deuteron binding energy, the triplet effective range parameters and the *overall* fit to the NN phase shifts were comparable. In this study Model I is essentially Bonn B, based on the large values for both coupling constants. Model II uses the new smaller values for both coupling constants as determined in the Nijmegen analysis. The three other models discussed here (one model shown in the original paper is not mentioned here) represent various compromises to the present situation.

For the deuteron, the calculated results are compared with the current experimentally determined values. Note that for the quadrupole moment, the experimental value listed in the table is corrected for meson-exchange currents and relativistic contributions from its experimentally determined value of $Q_d = 0.2859 \pm 0.0003$ fm^2. The corrected value is $Q_d = 0.276 \pm 0.003$ fm^2, where the uncertainty assumed for the theoretical corrections is zero. It can be seen that Model I predicts the quadrupole moment quite well, giving $Q_d = 0.278$ fm^2, while Model II underpredicts the value at $Q_d = 0.266$ fm^2. However, looking at NN scattering, the older, larger coupling constants overpredict the pp ^3P_J phase shifts, while the smaller values describe the experimental values quite well. According to Machleidt and Li this overprediction of the ^3P_J phase shifts is a common problem for all meson-exchange models at low energies. And since at low energies the nuclear interaction is dominated by OPE, the only way to solve this problem is a smaller πNN coupling constant. This solution fits the ^3P_J phase shifts more accurately and introduces little change in other partial waves.

A note about the asymptotic D- to S-state ratio, A_D/A_S: the three values given in Table 1.2 are the most recent experimental values. The large discrepancy between the values makes this observable useless as a probe into the sensitivity of the different models

to the pion-coupling constants. This is unfortunate since according to Ericson [Eri97] the asymptotic D- to S-state ratio would be the best two-nucleon observable for extracting the πNN coupling constant.

The discrepancy between the predictions of Models I and II is troubling since the same potential must be able to describe *both* the bound-state and the scattering properties of the nuclear interaction. Machleidt and Li propose some solutions to the problem, the results of which are shown in Table 1.2. Model III supposes a reduction in the ratio of the ρ tensor-to-vector coupling, κ_ρ, from 6.1 to 3.7 (the vector-meson dominance model) which sufficiently describes the deuteron quadrupole moment, but provides an even worse description of the pp ^3P_J phase shifts than Model I. Model IV suggests a "compromise" value for the pion-coupling constants, with the κ_ρ ratio again set at 6.1. With the values of $g^2_{\pi^\circ}/4\pi = g^2_{\pi^\pm}/4\pi = 14.0$, both the deuteron properties as well as the scattering phase shifts are reproduced fairly well. A third solution, Model V, supposes a large charge-independence breaking between the pion coupling constants with a smaller value for the neutral coupling, $g^2_{\pi^\circ}/4\pi = 13.5$, and a larger value for the charged coupling, $g^2_{\pi^\pm}/4\pi = 14.4$. Here, both the deuteron properties and the scattering phase shifts are also well reproduced.

Due to the high accuracy of the pp scattering data, it seems fairly certain that the new smaller value for the neutral pion coupling constant is correct. This raises the following question: can a measurement be made which will prove sensitive enough to pin down the value of the value of the charged pion coupling constant? The Nijmegen group insists that no single observable is responsible for the lower coupling constants; the new values are determined by the bulk of the data. However the importance of this question makes the search for such a measurement a worthwhile goal. One measurement considered has been the np cross section at backward angles. Ericson *et al.* [Eri97] recently performed such a measurement at 162 MeV at Uppsala. In their analysis a variant of the Chew method was used to extract the charged pion coupling constant from the data. The value they determined, $g^2_{\pi^\pm}/4\pi = 14.4 \pm 0.2$ ($f_{\pi^\pm} = 0.080 \pm 0.001$) is in agreement with the old

value. The Nijmegen group claims that this result is in disagreement with the majority of the np cross-section data, and that Chew-type extrapolations of all available np and $\bar{p}p \rightarrow \bar{n}n$ data by themselves, as well as reanalysis by the VPI group using the Chew method on all available np cross-section measurements have been consistent with the lower values of $g^2_{\pi^\pm}/4\pi \sim 13.5$ ($f_{\pi^\pm} \sim 0.075$).

So it remains: is there another observable that provides direct sensitivity to the charged pion coupling constant? Let us consider one observable, the low-energy np vector analyzing power, $A_y(\theta)$. At low enough energies, only S and P-waves can contribute to the np scattering. It is well known that the analyzing power is dominated by the ${}^3P_J$ waves. According to Tornow *et al.* [Tor80] the low-energy np $A_y(\theta)$ (below 20 MeV) can be approximated by

$$A_y(\theta) = \frac{\sin^2(\delta_{01})\sin\theta}{4k^2\sigma(\theta)}\left[-2\delta_{10} - 3\delta_{11} + 5\delta_{12} + (-9\delta_{21} - 5\delta_{22} + 14\delta_{23})\cos\theta\right], \qquad (1.13)$$

where δ_{LJ} are the partial-wave phase shifts, $\sigma(\theta)$ is the differential cross section in the center-of-mass system and k is the wave number. This equation assumes the orbital angular momentum, $L \leq 2$, with small phase shifts for $L \geq 1$ and that the ${}^3S_1$-${}^3D_1$ mixing paramter, $\varepsilon_1 = 0$. The differential cross section is dominated by S-wave phase shifts at low energies with negligible contributions from higher waves. However, the analyzing power is the result of the spin-orbit interaction, S-wave scattering does not contribute to it, leaving only contributions from higher partial waves. That this contribution is small can be seen in the extremely small analyzing powers at low energies, with a maximum of ~1.5% at 12 MeV and ~0.7% at 7.6 MeV. Additionally, the D-wave contributions at low energies are very small, with the result that the np analyzing power is dominated by the ${}^3P_J$ waves. Since P-waves are peripheral waves they should mainly probe the long-range part of the nuclear interaction, the part of the interaction dominated by OPE. Therefore, the vector analyzing power, $A_y(\theta)$, should be sensitive to the pion coupling constant.

To study the sensitivity of the coupling constants in the case of the np analyzing power, Machleidt prepared three models based on the recent charge-dependent Bonn OPE

potential (CD-Bonn) [Mac96b], which uses, reflecting the now widely accepted point of view, the new values for the neutral and charged pion coupling constants. The models prepared for the sensitivity study used the new value for the neutral pion coupling constant, but for the charged coupling constant, the value was varied between the old larger value and the new smaller value. The models are labeled A, B and C (not to be confused with the OPE parameterizations of the full Bonn potential mentioned earlier) and use for $g^2_{\pi^\pm}/4\pi$ values of 13.6, 14.0 and 14.4, respectively. Model A corresponds to the predictions of the Nijmegen phase-shift analysis and is essentially CD-Bonn. Model C represents a large charge-independence breaking in the pion coupling constant. Model B represents a "compromise", with a value for $g^2_{\pi^\pm}/4\pi$ between the two extremes.

To calculate the observables, the phase shifts predicted by these models were used as input to Arndt's Scattering Analysis Interactive Dial-in code (SAID) [Arn92]. The predictions for the np $A_y(\theta)$ of these models at two different incident neutron energies, 7.6 and 12 MeV, are shown in Figs. 1.3 and 1.4. Here the dotted curve is the prediction of Model A, the solid curve that of Model B and the dash-dotted curve the prediction of Model C. It can be seen that as the coupling constant is increased, the value of the analyzing power decreases. The sensitivity is greatest at the peak near θ_{cm}= 65° with a ∼10% difference between the three models at 7.6 MeV and an ∼8% difference at 12 MeV. The values of $A_y(\theta)$ at $\theta_{cm} = 65°$ for 7.6 MeV are 0.00772 for Model A, 0.00702 for Model B and 0.00626 for Model C. At 12 MeV the peak values are 0.01809 for Model A, 0.01687 for Model B and 0.01554 for Model C. It can be seen that the relative sensitivity is greatest at the lower energy though the larger $A_y(\theta)$ at the higher energy is easier to measure experimentally. This sensitivity to changes in the pion coupling constant decreases rapidly with increasing incident neutron energy as can be seen in Fig. 1.7, where phase shifts at $E_n = 30$ MeV from Models A, B and C were used to calculate $A_y(\theta)$. All three curves lie on top of each other and are experimentally and visually indistinguishable. This sensitivity to the charged pion coupling constant at low energies is only seen in the analyzing power. Figs. 1.5 and

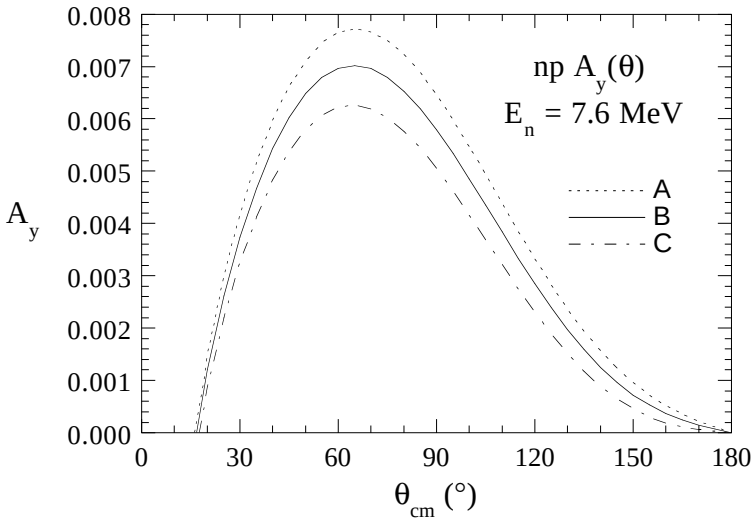

Figure 1.3: *np* $A_y(\theta)$ at $E_n = 7.6$ MeV as predicted by charge-dependent Bonn potential models. The neutral pion coupling constant is fixed at 13.6. For the charged coupling constant, A) 13.6, B) 14.0 and C) 14.4.

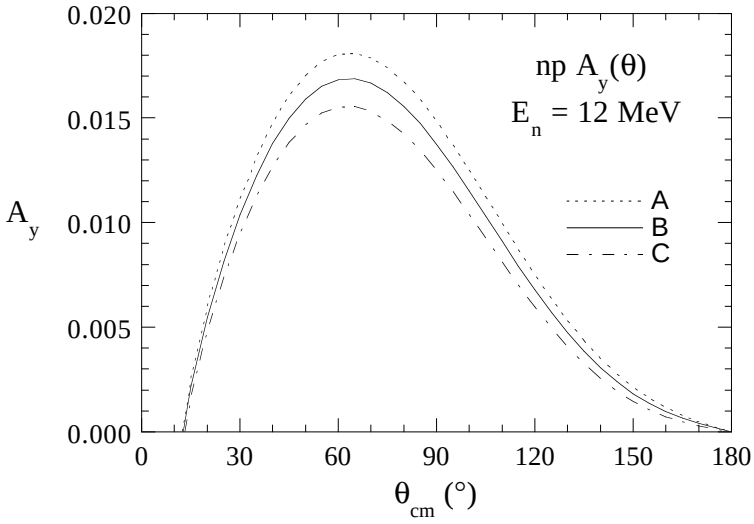

Figure 1.4: *np* $A_y(\theta)$ at $E_n = 12$ MeV as predicted by charge-dependent Bonn potential models. The neutral pion coupling constant is fixed at 13.6. For the charged coupling constant, A) 13.6, B) 14.0 and C) 14.4.

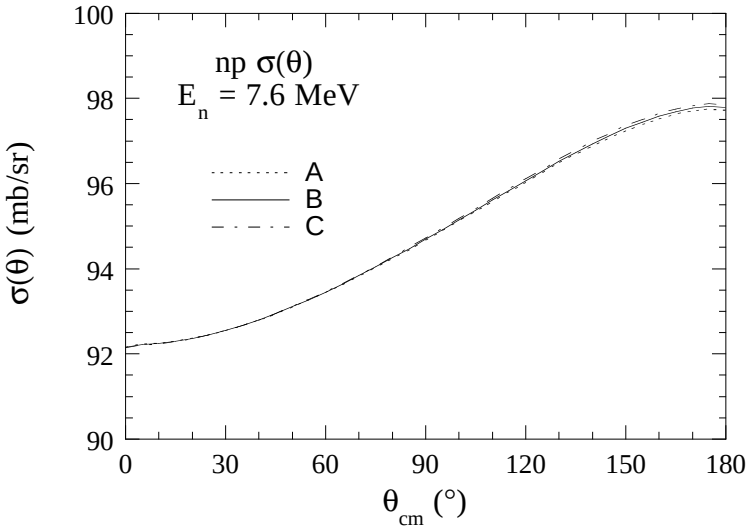

Figure 1.5: *np* differential cross sections at E_n= 7.6 MeV as predicted by charge-dependent Bonn potential models. The neutral pion coupling constant is fixed at 13.6. For the charged coupling constant, A) 13.6, B) 14.0 and C) 14.4. Note the cross-section scale.

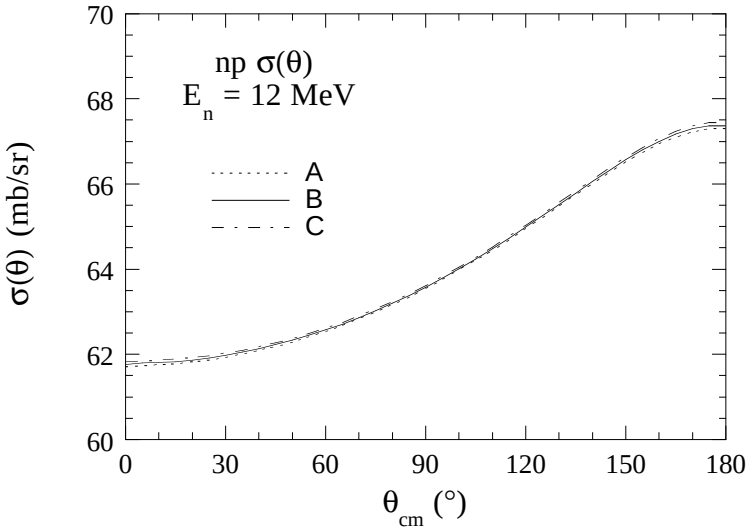

Figure 1.6: *np* differential cross sections at E_n= 12 MeV as predicted by charge-dependent Bonn potential models. The neutral pion coupling constant is fixed at 13.6. For the charged coupling constant, A) 13.6, B) 14.0 and C) 14.4. Note the cross-section scale.

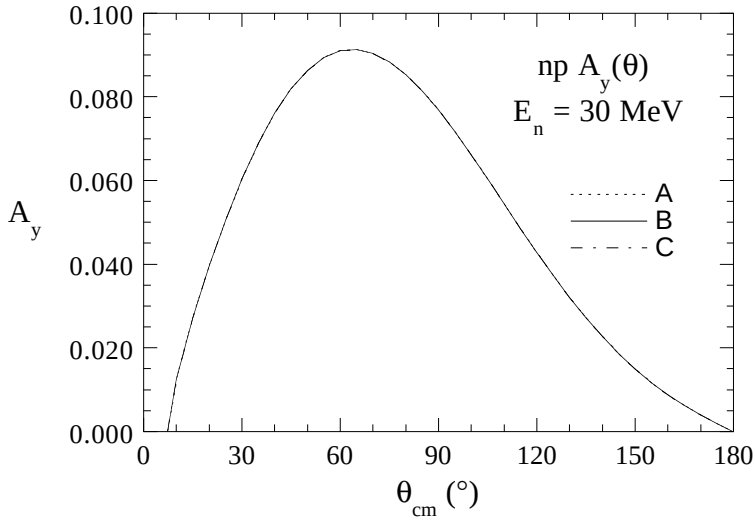

Figure 1.7: np $A_y(\theta)$ at $E_n = 30$ MeV as predicted by charge-dependent Bonn potential models. The neutral pion coupling constant is fixed at 13.6. For the charged coupling constant, A) 13.6, B) 14.0 and C) 14.4.

1.6 show differential cross-section predictions of the models at $E_n = 7.6$ and 12 MeV; the difference between the three models is too small to be seen experimentally.

In summary, a sufficiently accurate measurement of the np analyzing power should be able to differentiate between the model predictions discussed above, and since the only variable in these calculations is the charged pion coupling constant, one should be able to fix its value.

1.5 Scattering theory

When considering the scattering of a particle by a potential, we assume that the potential is bound within a certain range, outside of which it vanishes. Then the particle, moving freely with some momentum, can initially be described by the time-dependent Schrödinger equation [Glo83]

$$H_0|\psi_0(t)\rangle = i\frac{\partial}{\partial t}|\psi_0(t)\rangle, \tag{1.14}$$

where the free Hamiltonian operator is

$$H_0 = -\frac{1}{2m}\nabla^2. \tag{1.15}$$

When the particle enters the range of a potential it will feel a force which in the classical sense changes the particle's trajectory. Here the motion of the particle is described by the time-dependent Schrödinger equation

$$H|\Psi(t)\rangle = i\frac{\partial}{\partial t}|\Psi(t)\rangle, \tag{1.16}$$

with the full Hamiltonian operator, $H = H_0 + V$. The question is then how are the wave functions of the free particle and the particle influenced by the potential related? It turns out that one must express the relation in terms of the wave function norms, which unlike the wave function amplitudes, are time independent. This leads to the following relation:

$$\lim_{t\to-\infty} \|\Psi(t) - \psi_0(t)\| \to 0, \tag{1.17}$$

which must be true as the particle reaches the range of the potential. From the time-dependent Schrödinger equations for each region

$$\begin{aligned} |\psi_0(t)\rangle &= e^{-iH_0(t-t_0)}|\psi_0(t_0)\rangle \\ |\Psi(t)\rangle &= e^{-iH(t-t_0)}|\Psi(t_0)\rangle \end{aligned} \tag{1.18}$$

and the requirement of Eqn. 1.17 the following condition must link the two wave equations:

$$|\Psi(t_0)\rangle = \lim_{\tau\to-\infty} e^{iH\tau}e^{-iH_0\tau}|\psi_0(t_0)\rangle. \tag{1.19}$$

From this condition a specific scattering state at an arbitrary time can be constructed which corresponds to the initial conditions occurring in the infinite past. The limit given in Eqn. 1.19 is defined as the Möller operator:

$$\Omega^{(+)} = \lim_{\tau\to-\infty}(e^{iH\tau}\cdot e^{-iH_o\tau}), \tag{1.20}$$

where the "(+)" superscript denotes that the scattering state develops out of the initial state in the infinite past. Then for an arbitrary time, t, Eqn. 1.19 can be rewritten as

$$|\Psi(t)\rangle = \Omega^{(+)}|\psi_0(t)\rangle, \tag{1.21}$$

which is the solution to the scattering problem for a specific choice of initial conditions. This form, however, is not a practical solution; the standard method for proceeding involves reformulating Eqn. 1.19 as follows:

$$|\Psi(0)\rangle = \lim_{\varepsilon\to 0}\int dq \frac{i\varepsilon}{E_q + i\varepsilon + H}|\psi_q^0\rangle f_0(q). \tag{1.22}$$

This equation suggests one of the central operators in scattering theory, the resolvent operator, $G(z)$, to the Hamiltonian. This operator acts as a propagator for the motion of the particle, either in free space or in the field of a potential. For the case of a particle in a potential it is defined as

$$G(z) = \frac{1}{z - H}, \tag{1.23}$$

where in comparison with Eqn. 1.22 it can be seen that $z = E_q + i\varepsilon$. For the case of the free particle the resolvent operator is simply

$$G_0(z) = \frac{1}{z - H_0}. \tag{1.24}$$

If G is then applied to a momentum eigenstate, $|\psi_q^0\rangle$, we get

$$|\Psi_q^+\rangle = \lim_{\varepsilon\to 0}\frac{i\varepsilon}{E_q + i\varepsilon + H_0}V|\psi_q^0\rangle, \tag{1.25}$$

which is a solution to the stationary Schrödinger equation, and contains all the information about the scattering process. By integrating over the momenta, the time-dependent state for a general momentum distribution is:

$$|\Psi(t)\rangle = e^{-iH_0t}|\Psi(0)\rangle = +\int dq|\Psi_q^+\rangle e^{-iE_qt}\ f_0(q). \tag{1.26}$$

This result allows us to determine the transition rate into a state of a given momentum, q_f, at a given time, t, as

$$A_{q_f}(t) \equiv \langle\psi_{q_f}^0(t)|\Psi(t)\rangle. \tag{1.27}$$

To determine what the momentum components of the stationary scattering state are, the following identity between the free and full Hamiltonian resolvent operators,

$$G(z) = G_0(z) + G_0(z)VG(z), \tag{1.28}$$

can be applied to Eqn. 1.25, separating $|\Psi_q^{(+)}\rangle$ into a free and a scattered part:

$$|\Psi_q^+\rangle = |\psi_q^0\rangle + \lim_{\varepsilon\to 0} \frac{1}{E_q + i\varepsilon + H_0} V|\Psi_q^+\rangle. \tag{1.29}$$

This equation is known as the Lippmann-Schwinger equation. With this equation, the momentum components of $|\Psi_q^{(+)}\rangle$ can be expressed as

$$\langle\psi_{q_f}^0|\Psi_q^+\rangle = \delta^3(q_f - q) + \lim_{\varepsilon\to 0} \frac{\langle\psi_{q_f}^0|V|\Psi_q^+\rangle}{E_q + i\varepsilon + E_{q_f}}. \tag{1.30}$$

Eqn. 1.30 defines the central matrix of scattering theory, the T-matrix, as

$$T_{q_f q} \equiv \langle\psi_{q_f}^0|V|\Psi_q^+\rangle. \tag{1.31}$$

Using the result of Eqn. 1.30 the transition rate from Eqn. 1.27 is determined to be

$$\begin{aligned} \lim_{t\to\infty} A_{q_f}(t) &= \int dq \left[\delta^3(q - q_f) - 2\pi i\ \delta(E_{q_f} - E_q)T_{q_f q}\right]\ f_0(q) \\ &\equiv \int dq\ S_{q_f q} f_0(q). \end{aligned} \tag{1.32}$$

Here $S_{q_f q}$ is the probability amplitude for scattering from an initial state of momentum, q, to a final state of momentum, q_f, and is called the *S-matrix element.*

1.5.1 Partial-Wave Expansion

The elastic scattering of nucleons can be understood as the superposition of an incoming plane wave and outgoing spherical waves. For the case of spinless particles and purely central forces, the incident plane wave can be written as:

$$\begin{aligned} \Psi_i &= Ae^{ikz} \\ &= A\sum_{\ell=0}^{\infty} i^\ell(2\ell+1)j_\ell(kr)P_\ell(\cos\theta), \end{aligned} \tag{1.33}$$

where $j_\ell(kr)$ are spherical Bessel functions and $P_\ell(\cos\theta)$ are Legendre polynomials. Such an expansion of the wave function is known as a *partial-wave expansion*. Here the ℓ refer to the different angular momentum components of the expansion. For large values of r (where $kr \gg \ell$), the spherical Bessel function can be approximated as:

$$\begin{aligned} j_\ell &\approx \frac{\sin(kr - \frac{1}{2}\ell\pi)}{kr} \\ &\approx i\frac{e^{-i(kr-\frac{1}{2}\ell\pi)} - e^{+i(kr-\frac{1}{2}\ell\pi)}}{2kr}, \end{aligned} \tag{1.34}$$

so that the incident plane wave can be described as:

$$\Psi_i = \frac{A}{2kr}\sum_{\ell=0}^{\infty} i^{\ell+1}(2\ell+1)\left[e^{-i(kr-\frac{1}{2}\ell\pi)} - e^{+i(kr-\frac{1}{2}\ell\pi)}\right]P_\ell(\cos\theta). \tag{1.35}$$

Here the first term inside the brackets describes a spherical wave converging on the target while the second term describes a spherical wave expanding outward from the target. Only the outgoing wave can be affected by the scattering; this can be accounted for by modifying the second term in Eqn. 1.35 by a factor, η_ℓ. The total plane wave can then be written as

$$\Psi = \frac{A}{2kr}\sum_{\ell=0}^{\infty} i^{\ell+1}(2\ell+1)\left[e^{-i(kr-\frac{1}{2}\ell\pi)} - \eta_\ell e^{+i(kr-\frac{1}{2}\ell\pi)}\right]P_\ell(\cos\theta). \tag{1.36}$$

The scattered wave can then be obtained by subtracting Eqn. 1.35 from Eqn. 1.36 giving the result

$$\begin{aligned} \Psi_s &= \Psi - \Psi_i \\ &= \frac{A}{2kr}\sum_{\ell=0}^{\infty} i^{\ell+1}(2\ell+1)(1-\eta_\ell)e^{i(kr-\frac{1}{2}\ell\pi)}P_\ell(\cos\theta) \\ &= \frac{A}{2k}\frac{e^{ikr}}{r}\sum_{\ell=0}^{\infty} i(2\ell+1)(1-\eta_\ell)P_\ell(\cos\theta). \end{aligned} \tag{1.37}$$

For elastic scattering, the amplitude of the scattered wave must remain unchanged, only the phase can be modified. In this case the coefficient, η_ℓ, can be set equal to $e^{2\delta_\ell}$ where δ_ℓ are the phase shifts.

In the asymptotic limit, the total wave function can then be written in terms of the scattering amplitude, $f(\theta)$, as

$$\Psi = A\left[e^{ikz} + f(\theta)\frac{e^{ikr}}{r}\right]. \tag{1.38}$$

Comparing this to Eqn. 1.36, the scattering amplitude can be expressed as

$$f(\theta) = \frac{i}{2k}\sum_{\ell=0}^{\infty}(2\ell+1)(1-e^{i\delta_\ell})P_\ell(\cos\theta). \tag{1.39}$$

The differential cross section, which is defined in terms of the scattering amplitude, can be written in terms of the partial waves yielding the following:

$$\begin{aligned}\sigma(\theta) &= |f(\theta)|^2 \\ &= \frac{1}{k^2}\left|\sum_{\ell=0}^{\infty}(2\ell+1)e^{i\delta_\ell}\sin\delta_\ell P_\ell(\cos\theta)\right|^2.\end{aligned} \tag{1.40}$$

Integrating this over θ then gives the total cross section

$$\sigma = \frac{4\pi}{k^2}\sum_{\ell=0}^{\infty}(2\ell+1)\sin^2\delta_\ell, \tag{1.41}$$

which is made up of scattering eigenstates corresponding to the values of ℓ. The phase shifts, δ_ℓ then determine the contribution of each eigenstate to the cross section.

1.5.2 Spin

The discussion so far has considered spinless particles. The addition of spin, however, increases the complexity of the scattering state. Nucleons exist as a spin doublet, each nucleon having a total spin $\frac{1}{2}$ and a projection of $\pm\frac{1}{2}$. Thus for two nucleons, the spin space can be described by the orthonormal basis:

$$|\lambda_i\rangle = \{|m_1\rangle\ |m_2\rangle\} \tag{1.42}$$

where $i = 1, 2, 3, 4$ for each of the possible states. It is assumed that the momentum distributions we consider will consist of pure states for which there will be only one type of wave

packet. The spin states, in general, will occur as mixed states, with each pure spin state occurring with some probability, p_n, for a general state

$$|n\rangle = \sum_i \; a_i^{(n)} |\lambda_i\rangle, \tag{1.43}$$

where $a_i^{(n)}$ are the amplitudes for the spin states.

Using the above equations, we can now generalize the Lippmann-Schwinger equation (Eqn. 1.29) so that it will describe the scattering state in both spin and momentum space as it develops out of the initial pure spin and pure momentum states. This generalized equation takes the form

$$|qn\rangle^{(+)} = |q\rangle|n\rangle + \sum_i \; |\lambda_i\rangle\langle\lambda_i| G_0^{(+)} V |qn\rangle^{(+)}, \tag{1.44}$$

where the unit spin operator, $|\lambda_i\rangle\langle\lambda_i|$, is explicitly inserted in front of the resolvent operator and potential, $G_0 V$. The potential, V, is assumed to be spin-dependent, thus the scattering amplitude will depend on the initial spin state in a nontrivial way. By explicitly introducing the T-matrix operator into the equation for the scattering amplitude we get

$$\begin{aligned} f_i(q', q) &= -\mu(2\pi)^2 \langle\lambda_i|\langle q'|V|qn\rangle^{(+)} \\ &= -\mu(2\pi)^2 \sum_j \; \langle\lambda_i|\langle q'|T|q\rangle|\lambda_j\rangle a_j^{(n)} \\ &\equiv \sum_j \; M_{ji}(q', q) a_j^{(n)}, \end{aligned} \tag{1.45}$$

where the final form shows the dependence of the scattering amplitude on the initial spin-state coefficients, $a_j^{(n)}$. This final form also defines the *M-matrix*. The M-matrix contains all the dynamic information about the scattering process in both spin and momentum space.

1.5.3 Isospin

In addition to the spin states, in nuclear physics the concept of isospin adds a further classification of states to the scattering process. Isospin symmetry is only approximate,

being broken by the electromagnetic interaction, but in interactions where it is conserved, it allows the neutron and proton to be treated as identical particles existing in different isospin states. The nucleons exist as an isospin doublet, similar to the spin case, with total isospin, $t = \frac{1}{2}$ and spin projections of $m_t = -\frac{1}{2}$ for the neutron and $m_t = \frac{1}{2}$ for the proton. For two nucleons the physical state is generally a superposition of the states of total isospin, $T = 0$ and $T = 1$. Where isospin is conserved, the two states may be treated separately and the M-matrix elements will be built up of linear combinations of the $M^{T=0}$ and $M^{T=1}$ matrix elements. Because the states must be symmetric under the exchange of the two particles, only the $T = 1$ states will occur for the pp and nn systems. For the np system, the physical amplitude will be

$$M_{np} = \frac{1}{2}(M^{T=0} + M^{T=1}). \tag{1.46}$$

For the case where isospin is conserved, the scattering amplitude of Eqn. 1.45 becomes

$$f_i(q', q) = -\mu(2\pi)^2 \sum_j \langle \lambda_i | \langle t m_t | \langle q' | T\{|q\rangle | \lambda_j\rangle | t m_t\rangle \}_a \; a_j^{(n)} \tag{1.47}$$

with the M-matrix then given by

$$M^t_{m_1' m_2' m_1 m_2}(q'q) = -\mu(2\pi)^2 \langle q' | \langle m_1' m_2' | \langle t m_t | T\{|t m_t\rangle | m_1 m_2\rangle | q\rangle \}_a. \tag{1.48}$$

1.5.4 The Wolfenstein Parameterization

In order to calculate the various spin observables, it is necessary to parameterize the M-matrix in terms of the space and spin states. To accomplish this, the following unit vectors are defined in terms of the initial and final momenta

$$\hat{k} \equiv \frac{(\mathbf{q}' - \mathbf{q})}{|\mathbf{q}' - \mathbf{q}|}, \qquad \hat{p} \equiv \frac{(\mathbf{q}' + \mathbf{q})}{|\mathbf{q}' + \mathbf{q}|}, \qquad \hat{n} \equiv \frac{(\mathbf{q}' \times \mathbf{q})}{|\mathbf{q}' \times \mathbf{q}|}. \tag{1.49}$$

These vectors describe a right-handed, orthogonal coordinate system in which $\hat{k}$ and $\hat{p}$ lie in the scattering plane and $\hat{n}$ is the normal. Additionally in nonrelativistic kinematics, these vectors have particular relevance in the laboratory system. $\hat{p}$ is in the direction of

the scattered nucleon, $\hat{k}$ is in the direction of the recoil nucleon, and $\hat{n}$ is normal to the scattering plane. The M-matrix can then be parameterized by a linear combination of the 4-dimensional matrices, S^μ, used to describe the density matrix. After taking into account which combinations are forbidden by parity and time-reversal invariance, the M-matrix can be parameterized by the following terms:

$$\begin{aligned} M &= a + c(\sigma^{(1)} + \sigma^{(2)})\hat{n} + m(\sigma^{(1)}\hat{n})(\sigma^{(2)}\hat{n}) \\ &\quad + (g+h)(\sigma^{(1)}\hat{p})(\sigma^{(2)}\hat{p}) + (g-h)(\sigma^{(1)}\hat{k})(\sigma^{(2)}\hat{k}). \end{aligned} \tag{1.50}$$

This parameterization is called the Wolfenstein parameterization [Wol52]. From this the different spin observables can be expressed in terms of the coefficients of the parameterization.

In order to calculate the Wolfenstein parameters, we can take advantage of the rotational invariance of the potential, and classify the scattering states in terms of states of fixed angular momentum. Then the M-matrix can be decomposed into parts corresponding to these angular momentum states, which require only a few parameters to describe. An additional benefit of this approach is that at sufficiently low energies, only a few angular momentum states will be involved in the interaction, considerably reducing the calculation needed. The result of this decomposition is

$$\begin{aligned} M^s_{m'_s m_s} &= \frac{1}{iq} \sum_{J\ell\ell'} C(\ell' s J, m_s - m'_s m'_s m_s)\; Y_{\ell' M m_s}(\hat{q}') \\ &\quad \times\; i^{-\ell'+\ell}(S^J_{\ell',s,\ell,s} - \delta_{\ell'\ell})\; C(\ell s J, 0 m_s)\sqrt{\pi(2\ell+1)}\;[1-(-1)^{\ell+s+t}], \end{aligned} \tag{1.51}$$

which provides a link between the Wolfenstein parameters needed to calculate the observables, and the partial-wave S-matrix elements arising from the potential.

1.5.5 The S-Matrix

The S-matrix (defined in Eqn. 1.32) contains all the dynamical information about the scattering process. This matrix is both symmetric, due to the time-reversal invariance

of the potential, and unitary. The number of parameters necessary to describe the S-matrix then depends on the total spin of the scattering process. For the case in which $J = 0$, the S-matrix elements can be parameterized in terms of a single phase-shift parameter, $\delta_{\ell,J}$, since parity conservation forbids transitions between states of different angular momentum, ℓ. The S-matrix then takes the form

$$S^J_{\ell',s,\ell,s} = \begin{cases} e^{2i\delta_{\ell,J}} & \ell' = \ell \\ 0 & \ell' \neq \ell \end{cases} . \tag{1.52}$$

The phase shifts here follow the standard spectroscopic notation

$$\delta_{\ell,J} \rightarrow {}^{2s+1}L_J, \tag{1.53}$$

where for nucleon scattering, charge independence forbids the mixing of singlet and triplet spin states.

For the case where $J > 0$, there exist four possible states for each value of the total spin, J: a spin-singlet state with $\ell = J$ and three spin-triplet states with $\ell = J - 1$, $\ell = J$, and $\ell = J + 1$. The S-matrix will then have the following form:

$$S^{J\neq 0}_{\ell',s,\ell,s} = \begin{pmatrix} S^J_{J-1,1,J-1,1} & S^J_{J-1,1,J+1,1} & 0 & 0 \\ S^J_{J+1,1,J-1,1} & S^J_{J+1,1,J+1,1} & 0 & 0 \\ 0 & 0 & S^J_{J,0,J,0} & 0 \\ 0 & 0 & 0 & S^J_{J,1,J,1} \end{pmatrix} . \tag{1.54}$$

The uncoupled elements in the lower sub-matrix can be parameterized by a single phase-shift as in the $J = 0$ case. The coupled sub-matrix introduces a further parameterization, a coupling between the two angular momentum states. This coupled sub-matrix can be written in the following form:

$$S = e^{i\delta} \cdot e^{2i\varepsilon} \cdot e^{i\delta} \tag{1.55}$$

where δ is a diagonal matrix and ε is a symmetric matrix with zeroes on the diagonal

elements. These matrices are then given as

$$\delta = \begin{pmatrix} e^{\bar{\delta}_{J-1,J}} & 0 \\ 0 & e^{\bar{\delta}_{J+1,J}} \end{pmatrix} \tag{1.56}$$

and

$$\varepsilon = \begin{pmatrix} \cos 2\bar{\varepsilon}_J & i \sin 2\bar{\varepsilon}_J \\ i \sin 2\bar{\varepsilon}_J & \cos 2\bar{\varepsilon}_J \end{pmatrix}, \tag{1.57}$$

where the $\bar{\delta}_{\ell,J}$ (where $\ell = J \pm 1$) are the partial-wave phase shifts and $\bar{\varepsilon}_J$ is a mixing parameter between states. Substituting Eqns. 1.56 and 1.57 into Eqn. 1.55 yields the following result:

$$S = \begin{pmatrix} \cos 2\bar{\varepsilon}_J \; e^{2i\bar{\delta}_{J-1,J}} & i \sin 2\bar{\varepsilon}_J \; e^{i(\bar{\delta}_{J-1,J}+\bar{\delta}_{J+1,J})} \\ i \sin 2\bar{\varepsilon}_J \; e^{i(\bar{\delta}_{J-1,J}+\bar{\delta}_{J+1,J})} & \cos 2\bar{\varepsilon}_J \; e^{2i\bar{\delta}_{J+1,J}} \end{pmatrix}. \tag{1.58}$$

This is known as the "Stapp" or "bar" phase-shift parameterization [Sta57]. An alternate parameterization by Blatt and Biedenharn [Bla52b], [Bla52a] diagonalizes S using a unitary transformation

$$S = U^{-1} \begin{pmatrix} e^{2i\delta_{J-1,J}} & 0 \\ 0 & e^{2i\delta_{J+1,J}} \end{pmatrix} U \tag{1.59}$$

where

$$U = \begin{pmatrix} \cos \varepsilon_J & \sin \varepsilon_J \\ -\sin \varepsilon_J & \cos \varepsilon_J \end{pmatrix}. \tag{1.60}$$

This leads to the form

$$S = \begin{pmatrix} \cos^2 \varepsilon_J \; e^{2i\delta_{J-1,J}} + \sin^2 \varepsilon_J \; e^{2i\delta_{J+1,J}} & \frac{1}{2} \sin 2\varepsilon_J \; (e^{2i\delta_{J-1,J}} - e^{2i\delta_{J+1,J}}) \\ \frac{1}{2} \sin 2\varepsilon_J \; (e^{2i\delta_{J-1,J}} - e^{2i\delta_{J+1,J}}) & \cos^2 \varepsilon_J \; e^{2i\delta_{J+1,J}} + \cos^2 \varepsilon_J \; e^{2i\delta_{J-1,J}} \end{pmatrix}. \tag{1.61}$$

The relations between the Stapp and Blatt-Biedenharn parameters are given by the following

equations:

$$\begin{aligned} \bar{\delta}_{J-1,J} + \bar{\delta}_{J+1,J} &= \delta_{J-1,J} + \delta_{J+1,J} \\ \sin(\bar{\delta}_{J-1,J} - \bar{\delta}_{J+1,J}) &= \frac{\tan 2\bar{\varepsilon}_J}{\tan 2\varepsilon_J} \\ \sin(\delta_{J-1,J} - \delta_{J+1,J}) &= \frac{\sin 2\bar{\varepsilon}_J}{\sin 2\varepsilon_J} \end{aligned} \quad . \tag{1.62}$$

1.6 Calculating Spin Observables

Thus we have the following procedure for calculating the scattering observables from a given nuclear potential:

$$NN \text{ potential} \rightarrow S^J_{\ell',s,\ell,s} \rightarrow M^s_{m'_s m_s} \rightarrow \text{Wolfenstein parameters} \rightarrow \text{Observables}$$

We will look at the definition of the spin observables and how they are calculated from the Wolfenstein parameters. An in-depth discussion of the formalism of the spin observables can be found in Refs. [Glo83] and [Hos68].

1.6.1 The Density Matrix

In a polarization experiment, typically the initial state of the polarization is specified and it is finding the expectation values of the final polarization state that are of interest. A convenient formulation to this problem lies in expressing the scattering states in terms of density matrices. We can define the density operator as the matrix determined by the probabilities of the pure spin state as

$$\rho \equiv \sum_n |n\rangle p_n \langle n|. \tag{1.63}$$

where p_n are the relative probabilities of finding the system in the states defined in Eqn. 1.43. The density operator is a 4-dimensional, hermitian matrix and can be related to the expectation values of 16 linearly-independent, hermitian matrices, S^μ, where $\mu = 1, \ldots, 16$. A convenient set of such matrices may be constructed from the complete basis of 2×2 matrices, $\{\mathbf{1}, \sigma_x, \sigma_y, \sigma_z\}$, where the σ's are the Pauli spin matrices The following notation

is commonly used: $\sigma_0 \equiv \mathbf{1}$, $\sigma_1 \equiv \sigma_x$, $\sigma_2 \equiv \sigma_y$, and $\sigma_3 \equiv \sigma_z$. This set of spin operators, S^μ, is then given by

$$S^\mu \equiv \sigma_\alpha^{(1)} \sigma_\beta^{(2)} \quad (\alpha, \beta = 0, 1, 2, 3). \tag{1.64}$$

Given the density matrix, the expectation value for any spin operator, $\langle S^\mu \rangle$, is given by

$$\langle S^\mu \rangle = \frac{\sum_n p_n \langle n|S^\mu|n\rangle}{\sum_n p_n \langle n|n\rangle} = \frac{\mathrm{Tr}|\rho S^\mu|}{\mathrm{Tr}|\rho|}. \tag{1.65}$$

Thus the value of any final-state spin expectation values can be written as

$$\langle S^\mu \rangle_f = \frac{\mathrm{Tr}|\rho_f S^\mu|}{\mathrm{Tr}|\rho_f|}, \tag{1.66}$$

where ρ_f is the density matrix for the final state. The final-state density matrix is defined in terms of the scattered spin states; what is needed is the final-state expectation value in terms of the initial spin states, which are known. This can be done by applying the M-matrix defined in Eqn. 1.45 to the initial state density matrix, ρ_i. The final-state density matrix can then be written as

$$\rho_f = \sum_n M|n\rangle p_n \langle n|M^\dagger = M \rho_i M^\dagger. \tag{1.67}$$

Substituting this result into Eqn. 1.66, we can express the final-state expectation values of a given spin operator in terms of the initial-state density matrix

$$\langle S^\mu \rangle_f = \frac{\mathrm{Tr}|M \rho_i M^\dagger S^\mu|}{\mathrm{Tr}|M \rho_i M^\dagger|}. \tag{1.68}$$

The initial spin state is specified by the expectation value, $\langle S^\mu \rangle$, of S^μ given by Eqn. 1.64. The initial state density matrix is then

$$\rho_i = \frac{1}{4} \sum_{\mu=1}^{16} S^\mu \ \mathrm{Tr}|\rho_i S^\mu| = \frac{1}{4} \mathrm{Tr}|\rho_i| \sum_{\mu=1}^{16} S^\mu \langle S^\mu \rangle \tag{1.69}$$

using the relation of Eqn. 1.65. Then the final spin state expectation value can be written

$$\langle S^\mu \rangle_f = \frac{1}{4} \mathrm{Tr}|\rho_i| \ \frac{\sum_{\nu=1}^{16} \mathrm{Tr}|M S^\nu M^\dagger S^\mu|}{\mathrm{Tr}|M \rho_i M^\dagger|}. \tag{1.70}$$

As an example we can consider the simplest observable in the final state, the differential cross section, which does not measure spin orientations since it sums over all spin states. The differential cross section can be represented in terms of the density matrices by

$$I = \frac{\mathrm{Tr}|M\rho_i M^\dagger|}{\mathrm{Tr}|\rho_i|} = \frac{\mathrm{Tr}|\rho_f|}{\mathrm{Tr}|\rho_i|}. \tag{1.71}$$

This links arbitrary spin orientations in the initial state of both particles to all possible spin expectation values in the final state. With this result, the general expression for the spin observable in Eqn. 1.70 can be written as

$$I\langle S^\mu\rangle_f = \frac{1}{4}\sum_{\nu=1}^{16}\langle S^\mu\rangle_i \ \mathrm{Tr}|MS^\nu M^\dagger S^\mu|. \tag{1.72}$$

1.7 Analyzing Power

We will consider reactions of the form b($\vec{\mathrm{a}}$,a)b, where $\vec{\mathrm{a}}$ represents a polarized incident beam on an unpolarized target, b. The effect of the nuclear spin on the cross section in this reaction is observed in the analyzing power for the reaction. To develop the formulation we will first consider the case of b(a,a)b, where an unpolarized beam scattering from an unpolarized target. In this case the expectation values of all initial-state spin operators, $\langle S^\mu\rangle_i$, will be zero in Eqn. 1.68, except for the case of $\langle\sigma_0^{(a)}\sigma_0^{(b)}\rangle_i = 1$. Thus the unpolarized differential cross section is

$$I_0 = \frac{1}{4}\mathrm{Tr}\{MM^\dagger\}. \tag{1.73}$$

The unpolarized cross section sums over all spin states and thus in terms of the Wolfenstein parameterization (Eqn. 1.50) it is just the trace of all the terms [Hos68]

$$I_0 = |a|^2 + |m|^2 + 2|c|^2 + 2|g|^2 + 2|h|^2. \tag{1.74}$$

This scattering, however, produces a polarization vector in the outgoing beam, $\langle\sigma^{(a)}\rangle_f$. The expectation value of this polarization from Eqn. 1.68 is

$$I_0\langle\sigma^{(a)}\rangle_f = \frac{1}{4}\mathrm{Tr}\{MM^\dagger\sigma^{(a)}\}. \tag{1.75}$$

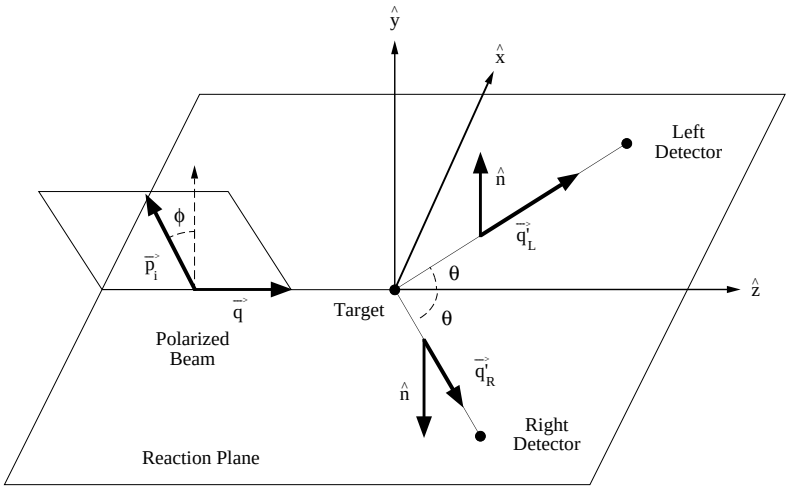

Figure 1.8: Coordinate system for analyzing power measurement (incident polarized beam) as recommended by the Madison convention The scattering normal $\hat{n}$ is defined by the vector cross product, $\mathbf{q} \times \mathbf{q}'$. It points in the positive $\hat{y}$-direction for scattering to the left side and in the negative $\hat{y}$-direction for scattering to the right side. The angle ϕ represents the angle between the incident polarization vector, $\vec{p}_i$, and the scattering normal, $\hat{n}$.

This axial polarization vector, $\langle \sigma^{(a)} \rangle_f$, is along the scattering plane normal. After taking the trace in Eqn. 1.75, we are left with functions of the initial and final momenta, $\mathbf{q}$ and $\mathbf{q}'$. The only axial vector that can be formed from these is $\mathbf{q} \times \mathbf{q}'$, which is along the $\hat{n}$-direction given in Eqn. 1.49. The polarization vector is thus given by

$$\langle \sigma^{(a)} \rangle_f = P\hat{n}, \tag{1.76}$$

where $P(\theta)$ is defined as the polarization. Eqn. 1.75 then becomes

$$I_0 P = \frac{1}{4}\mathrm{Tr}\{MM^\dagger(\sigma^{(a)}\hat{n})\}, \tag{1.77}$$

where $(\sigma^{(a)}\hat{n})$ is the normal component of the spin matrix for the incident beam particle, $\sigma^{(a)}$.

In the case where the incident beam is polarized, the initial density matrix now is characterized by the nonzero expectation value $p_i = \langle \sigma^{(a)} \rangle_i$. In this case the differential

cross section becomes

$$I = \frac{1}{4}\mathrm{Tr}\{MM^\dagger\} + \frac{1}{4}\langle\sigma^{(a)}\rangle_i \cdot \mathrm{Tr}\{M\sigma^{(a)}M^\dagger\}. \tag{1.78}$$

Here the first term on the right-hand side is just the unpolarized differential cross section, I_0. The second term represents the contribution of the initial-state beam polarization, $\langle\sigma^{(1)}\rangle_i$ to the cross section. The following trace relation exists in the case of time-reversal invariance

$$\mathrm{Tr}\{M\sigma^{(a)}M^\dagger\} = \mathrm{Tr}\{MM^\dagger\sigma^{(a)}\} \tag{1.79}$$

which lets us rewrite Eqn. 1.78

$$I = I_0(1 + p_i\, A_y \cos\phi), \tag{1.80}$$

where $p_i = |\langle\sigma^{(a)}\rangle_i|$ is the polarization of the incident beam and A_y is the analyzing power, a contribution to the unpolarized cross section due to the polarization component. (in analogy to Eqn. 1.77). Here ϕ is the angle between the incident polarization vector, $\langle\sigma^{(a)}\rangle_i$, and the scattering normal, $\hat{n}$.

In the ideal case where the incident polarization vector, $\langle\sigma^{(a)}\rangle_i$, is in the $\hat{y}$ direction, as defined in Fig. 1.8, and the scattering plane is set in the xz-plane, the angle $\phi = 0$ for scattering to the left side and $\phi = \pi$ for scattering to the right. The differential cross section for particles then is given as

$$\begin{aligned} I_L &= I_0(\theta)[1 + p_i\, A_y(\theta)] \\ I_R &= I_0(\theta)[1 - p_i\, A_y(\theta)]. \end{aligned} \tag{1.81}$$

One can then solve these two equations to determine the analyzing power

$$A_y = \frac{1}{p_i}\left[\frac{I_L - I_R}{I_L + I_R}\right]. \tag{1.82}$$

For the case of elastic scattering, the polarization of the beam due to scattering is equal the analyzing power from a polarized beam.

In terms of the Wolfenstein parameters, the analyzing power can be written (using Eqn. 1.77) as

$$I_0 A_y = \frac{1}{4}\mathrm{Tr}\{MM^\dagger(\sigma^{(a)}\hat{n})\}. \tag{1.83}$$

This can be evaluated by using the following trace relation:

$$\frac{1}{4}\mathrm{Tr}\{M\sigma_j M^\dagger\} = 2\hat{n}\mathrm{Re}\{c^*(a+m)\}. \tag{1.84}$$

The analyzing power is then given by

$$A_y = \frac{2\hat{n}\mathrm{Re}\{c^*(a+m)\}}{I_0}. \tag{1.85}$$

1.7.1 Experimental Definition of $A_y(\theta)$

The differential cross section is proportional to the number of counts recorded by the detectors; the exact relation is dependent on several factors, including the target density, the incident beam flux, the detector efficiency and several geometric effects. If we ignore these for a moment and imagine two identical, perfectly aligned detectors, Eqn. 1.82 simplifies to:

$$\varepsilon = \left[\frac{N_L - N_R}{N_L + N_R}\right] = \left[\frac{\frac{N_L}{N_R} - 1}{\frac{N_L}{N_R} + 1}\right]. \tag{1.86}$$

where N_L and N_R are the number of counts received in the left and right detectors, respectively. One can see that the instrumental effects do *not* cancel from the asymmetry. In real experimental situations, however, the differences in the detectors cannot be ignored, though their effects can be canceled by the following means. The previous equations assume a single spin state. If measurements are taken in both spin states, we can define the scattering asymmetry in the following way

$$\varepsilon = \frac{\alpha - 1}{\alpha + 1}, \tag{1.87}$$

where

$$\alpha = \sqrt{\frac{N_{L\uparrow} \cdot N_{R\downarrow}}{N_{L\downarrow} \cdot N_{R\uparrow}}}. \tag{1.88}$$

Here $N_{L\uparrow}$ is the yield in the left detector for spin "up" particles and the definitions of $N_{R\uparrow}$, $N_{L\downarrow}$ and $N_{R\downarrow}$ follow similarly. This definition will cause the detector-dependent factors to cancel from the asymmetry. The analyzing power then becomes

$$A_y = \frac{1}{p_i}\,\varepsilon = \frac{1}{p_i}\left(\frac{\alpha-1}{\alpha+1}\right). \tag{1.89}$$

The data were taken in this method, with the incident neutron spin flipped at a rate of 10 Hz during the course of a measurement (see Sec. 2.6.3).

Chapter 2

Experimental Setup

2.1 Overview

The experiment was performed at the Triangle Universities Nuclear Laboratory. A DC beam containing both vector and tensor-polarized deuterons was created using the Atomic Beam Polarized Ion Source (ABPIS), accelerated through the lab's 10 MV FN Tandem Van de Graaff accelerator and directed, via a switching magnet, to the Shielded Neutron Source (SNS) target area. Here a beam of polarized neutrons was created via the $^2\mathrm{H}(\vec{d},\vec{n})^3\mathrm{He}$ polarization-transfer reaction and tightly collimated through a heavy-metal shielding wall onto the hydrogen target. A plan of the laboratory showing the location of the experiment is shown in Fig. 2.1 and a detailed view of the Shielded Neutron Source area including the experimental setup is shown in Fig. 2.2. The detector array included 5 pairs of liquid scintillator neutron detectors surrounding an active target; these were used for the np experiment. Directly behind this detector array a high-pressure ^{4}He gas cell and a 6^{th} pair of neutron detectors were used to continuously monitor the neutron polarization during the experiment.

The data were collected using the TUNL XSYS data acquisition system, which allowed both for storing the incoming data events directly to tape for later analysis as

Figure 2.1: Floor plan for the Triangle Universities Nuclear Laboratory. The *np* analyzing power experiment was performed at the Shielded Neutron Source located on the 20° beamline of the analyzing magnet (labeled MAGNET #1 in the figure).

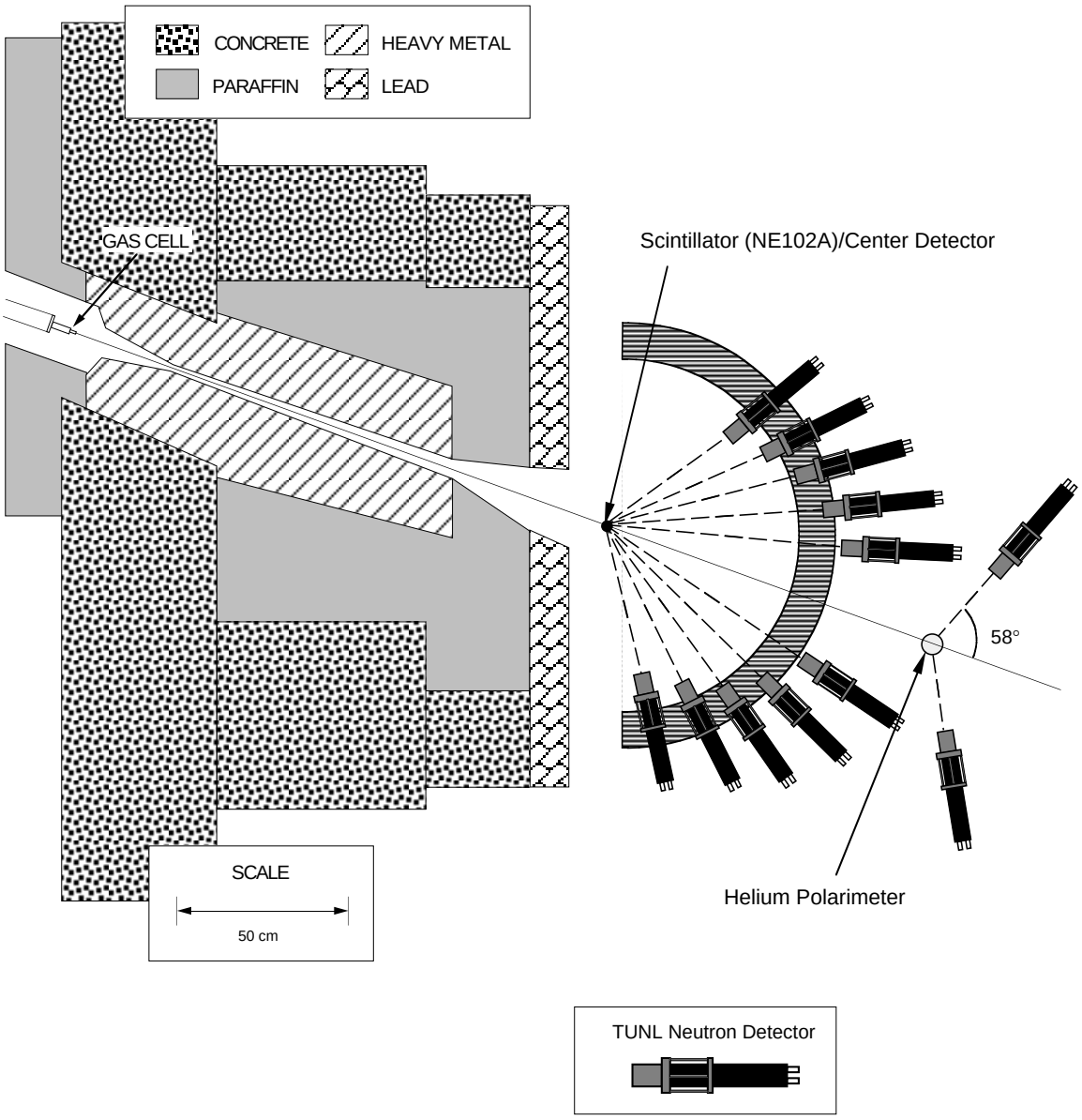

Figure 2.2: Experimental setup for np analyzing power measurement. Shielded Neutron Source (SNS) is off the 20° beam port of the analyzing magnet at the high-energy end of the accelerator.

well as for performing a complex online analysis. The data were taken over a period of approximately 9 months, with the majority of the beam time going towards the statistical accumulation of the np data. Setup and tuning times were kept to a minimum, mainly through the use of a dedicated electronics setup and a dedicated experimental area.

2.2 Polarized Source

The polarized deuteron beam for the experiment was provided by the TUNL Atomic Beam Polarized Ion Source (ABPIS) which is described in detail in the references [Cle95b], [Din95], [Cle95a]. A detailed diagram of the source is shown in Fig. 2.3. The ABPIS source is capable of producing high-intensity beams of vector-polarized hydrogen as well as both vector and tensor-polarized deuterium; for the present work a vector-polarized deuteron beam was required. The source produces the beam by dissociating the molecular bond of deuterium by means of an rf discharge. The neutral atomic beam then drifts from the tube towards the spin-transition section of the source. Only the axial component of the beam is desired, since no beam acceleration or focusing is performed till after spin selection has occurred. This axial component is first selected by means of a copper nozzle which is cooled and coated with nitrogen to prevent molecular recombination. A narrow skimmer then further restricts the beam component admitted to the spin-selection region.

After passing through the skimmer (see Fig. 2.3) the beam enters the spin-selection region. The source uses adiabatic fast passage transition units which take advantage of the coupling of the nuclear spin, $\vec{I}$, to the orbital electron spin, $\vec{S}$, in order to select states with certain nuclear polarization. As shown in Fig. 2.4, a magnetic field causes splitting of the different quantum configurations of the deuterium. Due to the strong coupling of the magnetic moment of the electron to the external field, there is a large energy separation between the states with different electron spin projections ($m_s = \pm\frac{1}{2}$). Coupling between the electron's and deuteron's magnetic moments causes an additional hyperfine splitting, with the energy being higher for states in which the spin projections are aligned. These

Figure 2.3: TUNL High-Intensity Atomic Beam Polarized Ion Source (ABPIS).

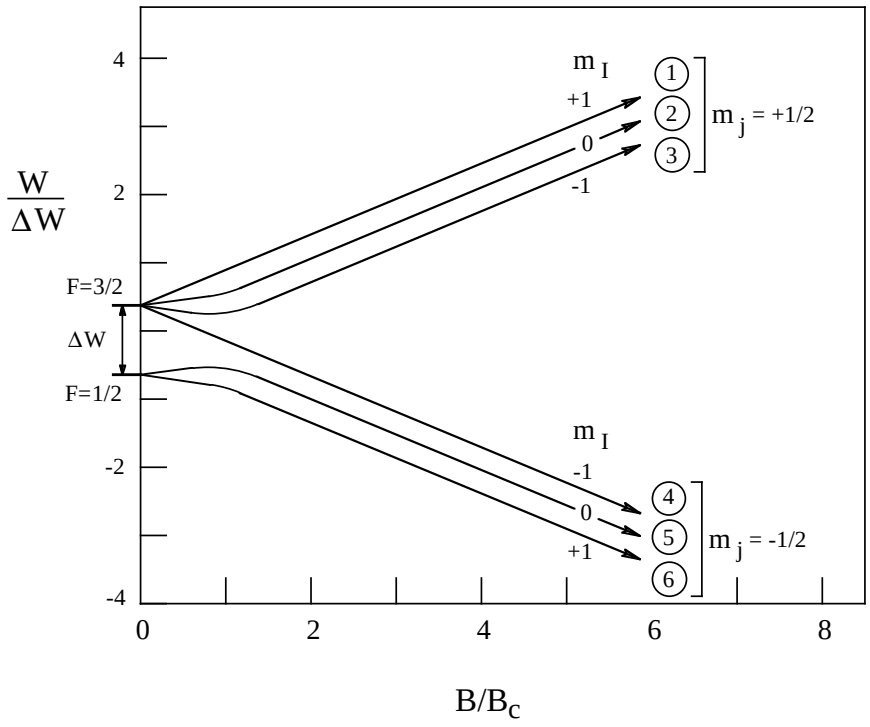

Figure 2.4: Breit-Rabi diagram of the hyperfine splitting of degenerate levels of deuterium in a magnetic field. The energy is measured in units of hyperfine splitting, ΔW, and the magnetic field is measured in terms of the critical field, B_c. Values used in the polarized source are $\Delta W/h = 327.4$ MHz and $B_c = 6.3$ mT.

states are labeled 1–6.

By passing the beam through a magnetic field, the degenerate energy levels of the coupled total spin, $\vec{J}$ are separated. An rf signal can then be used to couple two states with different $\vec{I}$ and $\vec{S}$. The TUNL source uses three separate transition units and two sextupole magnets, arranged as shown in Fig. 2.5 to select an appropriate combination of level transitions to give a polarized proton or deuteron beam. The sextupole magnets act as Stern-Gerlach filters which defocus away beam in the $m_s = -\frac{1}{2}$ state. Transitions between states will invert the populations of the two states. By preparing the beam in the $m_s = +\frac{1}{2}$ states, transitions can be made which leave the final beam with a particular nuclear polarization. There are two types of transition units on the source, referred to as

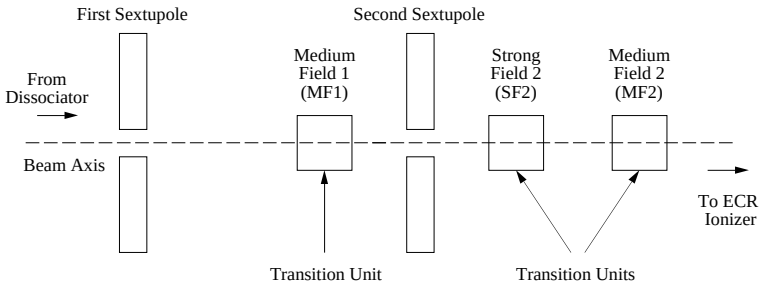

Figure 2.5: Schematic of the spin-selection region of the ABPIS showing the arrangement of rf transition units and sextupole magnets.

"strong field" (SF) and "medium/weak field" (MF) units depending on the strength of the magnetic field inside the unit. The strong field unit typically operates with a magnetic field of about 100 G and a frequency of about 400 MHz, while the medium field units operate with magnetic fields of about 30 G and a frequency from 8–12 MHz.

Due to the arrangement of the transition units on the TUNL polarized source there are several possible sets of transitions to be used to create a polarized beam, allowing one to choose between maximum theoretical polarization and maximum beam output, depending on the needs of the experiment. Table 2.1 shows the various available transitions for a deuterium beam. For the *np* experiment it was desired to have as large of a vector polarization as possible.

Thus for the "spin up" state, MF1 was used to produce the transitions $3 \rightarrow 4$ and $2 \rightarrow 3$ with SF2 providing $3 \rightarrow 6$. In this transition, the two transitions lie close enough that they cannot be experimentally separated. This set of transitions yielded a theoretical maximum polarization of $P_z = +1$, where P_z is defined as

$$P_z = \frac{N_\uparrow - N_\downarrow}{N_\uparrow + N_\downarrow + N_0}, \tag{2.1}$$

where $N_\uparrow$ and $N_\downarrow$ are the number of atoms with nuclear spin projections of $+\frac{1}{2}$ and $-\frac{1}{2}$, respectively, and N_0 is the number of remaining unpolarized atoms. For ideal transitions this value would be $+1$, but the transitions were affected by stray magnetic fields within the transition cavities. For the "spin down" state, the MF1 unit again provided the $3 \rightarrow 4$,

MF1	SF2	MF2	States Obtained	P_z	P_{zz}	I	P_z^2I
$3 \rightarrow 4$	$2 \rightarrow 6$	-	1+6	+1	+1	$\frac{2}{3}$	$\frac{2}{3}$
$3 \rightarrow 4$,$2 \rightarrow 3$	$3 \rightarrow 6$	-	1+6	+1	+1	$\frac{2}{3}$	$\frac{2}{3}$
$3 \rightarrow 4$	-	WF	3+4	-1	+1	$\frac{2}{3}$	$\frac{2}{3}$
$3 \rightarrow 4$,$2 \rightarrow 3$,$1 \rightarrow 2$	-	$3 \rightarrow 6$,$2 \rightarrow 3$,$(1 \rightarrow 2)$	3+4	-1	+1	$\frac{2}{3}$	$\frac{2}{3}$
WF	-	$3 \rightarrow 6$,$2 \rightarrow 3$,$(1 \rightarrow 2)$	3+4	-1	+1	$\frac{2}{3}$	$\frac{2}{3}$
-	$3 \rightarrow 6$	-	1+2+6	$+\frac{2}{3}$	0	1	$\frac{4}{9}$
-	$3 \rightarrow 6$	$2 \rightarrow 3$	1+3+6	$+\frac{2}{3}$	0	1	$\frac{4}{9}$
-	-	$3 \rightarrow 4$,$2 \rightarrow 3$,$1 \rightarrow 2$	3+4	$-\frac{2}{3}$	0	1	$\frac{4}{9}$
-	-	WF	2+3+4	$-\frac{2}{3}$	0	1	$\frac{4}{9}$
-	$1 \rightarrow 6$	$3 \rightarrow 4$,$2 \rightarrow 3$	3+4+6	$-\frac{2}{3}$	0	1	$\frac{4}{9}$
-	$3 \rightarrow 4$	$2 \rightarrow 3$,$1 \rightarrow 2$	2+3+4	$-\frac{2}{3}$	0	1	$\frac{4}{9}$

Table 2.1: Possible vector-polarized beam configurations for deuterium beam on the TUNL ABPIS. The "WF" indicates the medium field unit acting as a weak field transition unit (transitions $1 \rightarrow 4$, $2 \rightarrow 3$, $5 \rightarrow 6$).

$2 \rightarrow 3$ transitions while the MF2 unit was tuned to the $1 \rightarrow 4$ transition. Here the theoretical maximum polarization was also $P_z = -1$. In addition, both of these sets of transitions had theoretical maximum tensor polarizations of $P_{zz} = +1$, where the tensor polarization was defined as

$$P_{zz} = \frac{1 - N_0}{N_\uparrow + N_\downarrow + N_0}. \tag{2.2}$$

This tensor component of the beam was accepted since the polarization was the same for both vector spin states and would have a small effect on the polarization transfer to the neutrons.

As mentioned earlier, the TUNL polarized sources has the capacity to perform a "fast" spin flip. The transition units, which sit at the ∼72 kV frame voltage, were linked to the ground-potential electronics via fiber-optic links. This allowed the individual transition units to be switched on and off from a panel in the control room. A custom-built electronics module driven by a clock signal from the VAX computer was used to flip the spin state of the deuteron beam at a rate of 60 Hz. As opposed to simply switching repeatedly between the "up" (↑) and "down" (↓) spin states a more complex spin sequence was chosen. In this sequence the spin states were flipped according to the following sequence, ↑↓↓↑↓↑↑↓. This

eight-step sequence was chosen in order to cancel linear and quadratic time drifts in the detectors [Rob81a].

After the spin transition region, the beam is prepared for acceleration by an electron cyclotron resonance (ECR) ionizer. This consisted of a plasma driven by microwave radiation which would ionize the atomic beam with minimal effect on the beam polarization. The plasma consisted mainly of nitrogen buffer gas fed into the ionizer at a constant rate, the ionized deuterium alone being insufficient to maintain the plasma. The plasma was contained in the ionizer region by a magnetic bottle created by an arrangement of permanent magnets. Electrostatic lenses were used to extract the positively charged beam from the ionizer region.

For injection into the Van de Graaff accelerator, a negatively charged beam was required. Immediately after the extraction lenses a cesium charge-exchange oven converted the positively charged beam to a negatively charged one by the addition of two electrons. The oven's efficiency was only about 15%; however this factor was overcome by the high intensity of the positive beam (approximately 80 μamps) which still allowed for sufficient negative beam with which to perform the experiment.

At the end of the source a Wien filter was used to rotate the spin axis of the beam exiting the source into the direction desired at the target. In addition, spin precession through the beam leg bending magnets could be corrected for by calculating the effect using the code, PRECESS [Bla92]. For the present experiment, the spin axis was required to be along the y-axis (perpendicular to the beam pipe and parallel to the bending magnet fields), and no corrective spin precession was required. On either side of the Wien filter assembly, accelerator tubes accelerated the beam into the low-energy beam transport area by the ABPIS frame voltage of 72 kV.

2.3 Beam Transport

After leaving the ABPIS, the beam (now at ∼72 keV) was bent onto the axis of the Van de Graaff accelerator by a 30° analyzing magnet. The low energy beam pipe (see Fig. 2.1) contained a magnetic quadrupole, several magnetic steerers, and two Einzel lenses which were used to align and focus the beam with respect to the accelerator. Typically beam currents of ∼3 μamps were obtained on the low-energy Faraday cup, located immediately before the accelerator.

The accelerator was a High Voltage Engineering FN tandem Van de Graaff accelerator, with accelerator tubes capable of reaching a potential of 10 MV on the terminal. This terminal was kept charged by two charging chains located at either end, and the potential was regulated at the terminal by a corona current feedback system. The negatively charged beam (in this case D^-) was injected at the low-energy end and accelerated towards the terminal where a thin carbon foil stripped two electrons from the D^- ions, causing the then positively-charged beam to be accelerated away from the terminal. This type of accelerator thus doubles the available terminal potential, at the expense of some loss of efficiency due to the electron stripping. For the $E_n = 12$ MeV experiment, the deuteron beam was accelerated to an energy of 9.396 MeV. This value was calculated, taking into account the energy loss in the deuterium gas cell (at a given gas pressure), to produce a 12 MeV neutron beam at the center of the gas cell. For the $E_n = 7.6$ MeV experiment, a deuteron beam of energy 5.004 MeV was used.

Immediately after the tandem accelerator, a short high-energy beam transport section contained an electrostatic steerer and magnetic quadrupole, which were used to further steer and focus the beam through the analyzing magnet (see Fig.2.1) to the target area. The SNS was located almost immediately (∼6 m) after the analyzing magnet on the 20° port; with such a short beam pipe only one additional steerer was available for beam tuning. However due to the slight angle and short pipe, good transmission through the analyzing magnet was achieved.

2.4 Neutron Production

Neutrons for the experiment were produced via the $^2\mathrm{H}(\vec{d},\vec{n})^3\mathrm{He}$ polarization transfer reaction. The cross section and polarization-transfer coefficient of this reaction are strongly peaked at 0°. While the neutron beam produced is not monoenergetic, the neutrons from this reaction are separated from the neutrons produced by the deuteron breakup processes by a positive Q-value of 3.269 MeV as well as the -2.226 MeV required for deuteron breakup on the tantalum beam stop at the end of the beam line. The deuterium gas cell (shown in Fig. 2.6) sat at the end of the 20° beam line. The gas was separated from the vacuum in the beam line by a 0.25 mil Havar foil. The deuteron beam was stopped by a 0.051 cm thick gold beam stop soldered onto the end of the gas cell. Air and water cooling were used to keep the current (typically from 1–2 μamps) on the beam stop from damaging either the beam stop or the Havar foil. The beam stop was electrically isolated from the beam pipe, allowing the charge to be collected by a charge current integrator located in the control room. The interior of the gas cell measured 3.16 cm long with a radius of 0.24 cm. The gas pressure was kept constant to give a constant energy spread during the experiment; for the 12 MeV neutron beam, a gas cell pressure of 7.8 atmospheres was used to produce an approximately 400 keV spread in the incident neutron beam energy. For the 7.6 MeV neutron beam a gas pressure of 5 atmospheres yielded a spread of ∼500 keV.

The gas cell was encased in a heavy-metal (lead and iron) shielding wall built into the original concrete shielding wall. The neutron beam was directed down a ∼1 m long collimator made of copper and polyethylene to select only that beam produced at 0°. The collimator was designed such that the target was fully illuminated by the gas cell, but hidden from the section of the collimator directly illuminated by the gas cell. Beam profile measurements (see Fig. 2.7) were made prior to the experiment to determine whether the target was fully illuminated, as partial illumination could introduce an additional asymmetry to the measurement. As can be seen the beam profile at the target was sufficient to fully cover the target with some margin for slight shifts caused by fluctuations in the beam

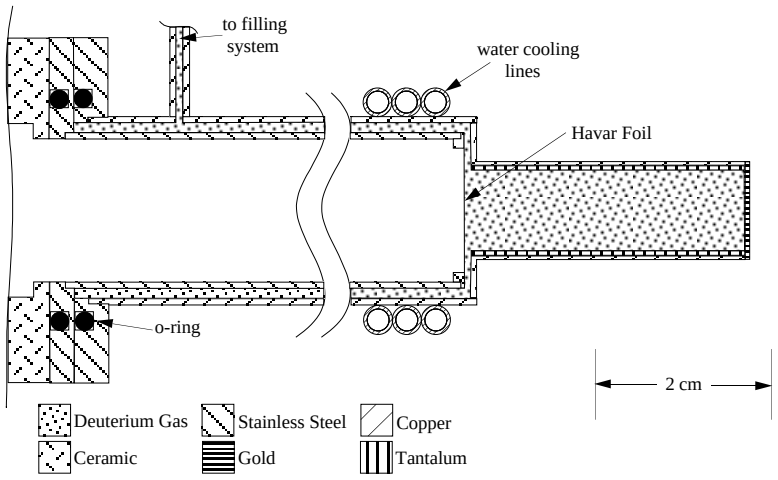

Figure 2.6: Deuterium gas cell used to produce the neutron beam via the $^2\mathrm{H}(\vec{d},\vec{n})^3\mathrm{He}$ neutron source reaction.

steering.

2.5 Detectors

The full experiment consisted of three separate detector groups: a neutron detector array used to measure the np asymmetry, a neutron polarimeter used to provide a continuous monitor of the neutron beam polarization and a deuteron polarimeter used to tune the deuteron beam from the source to its maximum polarization.

2.5.1 np Detectors

The np experimental setup consisted of an array of 5 pairs of neutron detectors surrounding the target. The target was a small, cylindrical, plastic scintillator (NE102A) of radius 0.95 cm and 3.81 cm in height and was located approximately 172 cm from the center of the deuterium gas cell. The target was mounted on the face of a photomultiplier tube, which allowed the target to be used as a center detector in coincidence with the side detectors. This greatly reduced the amount of background. As mentioned in Sec. 2.4 the target was separated from the deuterium gas cell by a heavy shielding wall with a tightly

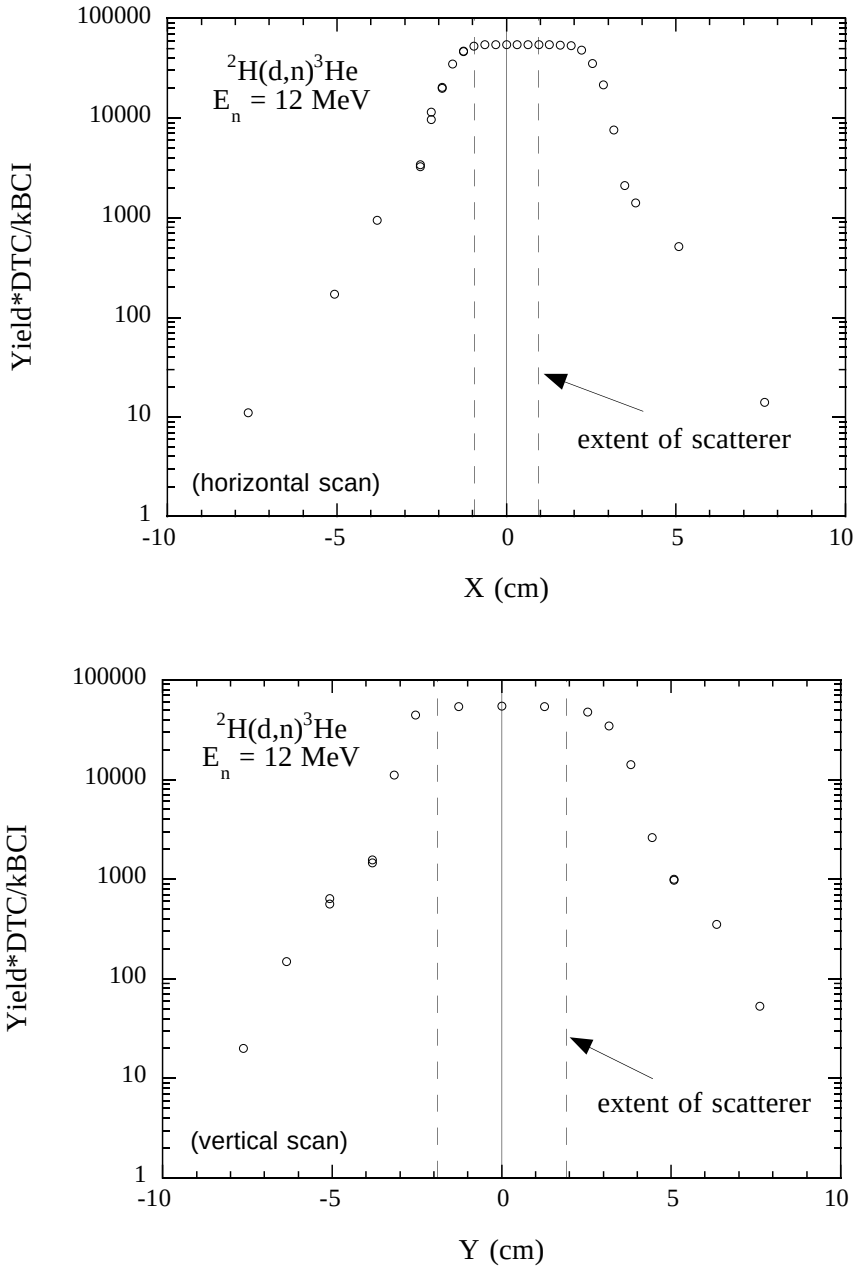

Figure 2.7: Beam-profile measurements at the shielded neutron source. Both the horizontal (top) and vertical (bottom) beam-profile measurements at the shielded neutron source are shown. X=Y=0 is the center of the target. The incident neutron beam energy is 12 MeV.

collimated opening. To prevent direct illumination of the target phototube by the beam, a small acrylic light guide (height 0.635 cm) was used to separate the target from the phototube; the light guide was the same radius as the target and did not cover the entire face of the phototube. The entire assembly was covered by a thin metal hood to insulate the phototube from external light sources.

The neutron detectors were built at TUNL and contained a liquid hydrocarbon scintillator (NE213). The detectors consisted of three parts (see Fig. 2.8): an aluminum housing containing the scintillating liquid, a phototube used to collect and amplify the emitted light, and an acrylic light guide used to join the back of the housing to the phototube. The scintillator housings, designed and constructed at Duke, were made of thin ($\sim$1 mm) aluminum in the shape of a rectangular box. The interior dimensions (active area) of the box was 7.52 cm $\times$ 4.26 cm $\times$ 11.86 cm. The rear side of the box was left open and fitted with a Pyrex glass window which was epoxied (with Torr Seal) in place. On the rear side, the aluminum frame was extended to form a bracket, which could be used to secure the detector to the phototube. Where possible, the aluminum frame was kept as thin as possible in order to avoid having large masses of metal for the incoming neutrons to scatter from. The interior surface of the scintillator box was coated with titanium oxide, in order to reflect as much light as possible from the walls towards the glass window and thus to the phototube.

To the detector, a machined acrylic light guide was attached to the Pyrex window using optical grease to assure a good optical coupling. The light guide was machined so as to join the rectangular window of the scintillator box to the round face of the phototube. The light guide was wrapped in aluminum foil in order to better reflect light back into the guide. This assembly was then mounted on Hamamatsu photomultiplier tubes (type H1161), again using the optical grease to assure a good optical coupling. The entire assembly was then wrapped in black electrical tape in order to seal the detector from external light sources. The phototube was outfitted with a circular ring, held onto the phototube's magnetic shielding

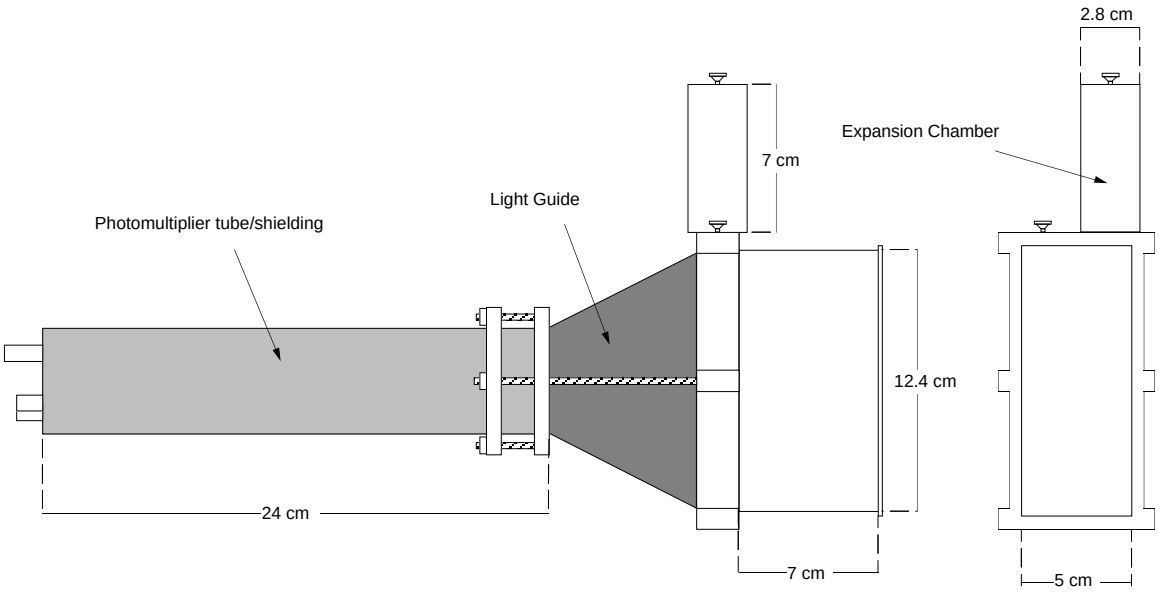

Figure 2.8: TUNL-built neutron detector.

by compression. Threaded bolts could be attached to the circular ring and the scintillator box bracket, mentioned earlier, and the entire assembly could then be held together by tightening nuts on the threaded bolts.

The assembled detectors were placed on an aluminum ring surrounding the target; each detector was held in an aluminum cradle and attached to the ring by thin ∼30 cm long aluminum rods; again the concern being to avoid large masses of metal close to the detectors. The detector ring was graduated in 1° markings allowing for accurate and consistent placing of the detectors. The cradle assembly could be moved across the surface of the ring till the appropriate angle was reached and locked in place. Great care was taken in the initial alignment of the detector ring with the beam axis; this allowed subsequent detector placement to be accurate to within the machining tolerances.

Flight paths for the neutron detectors ranged from 45 to 70 cm; the detector geometries for both the 7.6 and 12 MeV incident neutron beams is shown in Tables 2.2 and 2.3. The detectors were arranged in a staggered order, with the backward angles moved closer

$\theta_{\rm lab}$	$\theta_{\rm cm}$	Flight Path (cm)	E_n(scattered) (MeV)	Cs bias
16.0	32.1	70.0	7.02	$\frac{1}{7}$
20.0	40.1	70.0	6.71	$\frac{1}{7}$
24.0	48.1	70.0	6.34	$\frac{1}{7}$
28.0	56.1	65.0	5.92	$\frac{1}{5}$
32.0	64.1	65.0	5.46	$\frac{1}{5}$
36.0	72.1	65.0	4.97	$\frac{1}{5}$
40.0	80.2	60.0	4.45	$\frac{1}{5}$
44.0	88.2	60.0	3.92	$\frac{1}{5}$
48.0	96.2	60.0	3.39	$\frac{1}{5}$
52.0	104.2	55.0	2.87	$\frac{1}{10}$
56.0	112.2	55.0	2.37	$\frac{1}{10}$
60.0	120.2	55.0	1.89	$\frac{1}{10}$
64.0	128.2	50.0	1.45	$\frac{1}{15}$
68.0	136.2	50.0	1.06	$\frac{1}{15}$
72.0	144.2	50.0	0.72	$\frac{1}{15}$

Table 2.2: Experimental parameters at $E_n = 7.6$ MeV. Note that the detector biases given are approximate values (especially at the lowest biases).

$\theta_{\rm lab}$	$\theta_{\rm cm}$	Flight Path (cm)	E_n(scattered) (MeV)	Cs bias
16.0	32.1	70.0	11.08	$\frac{1}{2}$
20.0	40.1	70.0	10.59	$\frac{1}{2}$
24.0	48.2	70.0	10.00	$\frac{1}{2}$
28.0	56.2	65.0	9.34	$\frac{1}{2}$
32.0	64.2	65.0	8.61	$\frac{1}{2}$
36.0	72.2	65.0	7.83	$\frac{1}{2}$
40.0	80.2	60.0	7.02	$\frac{1}{3}$
44.0	88.2	60.0	6.19	$\frac{1}{3}$
48.0	96.2	60.0	5.35	$\frac{1}{3}$
52.0	104.2	55.0	4.52	$\frac{1}{4}$
56.0	112.2	55.0	3.73	$\frac{1}{4}$
60.0	120.2	55.0	2.98	$\frac{1}{4}$
64.0	128.2	50.0	2.29	$\frac{1}{9}$
68.0	136.2	50.0	1.67	$\frac{1}{9}$
72.0	144.3	45.0	1.13	$\frac{1}{9}$

Table 2.3: Experimental parameters at $E_n = 12$ MeV. Note that the detector biases given are approximate values (especially at the lowest biases).

to the target (see Fig. 2.2). This setup accomplished two things. First it helped to equalize the detector rates of the forward and backward angle detectors, so the statistical errors at all angles would be more uniform. Second it helped eliminate cross-scattering between detectors (see Sec. 3.3). Neutrons that scattered first in a lower-angle detector would be less likely to scatter to an extreme backward angle and be detected in a higher-angle detector. This was not a problem in the opposite case since the neutrons scattering first from a higher-angle detector would be significantly lower in energy, and would not fall within the kinematically accepted range in the lower-angle detector.

2.5.2 Neutron Polarimeter

In addition to the *np* setup, a 6^{th} pair of neutron detectors was used to continuously monitor the neutron polarization via the $^4\text{He}(\vec{n},n)^4\text{He}$ reaction, for which the analyzing power is well known. The target in this case was a high-pressure helium gas cell (see Fig. 2.9) with thin ($\sim$1 mm) steel walls. It was filled to a pressure of approximately 100 bar with a mixture of helium (90%) and xenon (10%) gas, the associated filling system is described in detail in reference [Wil93]. The xenon gas caused the recoiling helium nuclei to scintillate, allowing the target to be used as a center detector, similar to the *np* setup. Photomultiplier tubes were attached to both the top and bottom of the gas cell and the recoil light signals summed together. The gas cell and neutron detector pair sat on a small ring immediately behind the *np* detector ring (see Fig. 2.2, the ring is not explicitly shown).

The angles of the neutron detectors were chosen to correspond to maxima in the figure-of-merit of the n-^{4}He analyzing power. A Monte-Carlo simulation of the polarimeter setup was performed [Tor94] which calculated the effects of the experimental finite geometry and multiple scattering processes on the analyzing power. For this simulation, n-^{4}He phase shifts of Stammbach and Walter [Sta72] were used. At $E_n = 12$ MeV the detector angle was set to $\theta_{\text{lab}} = 58^\circ$ corresponding to a calculated analyzing power, $A_y(\theta) = -0.554 \pm 0.008$. At $E_n = 7.6$ MeV, the detector angle was set to $\theta_{\text{lab}} = 54^\circ$ with a simulated analyzing power

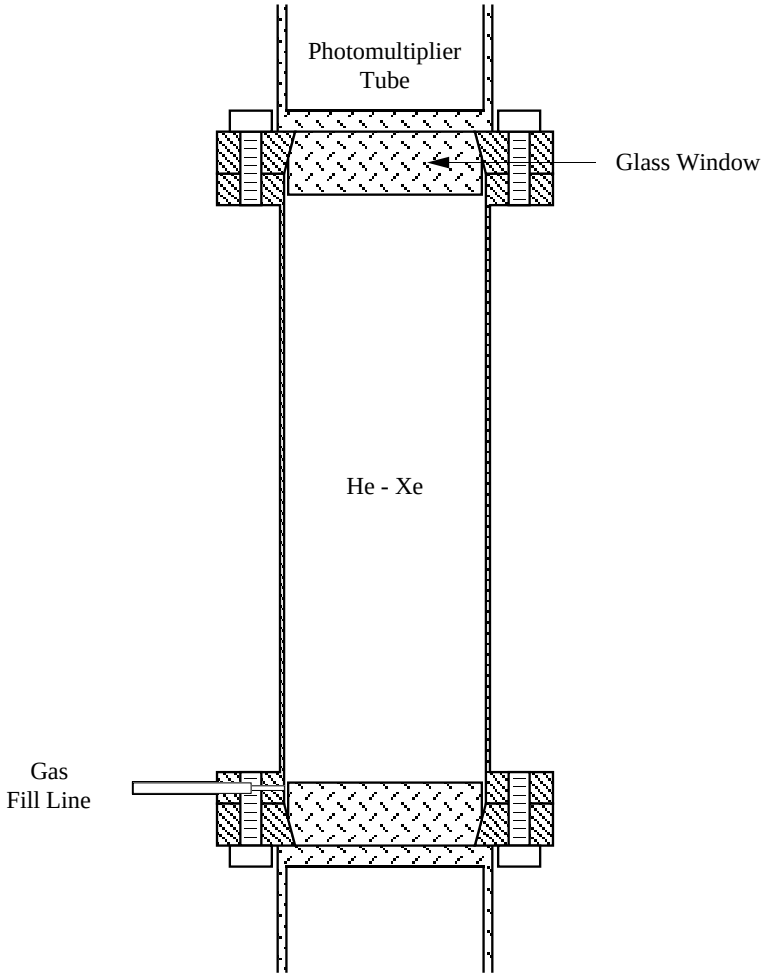

Figure 2.9: High-pressure ^{4}He gas cell.

of $A_y(\theta) = -0.615 \pm 0.009$. The error here reflects the absolute normalization uncertainty due to the uncertainty in the n-^{4}He phase shifts and is estimated to be $\sim \pm$ 1.5% for both energies.

The active target allowed the neutron polarimeter data, as with the np data, to achieve excellent suppression of background γ-ray events. At normal beam conditions (~1–2 μamps of deuteron beam at the gas cell) a 1% measurement of the neutron polarization could be accomplished in under an hour; this criterion was used to determine the length of individual runs. This length proved a good compromise between maximizing the statistics

of the data and minimizing lost data due to experimental and equipment errors.

2.5.3 Deuteron Polarimeter

For the purpose of tuning the ABPIS transition units to achieve maximum polarization, a pair of solid state detectors was used to monitor the $^{12}C(\vec{d}, p_0)^{13}C$ reaction. This measurement was performed inside a chamber mounted in the beamline just prior to the deuterium gas cell. A thin carbon foil was mounted so that it could be positioned in the beam or removed. The foil was thin enough that it did not appreciably affect the deuteron beam, yet for the actual *np* measurement the foil was removed from the beam. On either side of the foil at 122° in the reaction plane, a 1000 micron thick solid-state detector was mounted. The angle was chosen to correspond to the maximum of the asymmetry as measured by Drenckhahn [Dre77]. Each detector was mounted in a collimated holder with an adjustable slit at the end to narrowly define the reaction angle. Each detector was biased to roughly +300 V through electrically isolated feed-throughs in the chamber. The deuteron polarimeter was not used during the production runs, though the setup was kept intact so spot checks of the source transition units could be made when the polarization dropped.

This arrangement only allowed us to measure the deuteron vector polarization of the beam; no information about the tensor polarization was obtained. The neutron polarimeter (Sec. 2.5.2) provided an accurate measurement of the beam polarization. However, for the purpose of tuning the source transitions to achieve the maximum deuteron polarization, the deuteron polarimeter provided a quick and easy means. A 1% statistical measurement could be achieved in a few minutes, as opposed to approximately 45 minutes required for the neutron polarimeter. Once the apparent maxima in both spin states had been achieved, a longer run could be used to determine the actual neutron beam polarization.

2.6 Electronics

2.6.1 Neutron Side Detectors

Each side detector in the *np* detector array provided both an anode and a dynode signal. The anode signal was used to generate three signals for each event: 1) a timing signal used to determine the neutron time-of-flight (TOF), 2) a pulse-shape discrimination (PSD) signal for γ-ray rejection and 3) a trigger signal for the computer to process the event and provide routing information. Due to the large number of modules required for each detector and the numbers of detectors in the experiment, each pair of left and right detectors shared a common set of electronics. This was possible as simultaneous events in both the left and right detectors of a pair were rejected due to the inability to distinguish the center detector event of each side. The electronics for each pair of detectors were identical.

The time-of-flight (TOF) signal is the time difference between the detection of the recoil proton in the center detector and the detection of the scattered neutron in the side detector. In previous experiments at TUNL this difference was generated by a specialized electronics module, a time-to-amplitude converter (TAC), with the resulting amplitude being digitized. For this experiment a 16-input Phillips Model 7186 time-to-digital converter (TDC) was used. This device generates a digitized output based on the time difference between a common start signal and the stop signals for each of its 16 input channels.

Fig. 2.10 shows the electronics setup used to process the anode signals for each pair of side detectors. To generate the TOF stop signal, each anode signal was sent to its own constant-fraction discriminator (CFD). This produced a fast logic signal triggered on the rising edge of the signal; it is triggered when the signal reaches a certain fraction of the peak signal. For transport from the electronics rack to the computer interface, a pair of discriminators at each interface was used to regenerate the timing signals. This arrangement also provided for faster setup of the experiment, the computer interface for the side detectors required only a set of patch cables from the discriminator to the TDC.

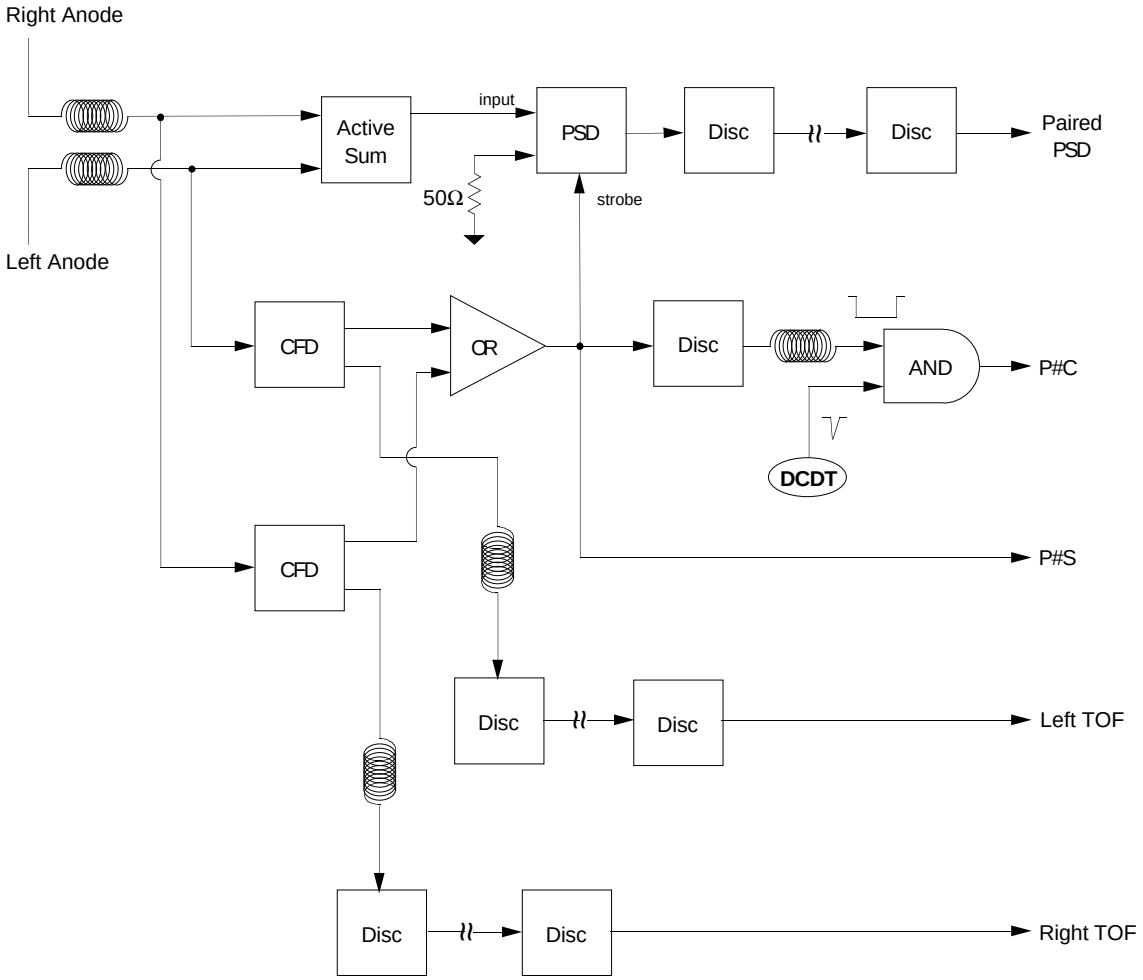

Figure 2.10: Side Detector anode electronics.

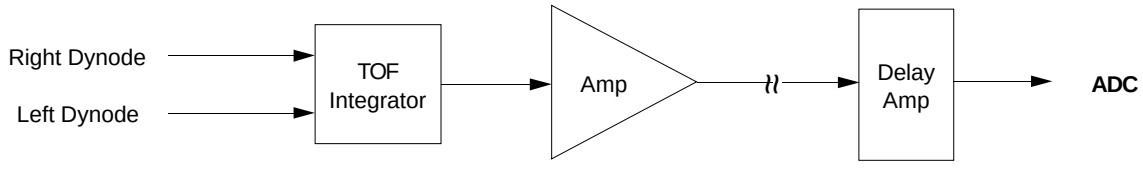

Figure 2.11: Side Detector dynode electronics.

Pulse-shape discrimination (PSD) was used to discriminate against γ-ray induced events. Certain scintillating materials (including the NE213 liquid used in our detector) give different light decay times for γ rays and neutrons. The anode signals of the left and right detectors were summed in a LeCroy 428F linear fan-in and sent to the input of a Canberra 2160 PSD module. This signal was strobed by the output of the CFD to produce a delayed output whose delay was proportional to the decay time of the of light signal. This signal was then sent to the computer interface to the inputs of the TDC. As with the TOF signals, the doubles trigger provided the common stop for the TDC. Dissimilar to the TOF signals, one TDC channel was used for both left and right detectors with the detector routing signal used to differentiate between left and right detector events.

The CFD output was also used to create two additional signals: a routing signal indicating which particular pair of detectors had fired (label `P#S`) and a side detector center detector coincidence signal (label `P#C`). The former signal was simply OR-ed with the other detector pair signals and the delayed CFD output of the center detector to provide a delayed center detector trigger (`DCDT`). This `DCDT` was AND-ed with the output of the two side detector CFD's to produce the latter signal. This signal allowed for rejecting events due to the high rate of the center detector ($\sim$50 kHz) unless there was a corresponding side detector event with the correct timing.

The side detector dynode signal was used to measure the pulse height produced by the scattered neutron. The left and right detector dynode signals were summed together in an integrating preamp and sent to a linear amplifier. The amplified signal was sent to the computer interface, through a delay line amplifier and to the input of a 4 input 13-bit EG&G Ortec AD413A analog-to-digital converter (ADC). The delay amplifier was used to align the energy signals with the gate signal provided by the trigger electronics (see Sec. 2.6.4).

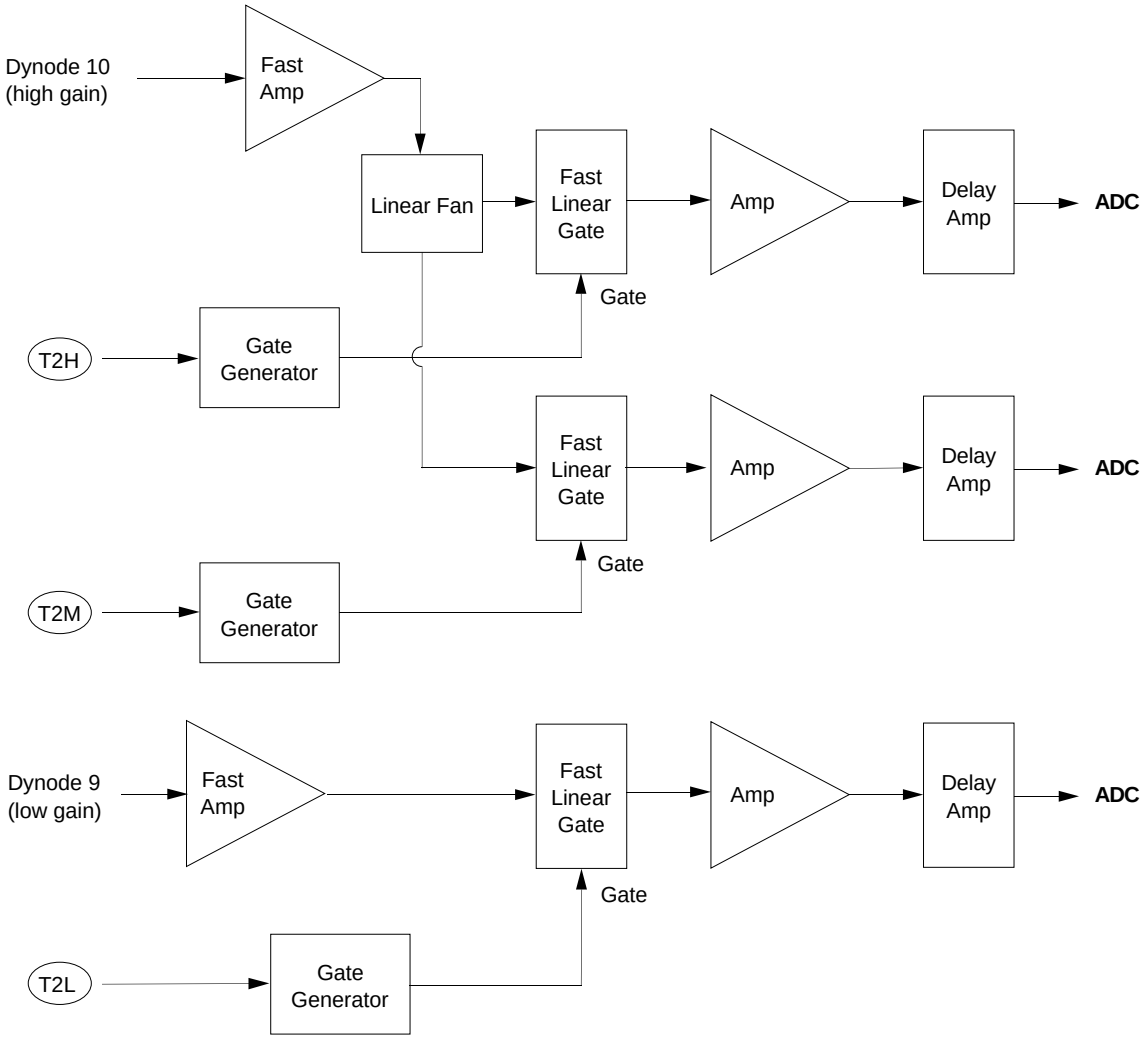

Figure 2.12: Center Detector dynode electronics.

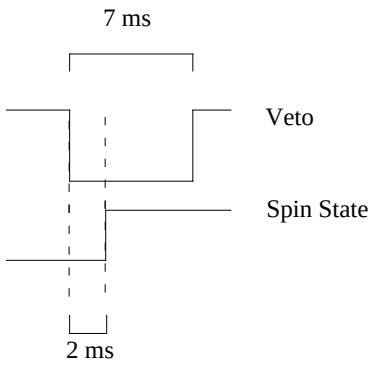

Figure 2.13: Spin-veto coincidence.

2.6.2 Center Detector Electronics

Due to the large angular range of the detector array, and thus the large range of scattered proton energies in the center detector, providing a clean center detector energy signal was not trivial. At the smaller angles, the low proton recoil energy required a high gain in order to be separated from the background noise. At larger angles a lower gain was desired to prevent saturation in the phototube and the associated electronics. Thus it was necessary to have more than a single gain for the center detector signal. To provide the best possible signal for each detector pair, three gains were used. The dynode electronics for the center detector are shown in Fig. 2.12. Dynode signals were taken from both dynode 9 and 10 on the phototube base. These were sent through Phillips 771 fast amplifiers and then into Tenelec 308 Fast Linear Gate modules; the gate for these was generated by the trigger circuit (see Sect 2.6.4) and was used to cut down the high rate seen by the center detector. The output of the the linear gate was then amplified and sent to the ADC. As with the side detector energy signals, a delay amplifier was used to align the center detector energy signals with the ADC gate. Also at least one energy signal was sent to each of the two ADC's used, thus insuring that both ADC's would generate a Look-At-Me (LAM) signal and be read for each event.

2.6.3 Spin-Flip Electronics

The polarized source at TUNL allowed for fast spin flipping (see Sec. 2.2); this was controlled by sending logic signals to the source from a panel at the computer interface. Thus a desired spin sequence, as well as individual spin states, could be controlled by electronics in the control room. A custom TUNL spin-state controller was used to provide the desired sequence ($\uparrow\downarrow\downarrow\uparrow\downarrow\uparrow\uparrow\downarrow$) as well as drive additional electronics to control the triggering of events based on the spin state. The spin-flip electronics are shown in Fig. 2.14. The spin-state controller was driven by a 10 Hz clock signal; this gave spin states of 100 ms duration. During spin flips, when one transition unit was switched off, while another was switched on, it was necessary to halt data acquisition for a short period in order to give the beam time to stabilize. The gated clock output of the controller was sent through two Phillips 794 Gate Generators which allowed the leading edge and the duration of the veto signal to be adjusted. From previous experiments [Wil93], a veto signal of 7 ms was determined to be adequate, with the veto starting 2 ms prior to the spin flip with 5 ms for the beam to recover. A diagram of the veto-signal coincidence with the spin-flip controller signal is shown in Fig. 2.13.

The "+" and "−" outputs of the spin state controller were sent to linear fan outs. From here they were sent to the hit register to provide spin-sense information for the software sorting of events. In addition each spin-sense signal was used to increment two sets of counters in order to check the relative amount of time and beam current for each spin state. The first counters were driven by a 2.5 kHz clock signal generated by a Phillips 794 Gate and Delay generator. The coincidence of this signal with each of the spin-sense bits and the spin-veto signal was counted in a scaler. The coincidence for each spin sense was vetoed by the spin-veto signal. Similarly the coincidence of the BCI signal with each spin state (including veto) was counted. Results from both counters were consistent within statistics and showed that 7% of beam time was spent in the spin-veto state (see Fig. 2.13).

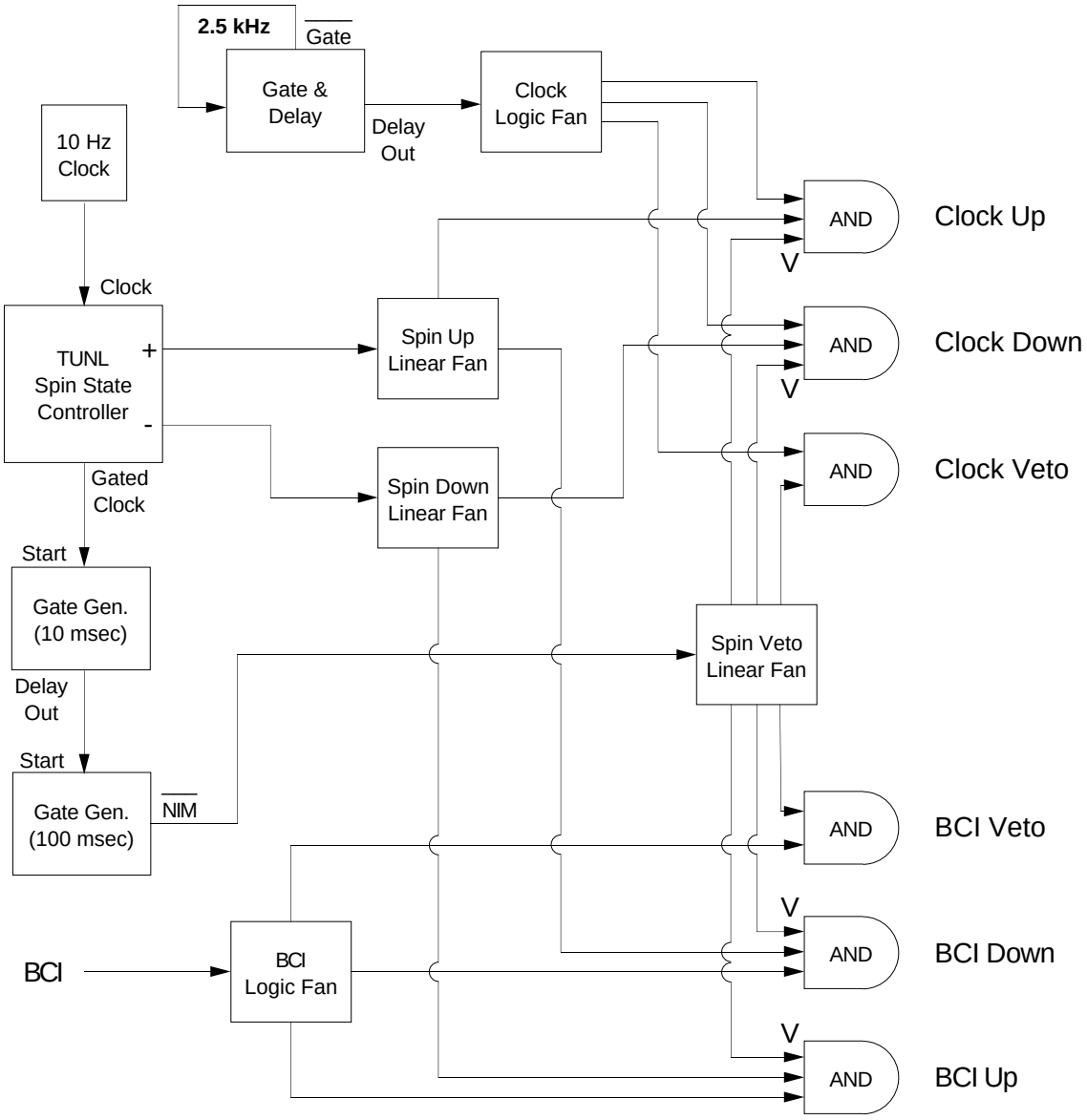

Figure 2.14: Spin-flip electronics.

2.6.4 Trigger Electronics

Due to the high rate of the center detector, it was desirable to eliminate false events before the signals were digitized. This was accomplished by requiring a coincidence between the center detector and a side detector within a certain time range. As seen in Fig. 2.10 the CFD outputs of each pair of detectors were OR-ed together and sent through a discriminator. Here the signal was widened to ∼100 ns and sent to a coincidence unit along with the trigger signal from the center detector. A short delay was used to adjust the coincidence window. This signal could then be used as a gate for the slow energy signals. As shown in Fig. 2.15 the 5 `P#C` signals were OR-ed together to provide four signals: the trigger to start the event digitization (`T1`) and the gate signals (`T2L`, `T2M`, and `T2H`) for the fast linear gate modules used by the center detector energy signals (see Fig. 2.12).

The trigger signal, `T1`, was sent to the computer interface (see Fig. 2.16) where it was fanned to produce a common stop signal for the TDC, gates for the Ortec ADC's and a strobe for the hit register. The hit register was used as the trigger for digitization, causing the CAMAC crate controller to read and reset the modules on the *np* MBD channel In addition the hit register was used to provide spin-sense information to the software by receiving inputs from the TUNL Spin-State Controller.

Trigger signals at the computer interface were vetoed by three signals: the spin veto (see Sec. 2.6.3), the hit register LAM and the crate inhibit. The spin veto prevented counting during indeterminate spin states while the hit register LAM and the crate inhibit signals prevented counting while the CAMAC modules were being read. The hit register read and cleared last so that its LAM signal would remain set until the entire event had been read.

2.6.5 Neutron Polarimeter Electronics

The neutron polarimeter electronics were similar in design to the *np* electronics. The top and bottom center detector anode signals were put in coincidence, with a small

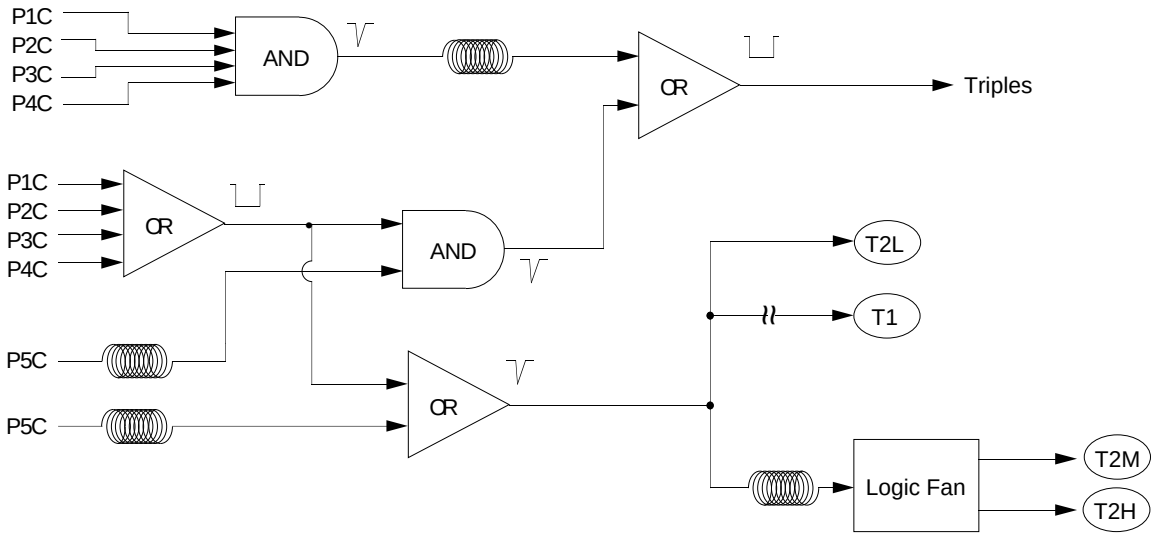

Figure 2.15: Trigger signal electronics.

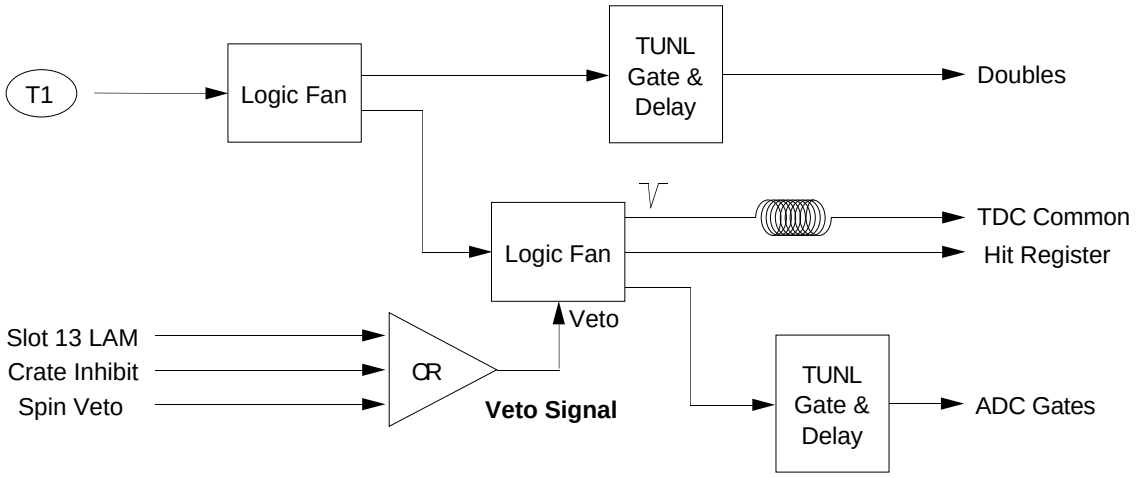

Figure 2.16: Computer interface trigger electronics.

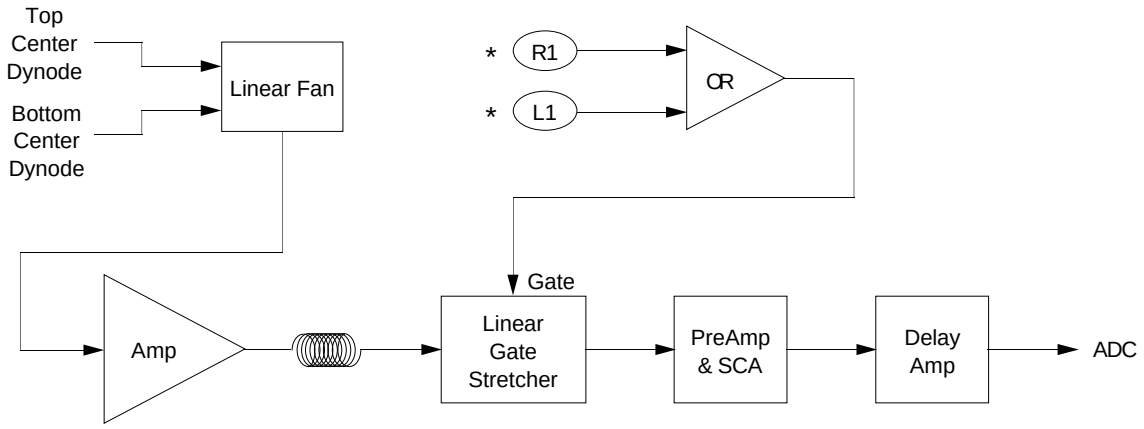

Figure 2.17: Neutron polarimeter dynode electronics. The signals `R1` and `L1` come from the side detector-center detector coincidences (see Fig. 2.18).

delay used to align the two signals (see Fig. 2.18). This center detector signal was put in coincidence with the CFD output of each side detector to generate a start signal for the Ortec Time-to-Amplitude Converter (TAC). The stop signal was provided by the top-bottom coincidence signal sent through a delay signal. The TAC signals for the left and right detectors were then sent to the computer interface and stored. In addition, the side detector anode signals were used to create a PSD signal and an energy signal. These signals were not stored in the computer, but were put in coincidence with the TAC single-channel output in a multi-input coincidence unit to generate the gate signal for the computer. This allowed a PSD cut to be made in the hardware, not requiring further processing at the computer. The cut was set by eye, so as to exclude most of the γ-ray events, however the PSD resolution of these detectors was good enough that this was not unreasonable.

The center detector dynode electronics are shown in Fig. 2.17. The top and bottom signals were again summed together and sent to an amplifier. This signal was sent to a linear gate and stretcher which was gated by an event from either a right or left center detector-side detector coincidence (signals `R1` and `L1` in Fig. 2.18). This output is then sent to the ADC to provide a recoil-energy spectrum.

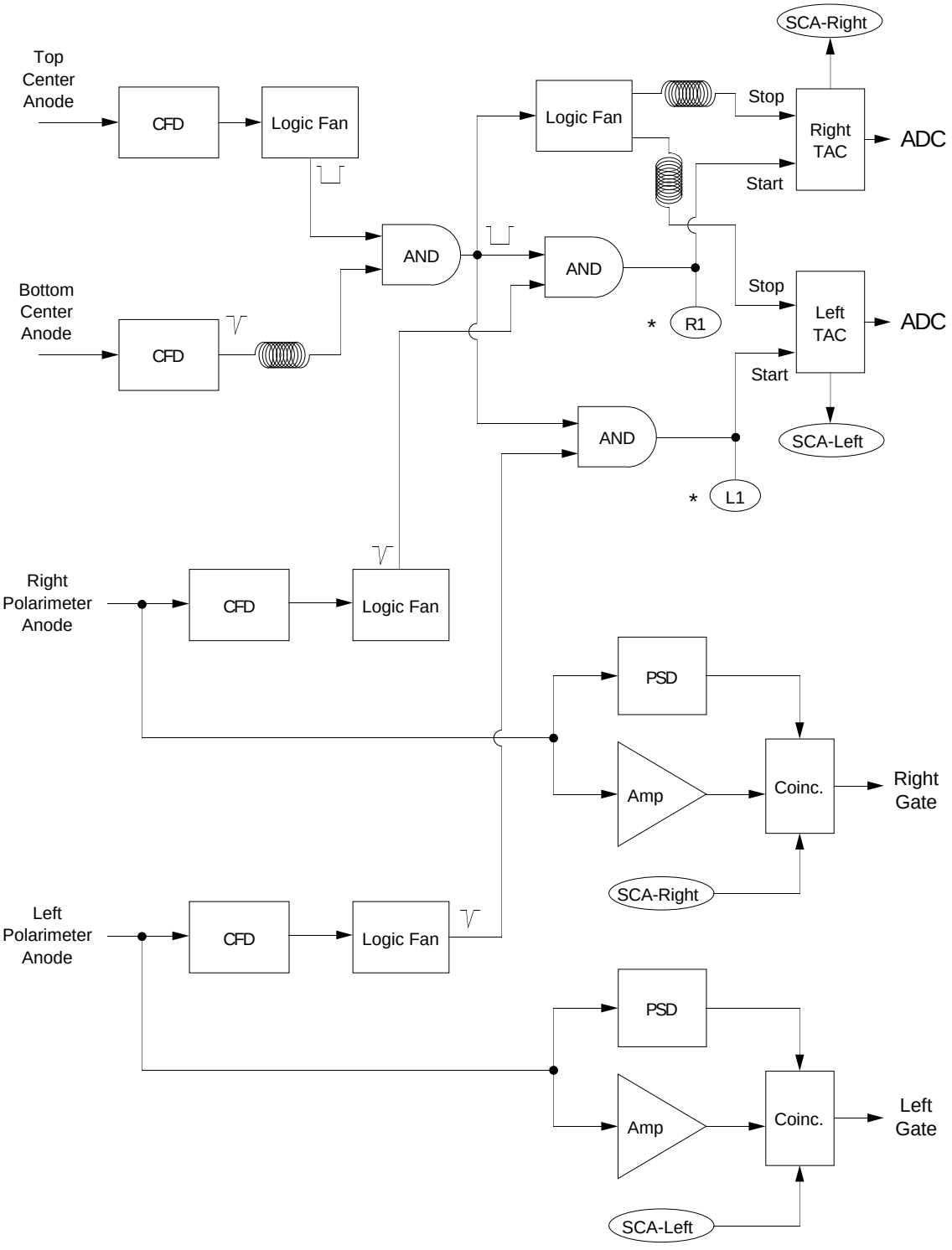

Figure 2.18: Neutron polarimeter fast electronics. The outputs `R1` and `L1` are used to gate the center detector energy signal (see Fig. 2.17).

2.6.6 Deuteron Polarimeter Electronics

The deuteron polarimeter was used to tune the transition units to achieve maximum polarization. The outputs of the solid state detectors were amplified, and the unipolar outputs summed together and stored in the computer (see Fig. 2.19). The bipolar outputs of each amplifier were sent through timing single channel analyzers to provide a gate and routing signal for the computer. This gate signal was vetoed by the same signal as the *np* electronics (see Sec. 2.6.4) in order to prevent measuring the polarization during the spin flips.

During the production runs, the deuteron polarimeter was not operated and the data acquisition was stopped to eliminate the associated computer dead time. The setup was kept intact and the detectors biased so that spot checks could be made of the deuteron polarization and if necessary, the source transition units could be retuned.

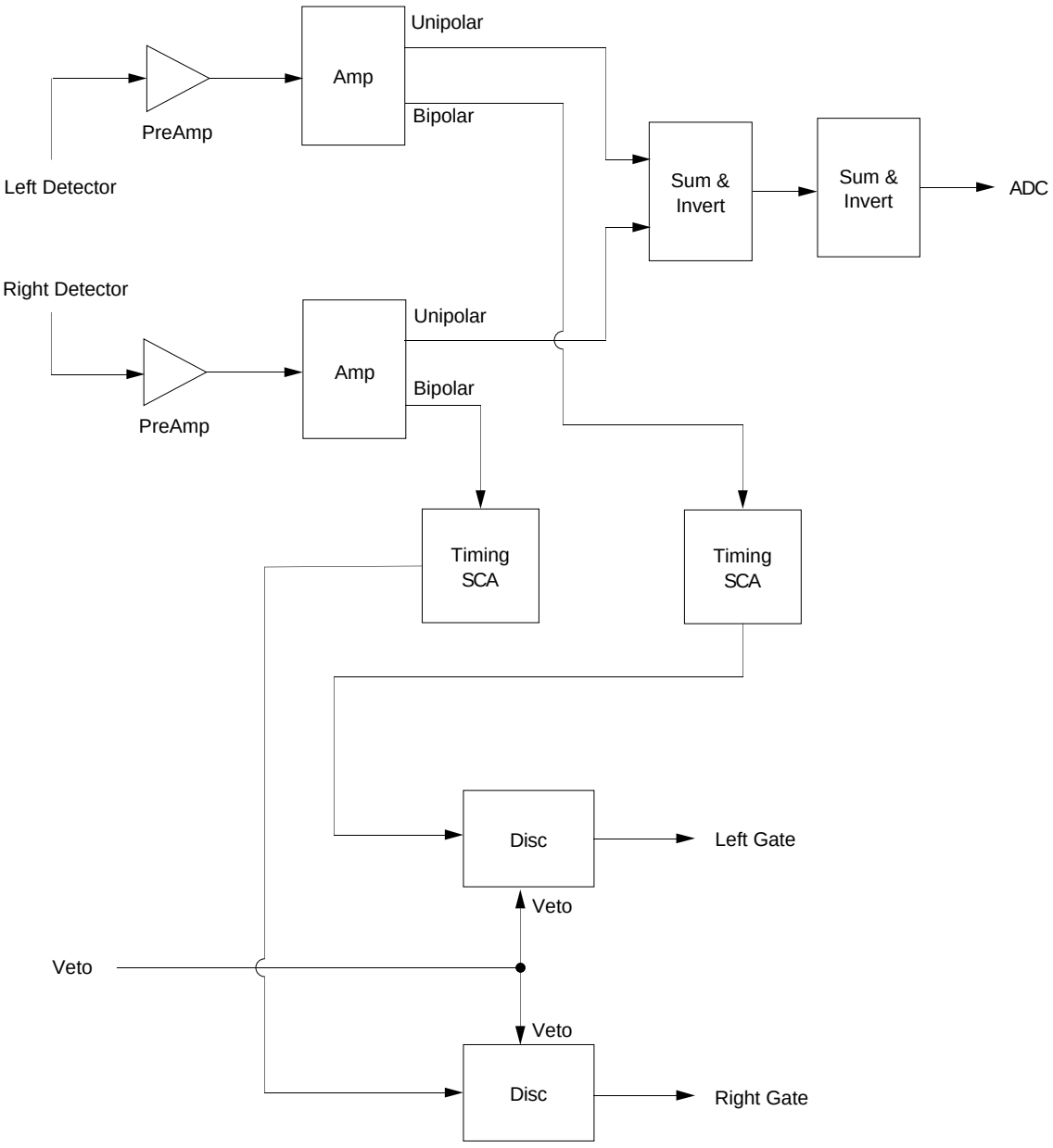

Figure 2.19: Deuteron polarimeter electronics. The veto signal shown comes from the interface electronics veto (see Fig. 2.16).

Chapter 3

Online Analysis

The TUNL XSYS Data Acquisition system [Gou81] was used for this experiment and provided for both complicated online sorting as well as tape storage of the data in "event" mode for subsequent offline sorting. This system has been developed and customized at TUNL over the years and provides many built-in analysis routines tailored to the experiments done in the lab. Additionally, user-written FORTRAN routines can be linked to the XSYS libraries, allowing the experimenters to further customize the data analysis software to their particular experiment.

The computer interface hardware consists of several CAMAC modules, including Analog-to-Digital Converters (ADC), Time-to-Digital Converters (TDC), clocks and scalers, located in two daisy-chained CAMAC crates communicating, via a Microprogrammed Branch Driver (MBD), with a μVAX 3200 workstation [Rob81b]. For each event trigger, the CAMAC crate is read and the event data words are stored in a VAX memory buffer. The MBD can send event data through up to seven different channels to the VAX; the channels are prioritized, with respect to each other, allowing certain data events to be handled preferentially. This allowed the *np* events to be processed by the computer at a higher priority than the monitor detector events, minimizing the possible computer dead time for these events. The XSYS software also allowed for events on one MBD channel to be stored

directly to an event file, typically written directly to tape, in addition to being sorted online. The *np* data was thus stored providing an immediate backup of the data which could be replayed at a later time to provide for more complicated sorting than was possible during the experiment.

The digitized events were sorted using XSYS's Event Analysis Language (EVAL), a FORTRAN-like language which allowed conditional testing to be performed on the digitized signals. The TUNL data acquisition software allows for separate routines to be written for each MBD channel, allowing for complex sorting of events from the different sets of detectors.

3.1 *np* Experiment

For the *np* detectors, the following signals were stored in common for all detector pairs: a detector pulse height (PH) for each neutron detector ($\times$10), a time-of-flight (TOF) signal ($\times$10), a pulse-shape discrimination (PSD) signal for each detector pair ($\times$5), a proton-recoil pulse height (CDPH) from the scatterer at three different gain settings, and a hit register signal providing spin-state information. The PSD signal was only stored for each pair of detectors due to a limitation of available electronics. The TOF and PSD signals were digitized by a Phillips TDC, while the side detector PH and CDPH signals were digitized by two Ortec quad-input ADC's. In addition the TDC provided a hit register which was used to determine which detector had triggered the event.

Each event was sorted in the following method: The TDC hit register signal was used to define the detector triggering the event, as well as to reject events in which multiple detectors were triggered. Next the spin-sense signal was checked to determine the current spin state. The side detector pulse height (PH), the time-of-flight (TOF), the pulse-shape discrimination (PSD) and the scatterer pulse height (CDPH) raw spectra were incremented accordingly. All signals from each detector in both spin states were stored in the analysis. However, due to the large number of data histograms required and in order to stay within the limits of the XSYS software and not overload the data acquisition computer, the CDPH

Detector	θ_{lab}	Center Gain
Pair 1	16° 20° 24°	High
Pair 2	28° 32° 36°	Medium
Pair 3	40° 44° 48°	Low
Pair 4	52° 56° 60°	Low
Pair 5	64° 68° 72°	Low

Table 3.1: Center detector gain for each detector pair. The high gain was used to pull the detector signal of the small scattering angle neutron events above a fast discriminator threshold, with subsequent saturation of the detector signal caused by larger angle neutron scattering events. The lower gains provided appropriate signals for the more backward angles.

events for both spin states were sorted into the same histogram. These histograms were split so that spin "up" events were sorted into the first 512 channels and spin "down" events were sorted in the last 512 channels.

Due to the large kinematic spread of the recoil particles, it was necessary to have three different gains for the CDPH signal. At the more forward angles ($\theta_{\mathrm{lab}} = 16^\circ, 20^\circ, 24^\circ$) an extremely high amplifier gain was required to pull the signal out of the background. The saturation of the higher voltage signals, however, made this gain unsuitable for the more backward angles. The intermediate angles ($\theta_{\mathrm{lab}} = 28^\circ, 32^\circ, 36^\circ$) required a lesser gain to separate the signals, but again, the extreme kinematic range of the setup made this second gain unsuitable for the most backward angles. All remaining angles used the lowest-gain CDPH signal.

The PSD signal was used to eliminate the γ-ray background. In the scintillating liquid used in the side detectors (NE213), light from scattered γ rays has a shorter decay time than the light produced by scattered neutrons; this difference in decay times can be used to reject the events due to γ rays. The PSD electronics (Sec. 2.6.1) produced a digitized signal proportional to the length of this decay time which was incremented to a

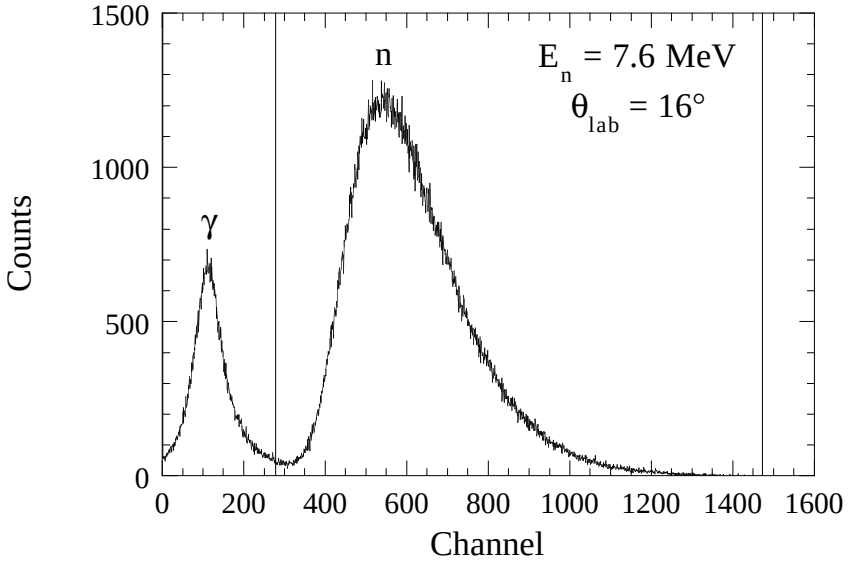

Figure 3.1: 1D Pulse-Shape Discrimination spectrum for $E_n = 7.6$ MeV and $\theta_{\rm lab} = 16°$.

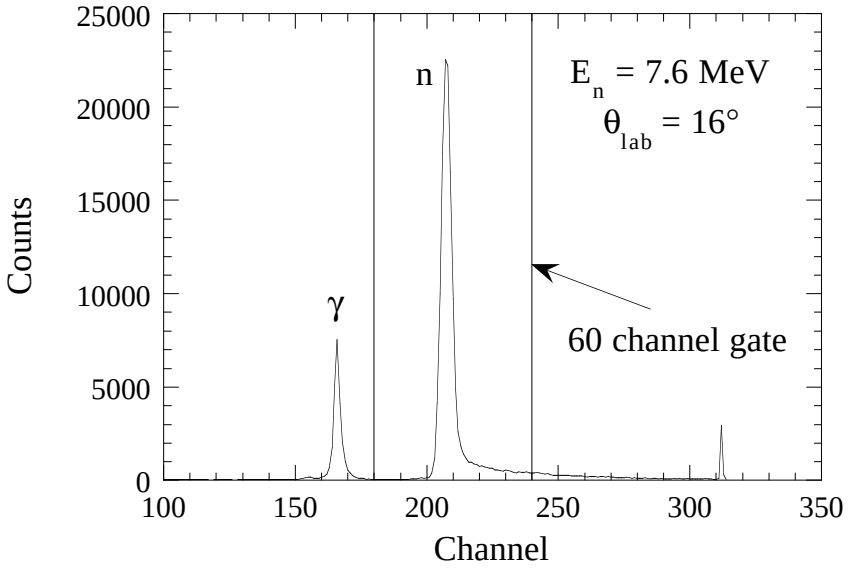

Figure 3.2: Raw Time-of-Flight spectrum for $E_n = 7.6$ MeV and $\theta_{\rm lab} = 16°$. The 60-channel gate is used to select events for 2D sorting versus the event CDPH signal.

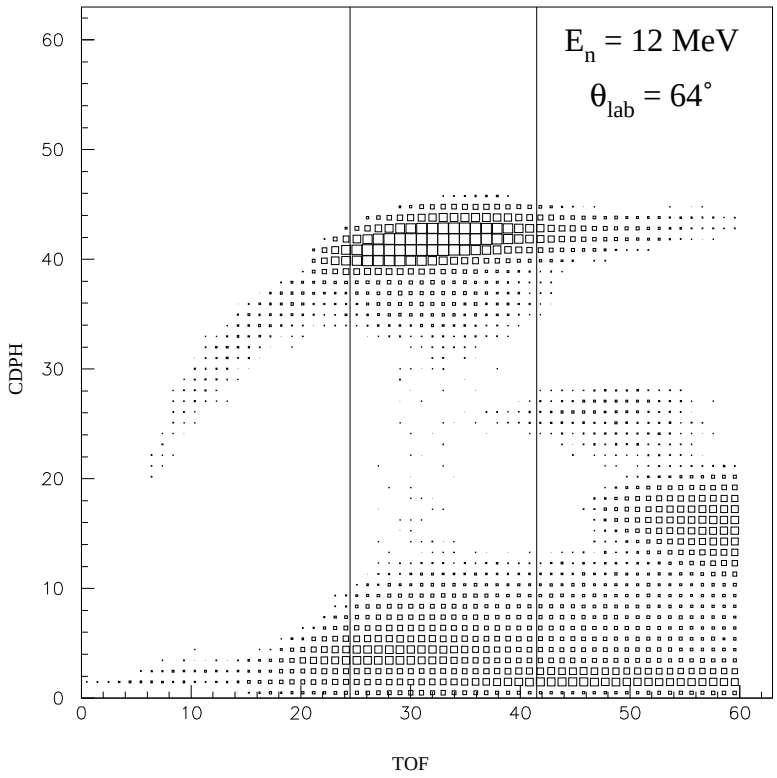

Figure 3.3: 2D spectrum of a 60-channel cut in TOF versus compressed CDPH. The spectrum shown is for $E_n = 12$ MeV and $\theta_{\rm lab} = 64°$. A gate is set around the elastic neutron peak in order to remove background events. Events within the gate are sorted to a final pulse-height spectrum at full resolution.

histogram. A gate was then set to select only those events with longer decay times. A typical spectrum and with the PSD gate is shown in Fig. 3.1. The separation between the γ peak and the neutron peak, as characterized by the depth of the valley between the two, varied from detector to detector. However, overall the PSD resolution of the detectors used in the present work was very good, as can be seen in the excellent separation between the two peaks in the figure,

Next the TOF signal of the event was evaluated; an example of the raw TOF spectrum at $E_n = 7.6$ MeV and $\theta_{\rm lab} = 16°$ is shown in Fig. 3.2. In this spectrum time

increases from left to right. The large peak near channel 210 is due to the elastically scattered neutrons; the smaller peak at channel 165 is from γ events, most of which will be rejected by the PSD cut. The small spike at channel 300 is an artifact of the signal electronics resulting from the timing window used in the TDC. The accidental background was extremely small, in large part due to the heavy shielding wall between the detectors and the the neutron source. Since the elastically scattered neutrons have the highest possible energy (and the shortest possible TOF) for neutrons associated with a given event, any neutrons arriving at shorter times must be accidental events. Accidental events have no time correlation and appear evenly distributed throughout the spectrum. It can be seen (particularly at $E_n = 7.6$ MeV) that the background due to accidentals was negligible.

From the TOF spectrum a 60-channel gate was chosen, centered on the elastic peak (see the gate in Fig. 3.2). Events passing the PSD cut and falling within this gate were incremented to a 64×64 channel 2D spectrum versus the CDPH signal. An offset, corresponding to the lower gate channel shown in Fig. 3.2, was subtracted from the TOF signal. The CDPH signal was then compressed from its full resolution of 2^9 bits to 2^6 bits in order to fit entirely within the 64 channels of the 2D spectrum; the 60-channel cut in the TOF was chosen to keep the full resolution of that signal. The 2D CDPH versus TOF spectrum for $E_n = 12$ MeV and $\theta_{\mathrm{lab}} = 64^\circ$ is shown in Fig. 3.3. The 2D spectra gave excellent separation of events with respect to the TOF and allowed for the removal of much the remaining background around the CDPH peak. A 2D gate was set around the elastic TOF peak (see Fig. 3.3), cutting at approximately 10% of the TOF peak height. Care was taken to check the raw TOF spectra (Fig. 3.2) for slight timing shifts during the course of the run. These shifts would change the position of the elastic peak within the 2D spectra, causing the 2D gates to become misaligned. If the gates in the raw TOF were adjusted, the offset to the TOF signal in the DAQ code needed to be adjusted to keep the elastic peak centered.

Events falling within this 2D gate of Fig. 3.3 were sorted to a final spectrum at the

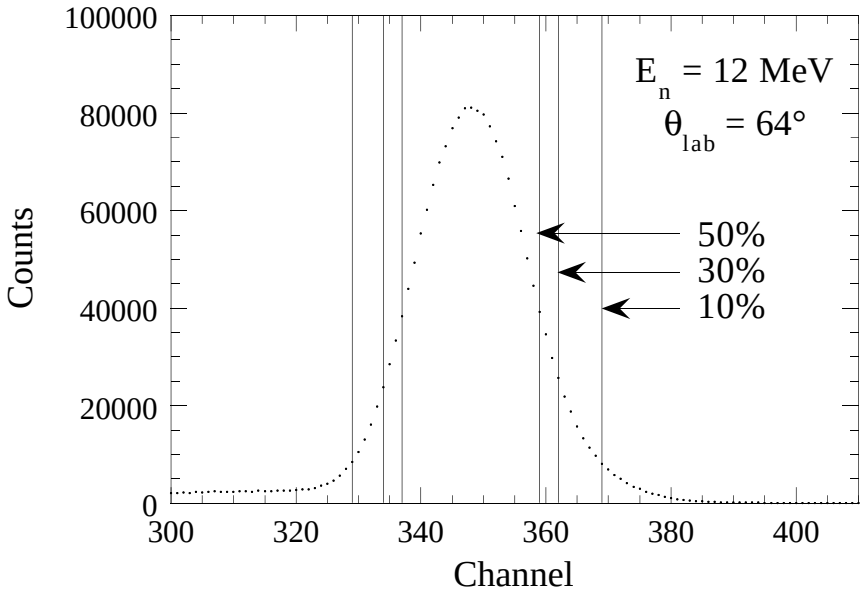

Figure 3.4: Center detector pulse-height spectrum after sorting at $E_n = 12$ MeV and $\theta_{\rm lab} = 64°$. Gates were set at 10%, 30% and 50% of the peak height to check the consistency in the asymmetries.

CDPH signal's full 2^9-bit resolution. Yields were taken from this spectrum to determine the asymmetries in the *np* scattering. Keeping these spectra at full resolution allowed for a detailed inspection of the remaining background structure. Fig. 3.4 shows the final CDPH signal at $E_n = 12$ MeV and $\theta_{\rm lab} = 64°$. Accidental events in these final spectra were negligible. In early tests of the online sorting, the accidental background from the TOF spectrum (events of shorter TOF than the γ peak in Fig. 3.2) was sorted in a similar fashion. The results were negligible and in order to conserve memory, the accidental event sorting was not performed during later runs.

The result of this sorting was a dramatic reduction in the amount of background in the CDPH spectra; this is clearly illustrated in Fig. 3.5. Here the CDPH spectrum at $E_n = 12$ MeV and $\theta_{\rm lab} = 48°$ is shown before the sorting (dotted curve) and after the sorting (solid curve). The remaining background after sorting can be seen tailing into the elastic peak from the lower channels. This background represents about 3% of the elastic

peak maximum and is composed of multiple-scattering events, scatterer edge effects and "cross-talk" from the other detectors. The treatment of this remaining background will be explained in later sections. Examples of the sorted CDPH spectra for all angles at both energies are shown in Figs. 3.6 and 3.7.

For each detector pair these sorted center detector pulse-height yields were used to calculate an asymmetry and from this, the analyzing power for the measurement. Gates in the pulse-height spectra for the left and right detectors were set separately to account for slight differences in their gain and geometry. Then yields were taken with three sets of gates. The first gate was set at 10% of peak height, the second at 30% and the final at 50%. Yields for the different spin states in each detector used the same gates. The asymmetry was given by

$$\varepsilon = \left(\frac{\alpha - 1}{\alpha + 1}\right), \tag{3.1}$$

where α is (from Eqn. 1.88)

$$\alpha = \sqrt{\frac{N_{L\uparrow} \cdot N_{R\downarrow}}{N_{L\downarrow} \cdot N_{R\uparrow}}}. \tag{3.2}$$

Here $N_{L\uparrow}$ is the yield for the spin-up state in the left detector and $N_{L\downarrow}$ is the yield for the spin-down state; similarly for the right side detector are $N_{R\uparrow}$ and $N_{R\downarrow}$. The error for the yield was taken to be purely statistical; for the left side detector in the spin-up state, this error was given by $\Delta N_{L\uparrow} = \sqrt{N_{L\uparrow}}$. From these, the error in the measured asymmetry was determined to be

$$\Delta\varepsilon = \frac{\alpha}{(\alpha+1)^2} \sqrt{\left(\frac{\Delta N_{L\uparrow}}{N_{L\uparrow}}\right)^2 + \left(\frac{\Delta N_{L\downarrow}}{N_{L\downarrow}}\right)^2 + \left(\frac{\Delta N_{R\uparrow}}{N_{R\uparrow}}\right)^2 + \left(\frac{\Delta N_{R\downarrow}}{N_{R\downarrow}}\right)^2}, \tag{3.3}$$

where again α is defined by Eqn. 3.2. The analyzing power could then be calculated, given the magnitude of the neutron polarization during the measurement. From Eqn. 1.82 the analyzing power was related to the asymmetry by the following relation

$$A_y = \frac{1}{p_i}\,\varepsilon = \frac{1}{p_i}\left(\frac{\alpha - 1}{\alpha + 1}\right). \tag{3.4}$$

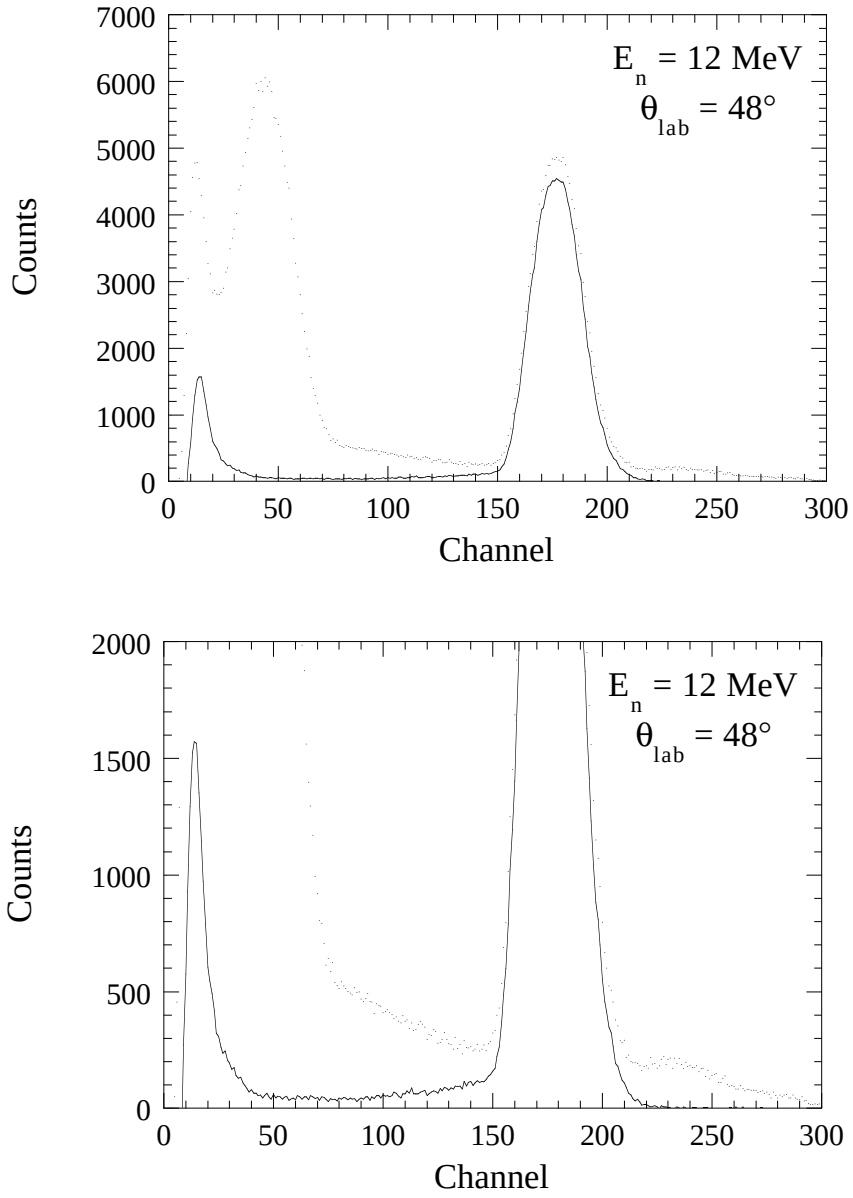

Figure 3.5: Reduction of background after online sorting. The raw data are shown by the dotted curve, the final sorted data are shown by the solid curve. Spectra shown are for $E_n = 12$ MeV and $\theta_{\rm lab} = 48^\circ$. The bottom figure shows the same data on an expanded scale.

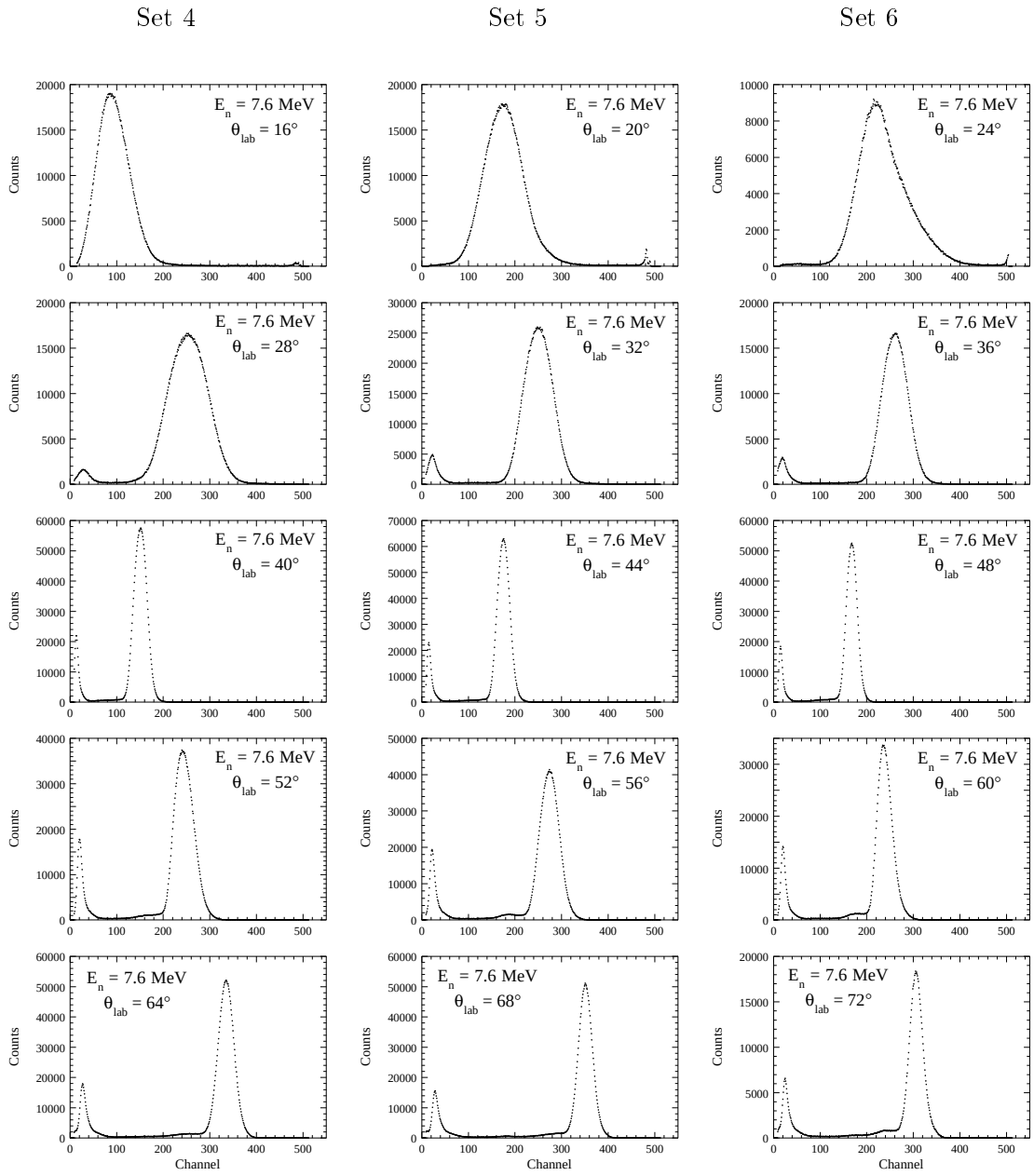

Figure 3.6: Representative center detector pulse-height (CDPH) spectra after sorting at $E_n = 7.6$ MeV.

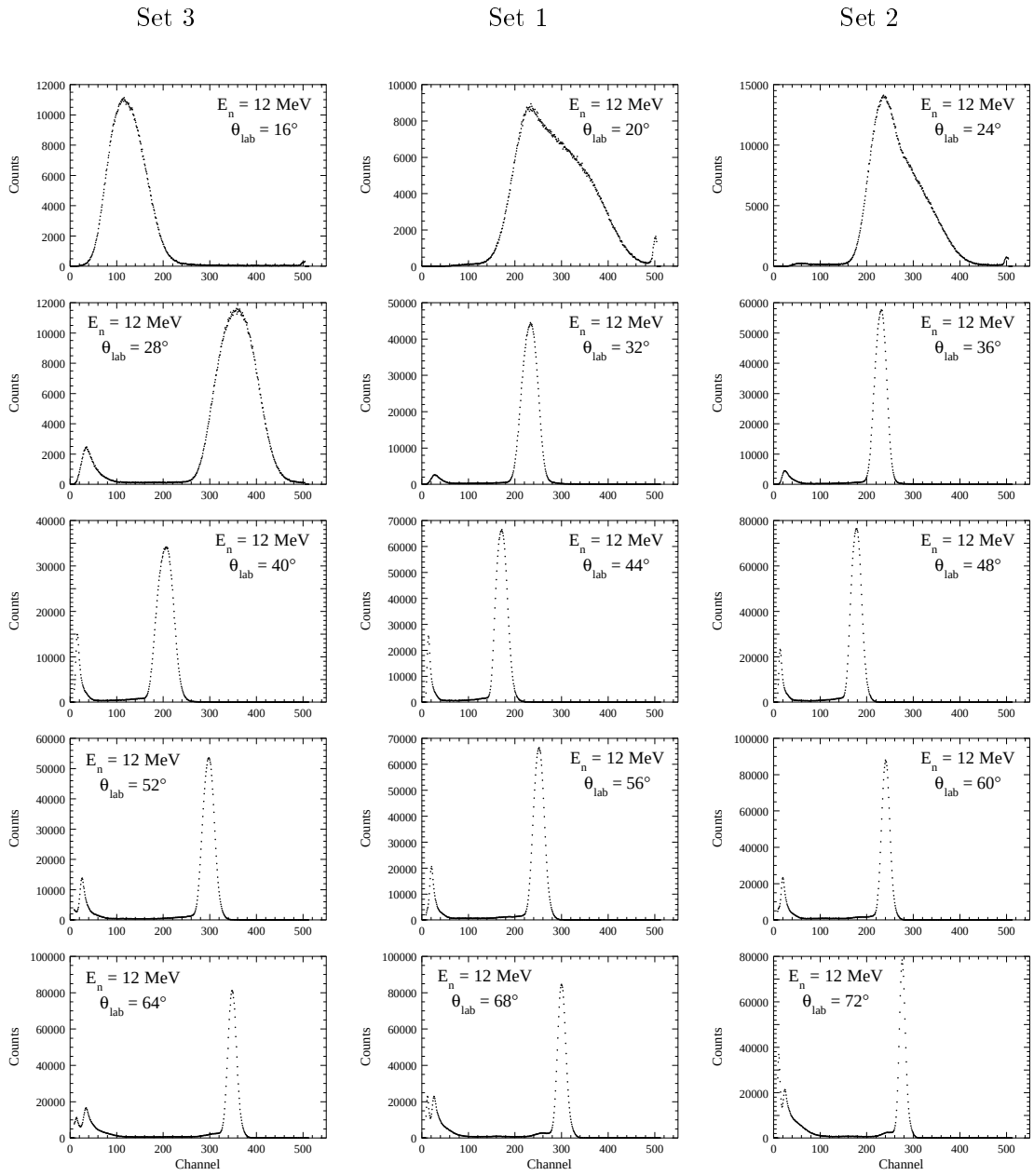

Figure 3.7: Representative center detector pulse-height (CDPH) spectra after sorting at $E_n = 12$ MeV.

			10%		30%		50%	
θ_{lab}	θ_{cm}	Set	A_y	dA_y	A_y	dA_y	A_y	dA_y
16.0	32.1	4	0.00335	0.00060	0.00360	0.00063	0.00369	0.00069
20.0	40.1	5	0.00539	0.00058	0.00490	0.00059	0.00495	0.00065
24.0	48.2	6	0.00380	0.00057	0.00394	0.00060	0.00404	0.00064
28.0	56.2	4	0.00856	0.00059	0.00836	0.00061	0.00815	0.00064
32.0	64.2	5	0.00673	0.00054	0.00671	0.00058	0.00687	0.00060
36.0	72.2	6	0.00759	0.00055	0.00765	0.00056	0.00743	0.00060
40.0	80.2	4	0.00745	0.00053	0.00718	0.00057	0.00696	0.00060
44.0	88.2	5	0.00746	0.00055	0.00746	0.00056	0.00687	0.00060
48.0	96.2	6	0.00284	0.00052	0.00287	0.00055	0.00301	0.00058
52.0	104.2	4	0.00369	0.00054	0.00365	0.00056	0.00358	0.00060
56.0	112.2	5	0.00335	0.00052	0.00308	0.00054	0.00319	0.00057
60.0	120.2	6	0.00259	0.00055	0.00231	0.00058	0.00258	0.00061
64.0	128.2	4	0.00327	0.00052	0.00306	0.00054	0.00304	0.00058
68.0	136.2	5	0.00344	0.00057	0.00301	0.00059	0.00312	0.00064
72.0	144.3	6	0.00087	0.00077	0.00062	0.00081	0.00034	0.00089

Table 3.2: Raw *np* analyzing powers for incident neutron energy of $E_n = 7.6$ MeV.

			10%		30%		50%	
θ_{lab}	θ_{cm}	Set	A_y	dA_y	A_y	dA_y	A_y	dA_y
16.0	32.1	3	0.00693	0.00057	0.00730	0.00061	0.00703	0.00064
20.0	40.1	1	0.01074	0.00056	0.01099	0.00058	0.01108	0.00061
24.0	48.2	2	0.01354	0.00059	0.01350	0.00060	0.01370	0.00066
28.0	56.2	3	0.01346	0.00057	0.01353	0.00058	0.01342	0.00062
32.0	64.2	1	0.01474	0.00053	0.01513	0.00057	0.01513	0.00058
36.0	72.2	2	0.01311	0.00055	0.01344	0.00059	0.01376	0.00061
40.0	80.2	3	0.01672	0.00054	0.01655	0.00055	0.01648	0.00057
44.0	88.2	1	0.01334	0.00051	0.01363	0.00053	0.01366	0.00054
48.0	96.2	2	0.01117	0.00051	0.01139	0.00052	0.01109	0.00056
52.0	104.2	3	0.01296	0.00049	0.01262	0.00050	0.01233	0.00053
56.0	112.2	1	0.00787	0.00048	0.00755	0.00050	0.00746	0.00053
60.0	120.2	2	0.00421	0.00050	0.00435	0.00052	0.00450	0.00056
64.0	128.2	3	0.00381	0.00043	0.00388	0.00047	0.00407	0.00048
68.0	136.2	1	0.00403	0.00051	0.00394	0.00052	0.00369	0.00056
72.0	144.3	2	0.00309	0.00059	0.00312	0.00061	0.00303	0.00066

Table 3.3: Raw *np* analyzing powers for incident neutron energy of $E_n = 12$ MeV.

The error in the analyzing power was then calculated from the errors associated with both the asymmetry and the neutron polarization. This error was

$$\Delta A_y = \sqrt{(A_y)^2 \left[\left(\frac{\Delta\varepsilon}{\varepsilon} \right)^2 + \left(\frac{\Delta p_n}{p_n} \right)^2 \right]}. \tag{3.5}$$

The uncorrected np analyzing powers for all three yields are given in Table 3.2 for $E_n = 7.6$ MeV and in Table 3.3 for $E_n = 12$ MeV. Comparison of the analyzing powers from the different gates shows the variation of the asymmetry due to finite geometry effects. The more inclusive gates allowed for a better statistical sample at the expense of a larger acceptance in the experimental geometry. As was mentioned earlier, the detector arrangement allowed for 5 angles to be measured simultaneously. The third column in Tables. 3.2 and 3.3 denote which angles were measured together. The angles 20°, 32°, 44°, 56° and 68° at $E_n = 12$ MeV were the first set measured, the angles 24°, 36°, 48°, 60° and 72° at $E_n = 7.6$ MeV were the final set to be measured. As can be seen from the data, the analyzing powers measured for each of the three gates were generally fairly close, usually within 10% of each other. At certain angles, larger difference between the three gates were seen, such as $\theta_{\rm lab} = 44°$ at 7.6 MeV and $\theta_{\rm lab} = 36°$ and 52° at 12 MeV where the difference between the gates was larger than expected. However, no systematic effects were seen occurring between detectors of the same sets.

3.2 Variation of np asymmetries

The np data were taken over the period from April 1993 to February 1994 during a series of approximately two-week long runs. Through the use of a dedicated electronics (Sect. 2.6) and a dedicated detector array (Sect. 2.5) the setup time required for each run was minimized; the times presented below reflect the actual amounts of "production" data time required to achieve the necessary statistics. Due to the small magnitude of the np analyzing power, a very accurate measurement was desired. For each angle a measurement with a statistical error of ± 0.0005, as defined by Eqn. 3.5, was set as the goal; this was

achieved for all but the most backward angles. Since the array allowed for the simultaneous measurement of five angles at one time, the time required for each angle set was determined by the statistically "worst" angle, typically the most backward angle in the set. Thus for each set approximately two weeks of beam time was required. During the course of the experiment the deuteron beam polarization was steadily improved, due to increasing expertise in adjusting the source. This helped to shorten the time required for each set of angles.

During each two-week run the data was taken in approximately 40-minute measurements. Each set of angles required approximately 350 of these single measurements to reach the desired statistics. The measurements were grouped into sets each containing between one and two dozen single measurements. After each set all data histograms were zeroed and a new set was begun. This grouping allowed the operators to tune the beam during a measurement and not aversely affect a large data set. When instrumental errors were detected the operator could clear the histograms to the last known good measurement and begin accumulating data again, or begin a new set of measurements, depending on the severity of the error.

Fig. 3.8 shows the accumulated raw data for one set of angles (20°, 32°, 44°, 56° and 68° plus the polarimeter data) at $E_n = 12$ MeV. The crosses show the analyzing power of the "sets" of individual measurements. The solid dots show the average of the previous "sets". These averages usually corresponded with breaks in the run time or mechanical difficulties which interrupted the data taking. Histograms within these averaged sets could usually be compared and summed directly; longer delays in data taking often necessitated powering down detectors and other electronics which caused slight gain changes in the histograms, making it necessary to reset gates.

Despite the scatter in the individual sets (crosses) the averaged sets (filled circles) show little variance from the final average (open box). The error bars shown represent only the statistical error of the measurements. Note also the general upward trend of the neutron

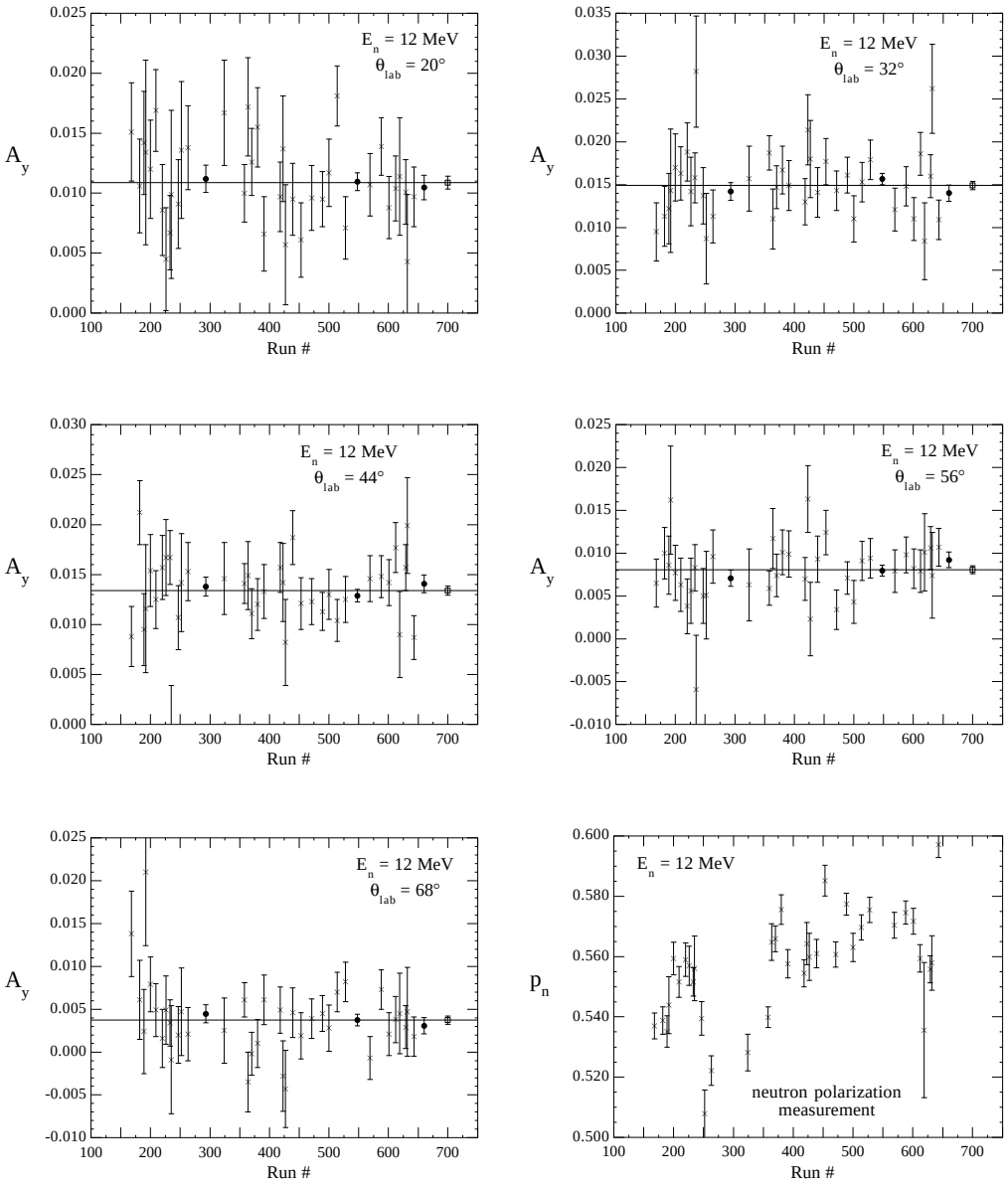

Figure 3.8: Run-by-run stability of *np* analyzing powers measurement. The filled circles are the average analyzing power for the previous measurements and the open box is the final raw analyzing power for the entire set. The bottom right panel gives the run-by-run neutron polarization.

polarization from the n-^{4}He monitor, indicating the improved beam from the source.

3.3 Cross Talk

An additional source of background came from neutrons scattering from a more forward detector and then into another detector. This was most apparent in the backward angle detectors and was due to the close spacing of the detectors. The two most backward detectors of each angle set were effected most by this "cross talk". Neutrons which scattered at a smaller angle (and therefore with a higher energy) could back-scatter from this detector into a higher-angle detector and still be within the TOF window for that detector. As was mentioned in Sec. 2.5.1 this was lessened by choosing shorter flight paths for the more backward detectors; the lower cross section for scattering to the backward angle needed to reach the other detector reduced the amount of background from this process. In addition this solution also helped to equalize the count rates between the detectors. Fig. 3.9 shows the spectrum for $\theta_{\rm lab} = 60^\circ$ superimposed over the spectrum at $\theta_{\rm lab} = 72^\circ$ (both at $E_n = 12$ MeV). The cross-talk events can be seen in the 72° spectrum occurring at the same energy as the 60° peak.

The effect of this process on the analyzing power can be see in Fig. 3.10. This figure shows the analyzing power at 72° where yields were taken over a range of channels, with the lower channel of the gate incremented while the upper channel was held constant. The starting point for the lower channel was the 10% gate used in the analysis. It can be seen that the analyzing power remains fairly constant over the range where the cross-talk effect is apparent, even up to channel 270 where the cross-talk influence is negligible. From this analysis and the cross-checking with the more restrictive gates it was determined that the cross talk produced a negligible effect on the np analyzing powers.

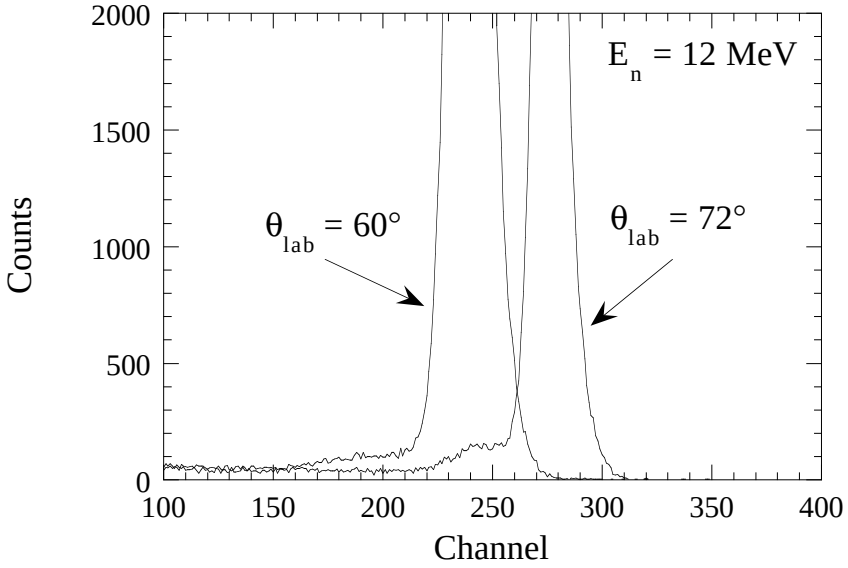

Figure 3.9: Cross talk in the CDPH spectrum at the backward angles. The spectra shown are $\theta_{\rm lab} = 60^\circ$ and 72° at $E_n = 12$ MeV. The cross-talk events can be seen in the 72° spectrum lying underneath the overlayed 60° spectrum.

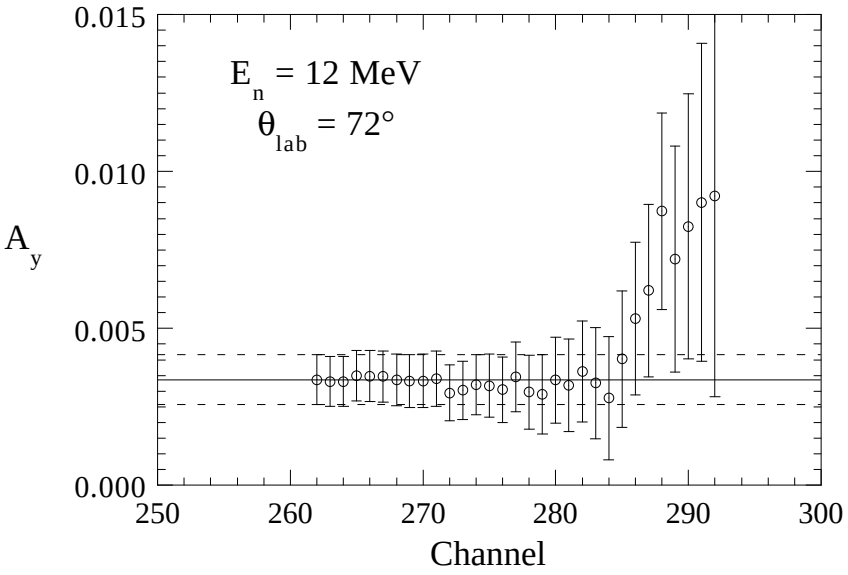

Figure 3.10: Collapsing-channel asymmetry for an np detector at $E_n = 12$ MeV and $\theta_{\rm lab} = 72^\circ$. The upper channel is held constant while the lower channel is incremented to observe the effect of the cross talk on the asymmetry.

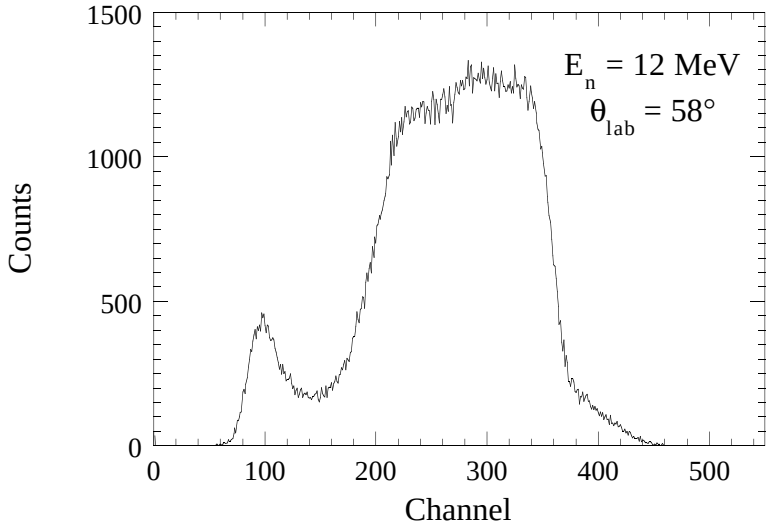

Figure 3.11: Neutron polarimeter center detector pulse-height spectrum. The signal was the sum of the light outputs of the top and bottom phototubes. Spectrum shown is for $E_n = 12$ MeV and $\theta_{\rm lab} = 58^\circ$ and contains both spin states.

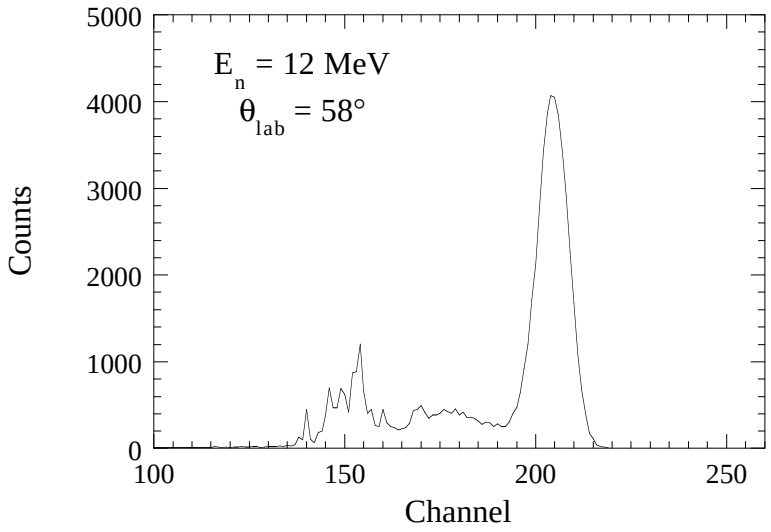

Figure 3.12: Neutron polarimeter TOF spectrum. Spectrum shown is for the right-side detector at $E_n = 12$ MeV and $\theta_{\rm lab} = 58^\circ$ and contains only spin-up events.

E_n(MeV)	$\theta_{\rm lab}$	$p_n \pm dp_n$	$\theta_{\rm lab}[n\text{-}^4\text{He}]$	$A_y(\theta)[n\text{-}^4\text{He}]$
7.6	16°, 28°, 40°, 52°, 64°	0.556 ± 0.008	54°	-0.615 ± 0.009
	20°, 32°, 44°, 56°, 68°	0.562 ± 0.008		
	24°, 36°, 48°, 60°, 72°	0.675 ± 0.010		
12	16°, 28°, 40°, 52°, 64°	0.585 ± 0.009	58°	-0.554 ± 0.008
	20°, 32°, 44°, 56°, 68°	0.558 ± 0.008		
	24°, 36°, 48°, 60°, 72°	0.545 ± 0.008		

Table 3.4: Average neutron polarization for all angle sets. The analyzing powers for the $^4\text{He}(\vec{n}, n)^4\text{He}$ reaction are corrected for finite-geometry effects.

3.4 Neutron Polarization

The neutron polarimeter data were sorted similar to the *np* data, but were taken with separate ADC's on a separate MBD channel in order to minimize the dead time of the *np* experiment. Due to limitations of the XSYS software, the neutron polarization data was not stored in event mode, but this was deemed unnecessary due to the thorough sorting done online. For each event the following signals were stored: the center detector pulse height (CDHE) in the ^{4}He gas cell and the time-of-flight (TOF) between each neutron side detector and the ^{4}He gas cell. The TOF signals of the left and right polarimeter detectors were summed into a single Northern ADC which had been modified [Rob81b] to allow additional bits to be added on top of the digitized signal and sent to the computer for sorting. These bits were used to provide left/right detector routing as well as spin-sense information. A second Northern was used to digitize the CDHE signal.

Pulse-shape discrimination was performed in hardware only; the resolution of the neutron detectors, which were of the same design as those in the *np* experiment, was deemed sufficient for the polarization measurement. Here a single-channel discriminator on the PSD TAC was used to cut the spectrum in the valley between the γ-ray events and the neutron events (as an example see lower channel in Fig. 3.1).

The center detector pulse height, which was the summed signal of the top and bottom phototubes, was sorted into a spectrum. An example of this is shown in Fig. 3.11.

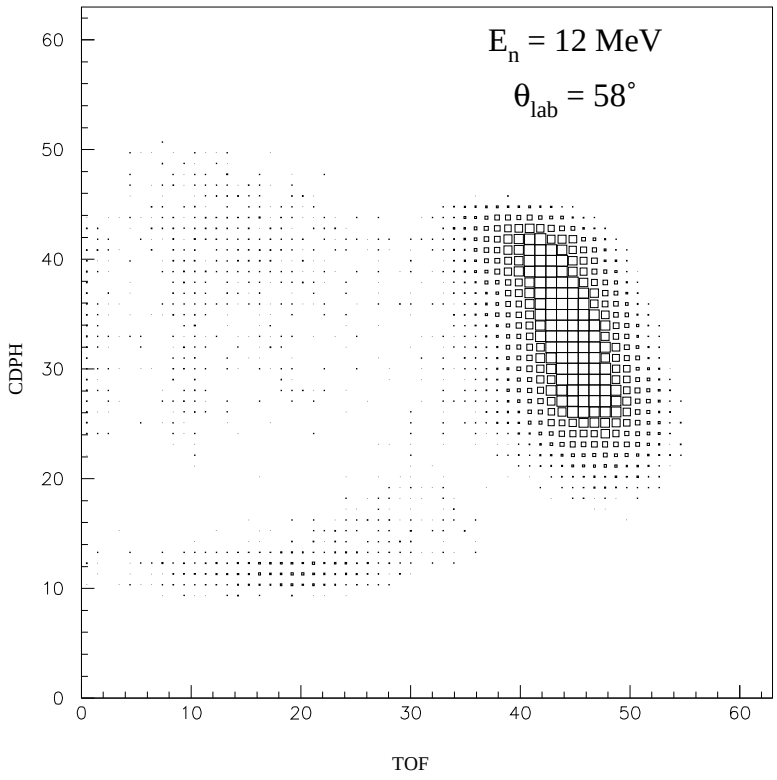

Figure 3.13: Neutron polarimeter spectrum showing TOF plotted versus CDPH. Spectrum shown is for right-side detector TOF at $E_n = 12$ MeV and $\theta_{\rm lab} = 58^\circ$ and contains only spin-up events.

The spin states were not separated in this raw spectrum. The side-detector TOF events were sorted into separate spectra for each detector and spin state; a sample spectrum for the right detector in the spin "up" state is shown in Fig. 3.12. As with the *np* data, a 60-channel cut centered on the elastic TOF peak was made and events passing this cut were incremented into a two-dimensional spectrum versus the compressed ^{4}He recoil pulse-height spectrum (see Fig. 3.13). The separation of the neutron polarimeter elastic events was such that projection onto the helium recoil pulse-height axis was actually unnecessary. However, in order to be consistent with the analysis of the *np* data, the projection was performed. Since the elastic peak was completely separated from the breakup and other

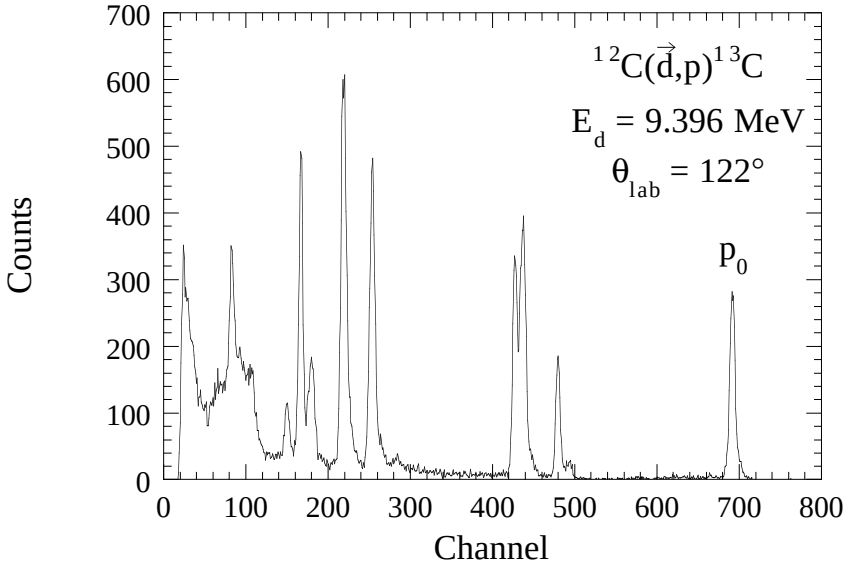

Figure 3.14: Deuteron polarimeter spectrum showing energy deposited in the solid-state detector. The peak at channel 700 was used to tune the deuteron vector polarization.

background events, a two-dimensional gate was chosen to select out only the elastic events. Yields were then taken from the full-resolution recoil spectrum to determine the scattering asymmetry of the neutrons, and by inverting Eqn. 1.82, the incident neutron polarization was determined. Table 3.4 shows the total average neutron polarization for all sets of angles at both energies. This table also shows the finite-geometry corrected analyzing power for the ^{4}He$(\vec{n},n)^4$He reaction used to determine the neutron polarization. The finite-geometry corrections were determined via a Monte-Carlo simulation of the polarimeter setup [Tor94]. This simulation calculated the n-^{4}He analyzing powers from the phase shifts of Stammbach and Walter [Sta72]; the errors shown for the analyzing powers reflect the uncertainty in the phase-shifts of about 1.5%.

3.5 Deuteron Polarization

The deuteron polarimeter events were sorted on a MBD channel separate from both the np and neutron polarimeter events. The deuteron polarimeter was not typically

run during the *np* experiment, but only used to initially tune the transition units on the polarized ion source. With only two detectors in the setup, the measurement did not provide information about the tensor component of the deuteron beam. For this reason, when the charged-particle detector asymmetry was tuned to a maximum, a measurement of the transfered neutron polarization was made. When it was determined that a sufficient neutron polarization was reached, the carbon foil was typically removed from the beam axis and the deuteron computer interface electronics were disabled.

Fig. 3.14 shows a typical energy spectrum for the deuteron polarimeter; this particular spectrum is for the spin-up ($p_d = 1$) case. The well-separated peak near channel 700 is the peak for the $^{12}\mathrm{C}(\vec{\mathrm{d}}, \mathrm{p}_0)^{13}\mathrm{C}$ reaction.

Chapter 4

Offline Analysis

Due to the small size of the *np* analyzing power, it was essential that as much of the residual background be accounted for as possible. Therefore the analysis of the data centered mainly on an accurate simulation of the experiment using the Monte-Carlo method. As a starting point, the computer code from Weisel's analysis [Wei92] was used; however during the course of the analysis, extensive modifications and additions were made to the original code. This code simulated the finite-geometry effects of the experiment as well as the different scattering processes which contributed to the observed yields. The relative contribution of these processes to the total yield in the detectors could then be used to infer the true yield from elastic *np* scattering.

4.1 Monte-Carlo Method

In the simulation, one wants to be able to model the different scattering processes and geometric effects, since experimentally there is no practical way to subtract these from the data. To do this one needs to be able to calculate the total number of neutrons detected in the side detectors. This can be done by calculating the flux of neutrons at each scattering point and using this to determine the flux at subsequent interaction points, ending up with the detection in the side detector. The flux of neutrons through the volume element, dV_{n+1},

after n scattering processes, is then

$$d^n\Phi_n = \Phi_0 \prod_{i=1}^{n} \frac{\bar{n}_i}{r_i^2} \frac{d\sigma_i}{d\Omega} A_i \, dV_i, \tag{4.1}$$

where Φ_0 is the incident deuteron flux from the $^2\mathrm{H}(\vec{d},\vec{n})^3\mathrm{He}$ polarization-transfer reaction, $\bar{n}_i$ is the particle density of the nuclei scattered from at scattering point i (in our notation "scattering" includes also the reaction in the gas cell), r_i is the distance from scattering point $i-1$ to i, and A_i is the attenuation of the neutron beam due to interactions with the matter it passes through between the reaction points. From the flux, one can then determine the number of neutrons detected in the $n+1$ process. This is given by

$$d^{n+1}N_n = d^n\Phi_n \, \eta \, dV_{n+1} \tag{4.2}$$

where $d^n\Phi_n$ is the flux from Eqn. 4.1, η is the response sensitivity for the $n+1$ scattering process and dV_{n+1} is the volume element. The total number of neutrons can then be found by integrating over all the volumes of the individual scattering processes. This multi-dimensional integral is

$$\begin{aligned} N_{neutrons} &= \int_{V_1} \cdots \int_{V_n} \int_{V_{n+1}} d^n\Phi_n \, \eta \, dV_{n+1} \\ &= \int_{V_1} \cdots \int_{V_n} \int_{V_{n+1}} I \, dV_1 \cdots dV_{n+1}. \end{aligned} \tag{4.3}$$

This integral can be integrated by the Monte-Carlo method if one evaluates the integrand, I, at N different statistically-chosen positions. If l represent an arbitrary position within the multi-dimensional space of the integral, the number of neutrons is given approximately by

$$N_{neutrons} \approx V_1 \cdots V_n V_{n+1} \left[\frac{1}{N} \sum_{l=1}^{N} I_l \right]. \tag{4.4}$$

Each arbitrary position, l, is described by a set of geometrical and kinematic variables, including the position of each of the scattering points (which determined the particle trajectories and reaction angles) and the particle energies (which determined the light output and neutron time-of-flight). At each position, checks of these parameters are made in order

to determine whether that event would pass the detection criteria of the experimental setup. Events which were excluded by these had their weighting factor, I_l, set to zero. After calculating the number of detected neutrons in each detector, the asymmetry of the simulated events could be determined and used to correct the experimentally determined value.

For the present experiment the $n+1$ scattering process represents the final detection of the neutron within the volume of one of the neutron side detectors. A single-scattering process in the scatterer would then include a reaction point in the deuterium gas cell and one reaction point in the scatterer, so $n = 2$; the final detection in the side detector would be the third scattering process. A double-scattering process in the scatterer would include an additional reaction point in the scatter with $n = 3$, so the final detection would be the fourth scattering process.

To make the calculations manageable, some simplifications were made to the simulated experimental setup. Only a single neutron spin state was taken into account for each detector. Since in the actual experiment, flipping the spin state made it possible to cancel certain physical and geometrical differences in the detectors, the two simulated neutron detectors were made identical, *i.e.*, the size and position (and thus the solid angle) of both detectors were made equal, as well as the neutron detection efficiencies and detection threshold energies. In addition scattering to both the left and right detectors was forced for each event, in order to increase the statistics of the calculation.

4.2 Scattering Processes

Due to the large amounts of carbon as well as hydrogen in the scatterer and the detectors, the experimental spectra contained events from other scattering processes in addition to the elastic *np* scattering of primary interest. The Monte-Carlo simulation considered the following neutron-scattering processes (in the code the different processes were assigned different values of the variable, `NPATH`, which could used to select the scattering processes to be calculated):

P0	P1	P3	P4
deuterium gas cell	scatterer	left detector	right detector
R0 = 0.238 cm	R1 = 0.950 cm	AL = 2.13 cm	AR = 2.13 cm
GL0 = 1.580 cm	H1 = 1.905 cm	BL = 3.76 cm	BR = 3.76 cm
		CL = 5.93 cm	CR = 5.93 cm
D1 = 172.4 cm		D2*	D3*

Table 4.1: Geometry of the detectors in the *np* experiment. The variables shown refer the variable names used in the Monte-Carlo code. The dimensions given are half-lengths; *i.e.*, the total length of the deuterium gas cell is $2 \times$ GL0. For the left-side neutron detector, $2 \times$ AL is the width, $2 \times$ BL is the thickness and $2 \times$ CL is the height. D1 is the distance between the neutron production gas cell and the scatterer. D2 and D3 are the flight paths to the left and right detectors, respectively (* see Tables 2.2 and 2.3).

- single scattering from hydrogen (NPATH=1)
- double scattering from hydrogen (NPATH=2)
- double scattering first from hydrogen then from carbon (NPATH=31)
- double scattering first from carbon then from hydrogen (NPATH=32)
- single scattering from hydrogen in the scatterer and double scattering in the side detector, first from carbon then from hydrogen

As mentioned in Sec. 4.1 all events included a reaction in the deuterium gas cell where the neutron beam was produced and a reaction in the side detectors where the neutron was finally detected. The processes listed above, with the exception of the final one, consider the scattering processes taking place within the center scatterer. The final process is a multiple-scattering process in the side detectors and will be discussed in more detail in Section 4.6. Only single and double-scattering processes were considered; triple scattering processes were not simulated. The simulated yield due to all double scattering processes amounted to roughly 1.5% of the total single scattering yield, thus a triple scattering process was assumed to have a similar relation to the double scattering, making it a negligible effect.

At each energy and angle measured experimentally, the simulation was run with the different scattering processes "turned on" in order to determine their contribution to the total scattering. The sum of these scattering processes would then simulate the ex-

perimentally observed data. For each simulated scattering process, the code calculated the following:

- the number of neutrons detected in each side detector, the calculated asymmetry and the statistical error
- the proton light-output spectra of the center detector in coincidence with each side detector
- the time-of-flight spectra for each side detector from the center scatterer

These could then be compared to the experimental data; in particular the light-output spectra were saved to a file which could be loaded into the data analysis software and compared directly to the experimental light output. These simulated spectra were matched closely to the experimental spectra, to reproduce the relative gain and shape of the spectra. These were matched using the single-scattering simulations and then held constant during the calculation of the subsequent multiple-scattering processes.

The following sections describe the different routines of the simulation, including the target routine, the kinematic calculations, the weighting of the event and finally the calculation of asymmetry and associated error for each process.

4.3 Target Routine

For each event, a particle trajectory was traced out from an incident deuteron beam, to a reaction point (`P0`) in the deuterium gas cell, to one or two scattering points (`P1` and `P2`) within the scatterer and finally to a point in each of the two side detectors (`P3` in the left detector, `P4` in the right). The coordinate systems were chosen in the gas cell, the scatterer and the two side detectors as shown in Fig. 4.1, with the origin at the center-of-gravity for each object. The geometry of the simulation was modeled to correspond to the actual experimental setup. The various geometrical parameters of the simulation are given in Table 4.1 while the flight paths from the scatterer to the side detectors can be found in Tables 2.2 and 2.3. For each event, scattering to both the left and right was considered in order to increase the statistics of the calculation.

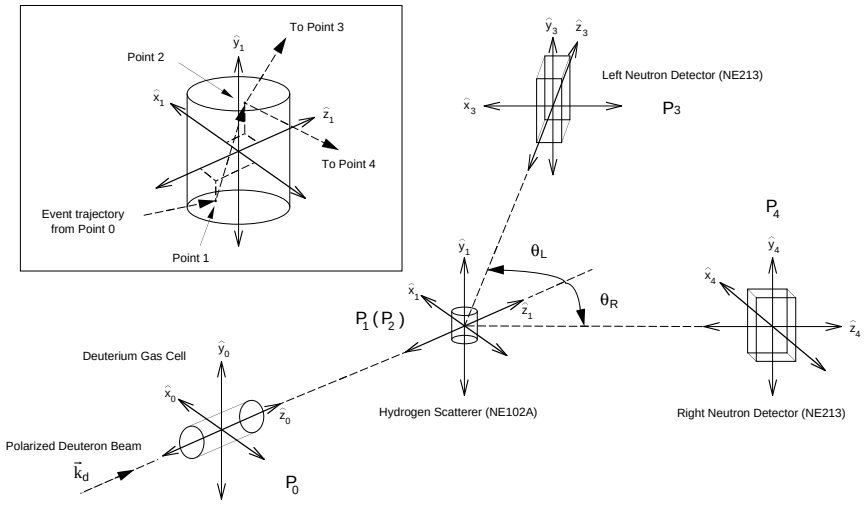

Figure 4.1: Monte-Carlo geometry showing coordinates for each reaction point in a simulated event. The inset shows the geometry of a typical multiple-scattering process within the scatterer.

Each reaction point of an event was chosen randomly. A random number generator, ran(0,1), was used to provide a distribution of numbers evenly distributed over the range (0,1). This distribution was then used to pick the coordinates of the reaction point. For the deuterium gas cell (point `P0`), a point was chosen (in the coordinate frame of the gas cell) as follows:

$$\begin{aligned} x_0 &= 2 \cdot \texttt{R0} \cdot \mathrm{ran}(0,1) - \texttt{R0} \\ y_0 &= 2 \cdot \texttt{R0} \cdot \mathrm{ran}(0,1) - \texttt{R0} \\ z_0 &= 2 \cdot \texttt{GL0} \cdot \mathrm{ran}(0,1) - \texttt{GL0}. \end{aligned} \tag{4.5}$$

Here `R0` and `GL0` are the gas cell radius and half-length, respectively, as given in Table 4.1. This point was checked to determine if it lay inside the volume of the gas cell by checking the inequality

$$x_0^2 + y_0^2 \leq \texttt{R0}^2. \tag{4.6}$$

If this condition was not met, a new point was chosen. For a valid point, a transformation into the coordinate system of the scatterer was then performed

$$x_{01} = x_0$$

$$\begin{aligned} y_{01} &= y_0 \\ z_{01} &= z_0 - \texttt{D1} \end{aligned} \tag{4.7}$$

where D1 is the distance between the deuterium gas cell and the scatterer.

Next a reaction point in the scatterer, P1, was chosen in a manner similar to the first point:

$$\begin{aligned} x_1 &= 2 \cdot \texttt{R1} \cdot \mathrm{ran}(0,1) - \texttt{R1} \\ y_1 &= 2 \cdot \texttt{H1} \cdot \mathrm{ran}(0,1) - \texttt{H1} \\ z_1 &= 2 \cdot \texttt{R1} \cdot \mathrm{ran}(0,1) - \texttt{R1} \end{aligned} \tag{4.8}$$

where R1 is the radius of the scatterer and H1 is the half-height (from Table 4.1). This point was also checked to determine that it lay within the scatterer (as in Eqn. 4.6). The directional cosines, which define the unit vector, $k_1(x, y, z)$, from P0 to P1 could then be calculated

$$\begin{aligned} l_1 &= (z_1 - z_{01})/r_1 \\ m_1 &= (x_1 - x_{01})/r_1 \\ n_1 &= (y_1 - y_{01})/r_1 \end{aligned} \tag{4.9}$$

where r_1 is the distance between points P0 and P1. Since the incident deuteron beam was assumed to be uniform and parallel to the incoming beam axis, the unit vector of the beam at the gas cell reaction point was $k_d(x, y, z) = k_0(x, y, z) = (0, 0, 1)$. The reaction angle, θ_1, from point P0 to P1 is then defined by

$$\cos\theta_1 = k_0 \cdot k_1 = l_1. \tag{4.10}$$

In the case of multiple scattering within the scatterer, a second point (P2) was chosen randomly in the scatterer. However, to prevent a large weighting of points chosen close together (due to the $\frac{1}{r^2}$ dependence of the weighting, see Eqn. 4.1), the second point was discarded and rechosen if it was within $\frac{1}{10} \times$ R1 (the radius of the scatterer) of the first point. For a valid point P2 the unit vector, k_2, and the scattering angle between points P1 and P2, θ_2 was then calculated.

Next reaction points P3 and P4 were chosen in the left and right side detectors, respectively. Again, the points were chosen randomly within the detector volumes. The procedure was identical for the left and right detectors. For the left side detector the reaction point was

$$\begin{aligned} x_3 &= 2 \cdot \mathtt{AL} \cdot \mathrm{ran}(0,1) - \mathtt{AL} \\ y_3 &= 2 \cdot \mathtt{CL} \cdot \mathrm{ran}(0,1) - \mathtt{CL} \\ z_3 &= 2 \cdot \mathtt{BL} \cdot \mathrm{ran}(0,1) - \mathtt{BL} \end{aligned} \tag{4.11}$$

where AL, BL, and CL are the half-dimensions of the detector given in Table 4.1. This point is then transformed into the coordinate system of the scatterer as follows:

$$\begin{aligned} x_{13} &= \mathtt{D2} \cdot \cos\theta_L \pm \sqrt{x_3^2 + z_3^2}\ \cos\left(\theta_L + \arctan(\frac{x_3}{z_3})\right) \\ y_{13} &= y_3 \\ z_{13} &= \mathtt{D2} \cdot \cos\theta_L \pm \sqrt{x_3^2 + z_3^2}\ \sin\left(\theta_L + \arctan(\frac{x_3}{z_3})\right) \end{aligned} \tag{4.12}$$

where D2 is the flight path between the scatterer and the left side detector. The second term in x_{13} and z_{13} of Eqn. 4.12 is positive for the case where $z_3 > 0$ (in the reference frame of the side detector) and negative otherwise. The components of the unit vector, k_3, from P1 to P3 were then determined. For the case of single-scattering in the scatterer this is:

$$\begin{aligned} l_3 &= (z_3 - z_{13})/r_3 \\ m_3 &= (x_3 - x_{13})/r_3 \\ n_3 &= (y_3 - y_{13})/r_3 \end{aligned} \tag{4.13}$$

where r_3 is the distance between points P1 and P3. The reaction angle from the scatterer to the left side detector, θ_3 is then defined by

$$\cos\theta_3 = k_1 \cdot k_3 = l_1 l_3 + m_1 m_3 + n_1 n_3. \tag{4.14}$$

In the case of double scattering in the scatterer, point P2 was substituted for P1 in Eqn. 4.13 and the unit vector, k_2, was substituted in Eqn. 4.14. With all reaction points determined and the scattering angles between the points calculated, the kinematics for the event could then be determined.

4.4 Kinematic Calculations

The first reaction point, `P0`, the neutron production via the ^{2}H$(\vec{d},\vec{n})^3$He polarization transfer reaction in the deuterium gas cell, was common to all scattering processes. The incoming deuteron beam was considered monoenergetic and parallel to the beam axis, as mentioned before. The deuteron energy loss in both the 0.25 mil Havar foil at the gas cell entrance and in the deuterium gas up to the reaction point, `P0`, was calculated. The resulting deuteron energy was then used to calculate the associated incident neutron energy, E_n^0, and to determine the cross section for the ^{2}H$(\vec{d},\vec{n})^3$He polarization-transfer reaction from a library [Lis73].

The code also had the option to pick E_n^0 randomly from a distribution centered on the average beam energy and having a variance equal to the energy spread due to the deuteron energy loss in the gas cell. The energy loss was calculated for different deuterium gas pressures by the TUNL code `BABEL` [Bow82]. Of course, this is only valid if the ^{2}H$(\vec{d},\vec{n})^3$He cross section does not change appreciably within the range of possible deuteron energies and if E_n^0 (for a given deuteron energy) does not change over the face of the scatterer. In this case the neutron energy incident at point `P1` was then chosen as

$$E_n^0 = \overline{E}_n + 2\delta_{E_n}\,\mathrm{ran}(0,1) - \delta_{E_n}\,, \tag{4.15}$$

where $\overline{E}_n$ is the average beam energy for the experiment and δ_{E_n} was the energy spread as calculated from Ref. [Bow82]. Breakup neutrons from the ^{2}H(d,n)np reaction were not modeled in this simulation because their energies are considerably lower than the energies of interest.

Given the incident neutron energy and the scattering angle calculated in the target routine (Sec. 4.3), the energy of the scattered neutron was calculated. For the single-scattering case, the energy of the scattered neutron to the left-side detector was

$$E_n^1 = E_n^0 \left(\frac{m_n}{m_n+m_p}\right)^2 \left\{\cos\theta_3 + \left[\left(\frac{m_p}{m_n}\right)^2 - 1 + \cos^2\theta_3\right]^{\frac{1}{2}}\right\}^2 \tag{4.16}$$

and the recoil energy of the scattered proton

$$E_p = E_n^0 - E_n^1. \tag{4.17}$$

For the multiple-scattering case, the neutron energy and associated proton recoil energy was calculated at each scattering point.

The detectors used in the experiment measured the light output of the recoil protons, so for these scattering processes, the light output was determined. The light output in the center detector, L, was taken to be proportional to the proton energy. The light response function was determined empirically by matching the simulated proton recoil energy spectra to the experimental light spectra for each side-detector angle measured. Figs. 3.6 and 3.7 show light spectra fitted for the simulation.

With the energy of the scattered neutrons known, the time-of-flight (TOF) between scattering points was calculated. For `NPATH` = 1 (single-scattering from hydrogen) the TOF between the scattering point in the scatterer and the left-side detector was calculated to be

$$\mathrm{TOF} = F\left(\frac{r_3}{\sqrt{E_n^1}}\right) \tag{4.18}$$

where the TOF is calculated in nanoseconds. The factor, F, is the proportionality constant:

$$F = \sqrt{\frac{1.00898(\mathrm{amu}) \cdot 1.66054 \times 10^{-27}(\frac{\mathrm{kg}}{\mathrm{amu}})}{2 \cdot 1.6021 \times 10^{-19}(\frac{\mathrm{J}}{\mathrm{MeV}})}}. \tag{4.19}$$

For multiple-scattering processes `NPATH` = 2 and 31, an additional time-of-flight between points `P1` and `P2` was also calculated and added to the total. This was not done in the case of `NPATH` = 32 since the initial scattering from carbon did not produce enough light in the center detector to produce a start signal for the TOF.

The TOF, the proton-recoil energy and the proton-recoil light output were then "smeared" to simulate the time and energy resolution seen in the experimental data. To do this several parameters modeling the resolution of the detectors in the experiment were applied to the calculated values. The magnitude of the smearing for an individual event

was picked from a distribution of random numbers; this distribution was formed by taking the sum of 6 random distributions of numbers over the range (0,1)

$$\texttt{GRAND} = \sum_{i=1}^{6} \mathrm{ran}(0,1). \tag{4.20}$$

This number was used for all smearing during the same event; it was recalculated at the beginning of the next event. The "smeared" time-of-flight, TOF$'$, was given by

$$\mathrm{TOF}' = \mathrm{TOF} + \sqrt{2}\ (\texttt{GRAND} - 3)\ \delta_{TOF}, \tag{4.21}$$

where the parameter, δ_{TOF}, was empirically chosen by matching the simulated single-scattering TOF spectrum to the experimental TOF. A "smeared proton recoil energy, E_p', was calculated from the calculated energy

$$E_p' = E_p + \sqrt{2}\ (\texttt{GRAND} - 3)\frac{\delta_{E_p}}{\sqrt{E_p}}, \tag{4.22}$$

where δ_{E_p} was also determined empirically. For the the proton light output, a more complex smearing method was used. The formula used

$$L' = L + (\texttt{GRAND} - 3)\left[\sqrt{2E_p}\ \delta_L + \delta_{T1}(1+L^2)\ e^{\{(\texttt{GRAND}-3)\delta_{T2}(1+L)\}}\right], \tag{4.23}$$

where δ_L determines the width of the proton light distribution while the parameters, δ_{T1} and δ_{T2} generate a tail on the light spectrum. Again all parameters were determined by fitting the single-scattering light output to the experimental light spectra for each energy and angle simulated (see Figs. 3.6 and 3.7).

4.5 Weighting Factors

Once the kinematics of the event were determined, cuts were made corresponding to the detection thresholds and the spectra gates in the data-sorting software (see Sec. 3.1). Events which failed to pass any one of these cuts were discarded; the weighting for the event was set to zero (corresponding to $I_l \rightarrow 0$ in Eqn. 4.4 from Sec. 4.1) and the simulation jumped to the end of the loop to start a new event.

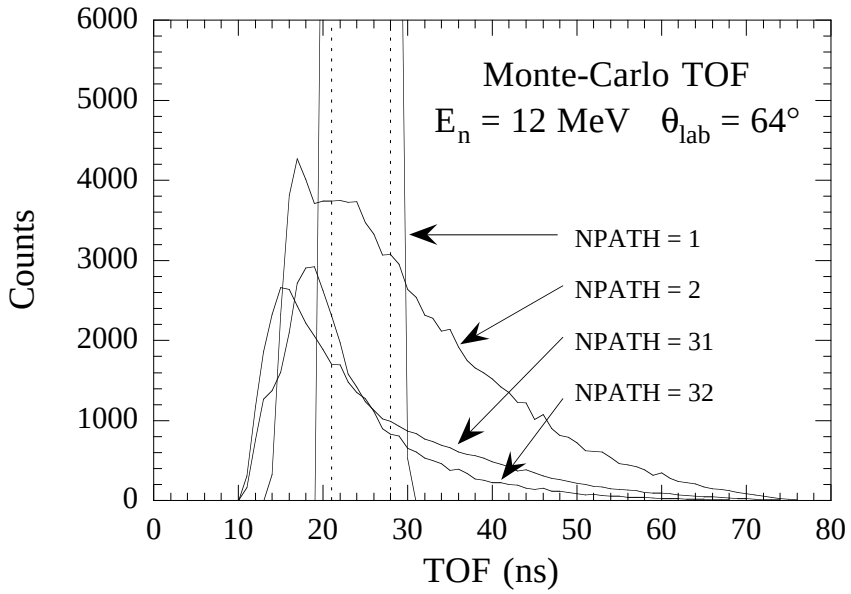

Figure 4.2: Monte-Carlo TOF spectrum at $E_n = 12$ MeV and $\theta_{\rm lab} = 64°$. The dashed vertical lines indicate the TOF cut used for all scattering processes.

For the TOF, a cut was made similar to the cut made on the data shown in Fig. 3.3. This cut was made at approximately 10% of the peak height in the `NPATH` = 1 (single-scattering from hydrogen) TOF peak and was used for all multiple-scattering processes. Simulated events with TOFs lying outside this window were discarded. This cut was set in a 1D TOF spectrum (as opposed to the 2D spectrum used for the data) since the simulated spectrum did not contain background from breakup neutrons. The TOF spectra from the Monte-Carlo simulation at $E_n = 12$ MeV and $\theta_{\rm lab} = 64°$ from the different scattering processes is shown in Fig. 4.2. Here the dashed vertical lines indicate the TOF cut used in the simulation.

Events passing the TOF cut were then checked to determine if their proton recoil energy was above the lower-level bias in the center detector. This threshold was constant for all energies and angles; a threshold energy of 0.2 MeV was used. Finally the scattered neutron energy was checked to determine if it was above the threshold set in the side detectors (see Tables 2.2 and 2.3).

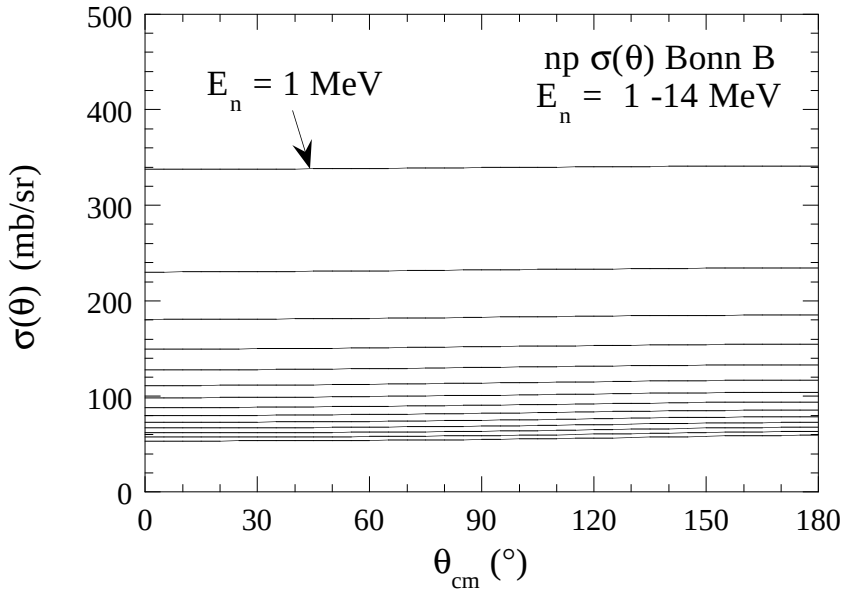

Figure 4.3: Cross-section library for *np* scattering as calculated from Bonn B. Library values are calculated from 1–14 MeV in 1 MeV steps. Phase shifts from Bonn B were used as input to SAID.

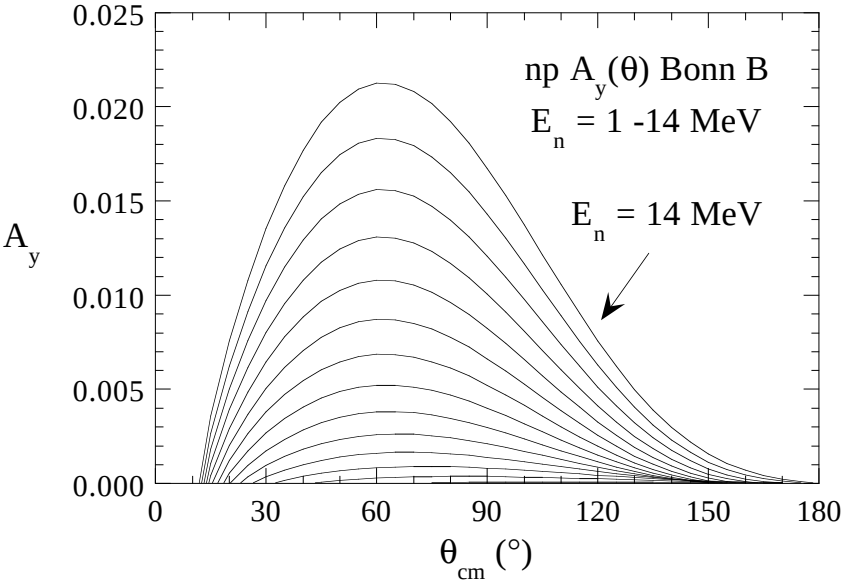

Figure 4.4: Analyzing power library for *np* scattering as calculated from Bonn B. Library values are calculated from 1–14 MeV in 1 MeV steps. Phase shifts from Bonn B were used as input to SAID.

For events passing each of these cuts, the neutron flux at the reaction point was then calculated as in Eqn. 4.1. This required that the polarized cross section for the process be determined. Depending on the scattering process being considered, the appropriate values for the unpolarized cross section and analyzing power were determined from a set of libraries for both np and n-^{12}C scattering. For the np scattering processes the differential cross sections and analyzing powers libraries were determined from phase shifts provided by Machleidt [Mac92] using the Bonn B NN potential model. These phase shifts were used as the input to Arndt's SAID (Scattering Analysis Interactive Dial-in) code [Arn92] in order to calculate the observables. The libraries were calculated for energies from 1–14 MeV in 1 MeV steps, and at each energy the angular distribution was calculated from 0–180° (in the center of mass) in 5° steps. Figs. 4.3 and 4.4 show these libraries for the cross section and analyzing power, respectively. For n-^{12}C scattering, two sets of libraries for the differential cross section and analyzing power were used. The first library covered the energy range from 0.1–8.9 MeV in 2.5° steps and was from a phase-shift analysis performed by Tornow [Tor90]. The second, and more recent, library came from a phase-shift analysis performed by Chen [Che94] and covered the range of energies from 8.97–12.96 MeV in 1° steps. Values for events between the points of all libraries were linearly interpolated. Cross sections returned from the libraries were in center-of-mass coordinates. For the case of single scattering from hydrogen, the polarized cross section (in the laboratory system) had the form

$$\sigma^{lab}(\theta) = U\sigma_0^{cm}(\theta)\ [1 + \vec{p}\cdot\hat{n}\ A_y(\theta)], \tag{4.24}$$

where U is a kinematic factor converting from the c-m system to the laboratory system, σ_0^{cm} is the unpolarized cross section in the c-m system, $\vec{p}$ is the incident neutron polarization (in the $\hat{y}$ direction) and $\hat{n}$ is the scattering normal. At each scattering point, this process would be repeated and the cross section recalculated.

In addition to the polarized cross section, several other factors determined the neutron flux at a scattering point. These included the neutron attenuation between scattering points, the influence of edge effects in the scatterer, the neutron depolarization after scat-

tering from protons and the neutron detector efficiency. Each of these effects is described in the following sections.

4.5.1 Attenuation

The attenuation of the neutron beam due to hydrogen and carbon in the scatterer (NE102A) and the side detectors (NE213) was modeled in the simulation. In the scatterer, the intersection point of the incident neutron flight path with the wall of the scatterer was calculated from kinematics. The distance from this point to the reaction point, `P1`, (given by r_1 in Eqn. 4.25) was then used to determine the attenuation

$$\text{Attenuation} = e^{-(\sigma_p \bar{n}_p + \sigma_c \bar{n}_c) r_1}. \tag{4.25}$$

Here $\bar{n}_p$ and $\bar{n}_c$ are the particle densities of hydrogen and carbon, respectively, in the scatterer. The total np cross section, σ_p and the total n-^{12}C cross section, σ_c, were determined from a table of total cross sections from 0 to 17 MeV [Ste64]. Results for energies between the data points in both tables were linearly interpolated.

Additionally, for multiple-scattering events, the attenuation between the scattering points `P1` and `P2` was determined. Then the attenuation of the neutrons leaving the scatterer, and entering the side detectors was also determined. Air attenuation between the deuterium gas cell and the scatterer and between the scatterer and the side detectors was not taken into account.

4.5.2 Edge Effects

Due to the small size of the scatterer and the energy of the incident beam (and the associated proton recoil energies) a correction for edge effects was included in the calculation. Edge effects occurred when a proton left the scatterer before depositing all of its energy. The range of recoil protons in the scatterer was as much as $\Lambda \sim 0.07(0.16)$ cm at 7.6 (12) MeV, not insignificant given the small size of the scatterer. The edge effects in the side

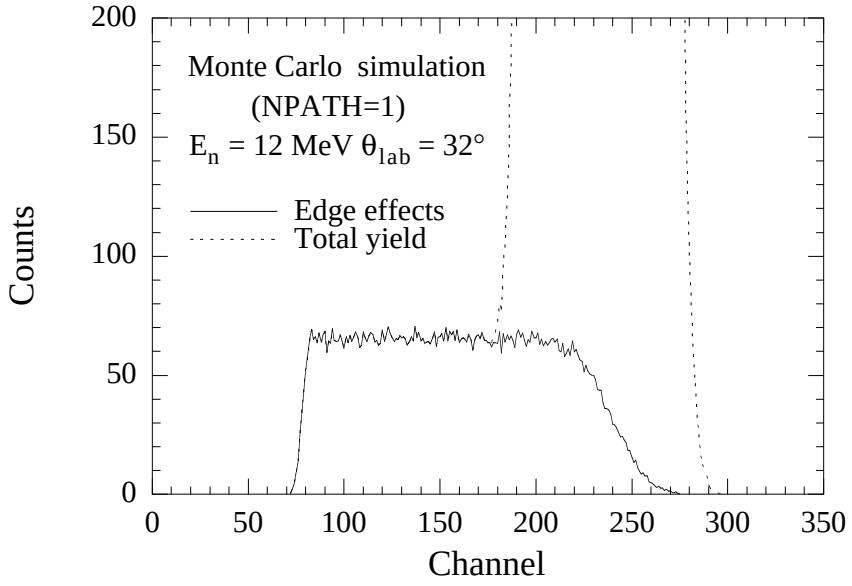

Figure 4.5: Proton-recoil spectrum showing edge effects at $E_n = 12$ MeV and $\theta_{\rm lab} = 32°$. The dotted curve is the spectrum for the total yield for single scattering from hydrogen (`NPATH` = 1) while the solid curve shows edge effects only.

detectors were not considered, due to the much larger volume of these compared to the range of the recoil protons. For each event the scattering point `P1` (or `P2` for multiple scattering if the point was a np interaction) was checked to determine if it lay near enough to the edge for the proton to escape the scatterer before depositing its full energy. If the following condition was met

$$x_n^2 + y_n^2 \leq (\texttt{R1} - \Lambda)^2 \tag{4.26}$$

(where $n = 1$ or 2, depending on the value of `NPATH`), then no edge effect was possible for the current event. If this condition was not satisfied, then the intersection point on the scatterer wall from the scattering point and the range of the proton for that particular event were calculated. The range was calculated using an empirical formula for the range of protons in NE102A [Tho88]:

$$\text{Range (in cm)} = 0.0020458\,(E_p + 0.15045)^{1.8194}/1.17. \tag{4.27}$$

If the calculated range was greater than the distance to the scatterer wall, only that percentage of the energy actually deposited in the scatterer was recorded for the event. The proton recoil energy was then given by

$$E_p(\text{corrected}) = E_p(\text{from kinematics}) \times \frac{\text{distance to wall}}{\text{range of proton in NE102A}}. \tag{4.28}$$

These edge effects were flagged so that the magnitude of their effect on the yield could be determined. At $E_n = 7.6$ MeV, edge effects accounted for up to 4% of the single-scattering yield at the most backward angle, where the proton recoil energy was greatest, and were negligible at the most forward angle. At 12 MeV the edge effects accounted for approximately 9% of the single-scattering yield at the most backward angle while accounting for less than 0.2% at the most forward angle. Additionally, flags within the code allowed for only edge effects to be recorded; in this way the proton recoil spectrum of these edge effects could be viewed separately. Fig. 4.5 shows such a spectrum at $E_n = 12$ MeV and $\theta_{\text{lab}} = 32°$. The edge events (solid curve) are a flat background that tails in underneath the elastic peak (dotted curve).

4.5.3 Depolarization

After scattering from a proton, the depolarization of the neutron beam was determined. From this the neutron polarization was adjusted prior to the next scattering process. The scattered neutron polarization, p' was given by [Fai59]

$$p' = \frac{P(\theta) + (\vec{p} \cdot \hat{n})D(\theta)}{1 + (\vec{p} \cdot \hat{n})P(\theta)} \tag{4.29}$$

where $\vec{p}$ is the incident neutron polarization, $\hat{n}$ is the scattering normal, $P(\theta)$ is the polarization that an unpolarized neutron would obtain and $D(\theta)$ is the depolarization. For the case of elastic scattering, $P(\theta) = A_y(\theta)$. As with the np differential cross sections and analyzing powers, the depolarization was determined from the Bonn B phase shifts provided by Machleidt [Mac92] and calculated using Arndt's SAID code [Arn92]. For practical reasons, the depolarization determination was only done for the multiple-scattering from hydrogen

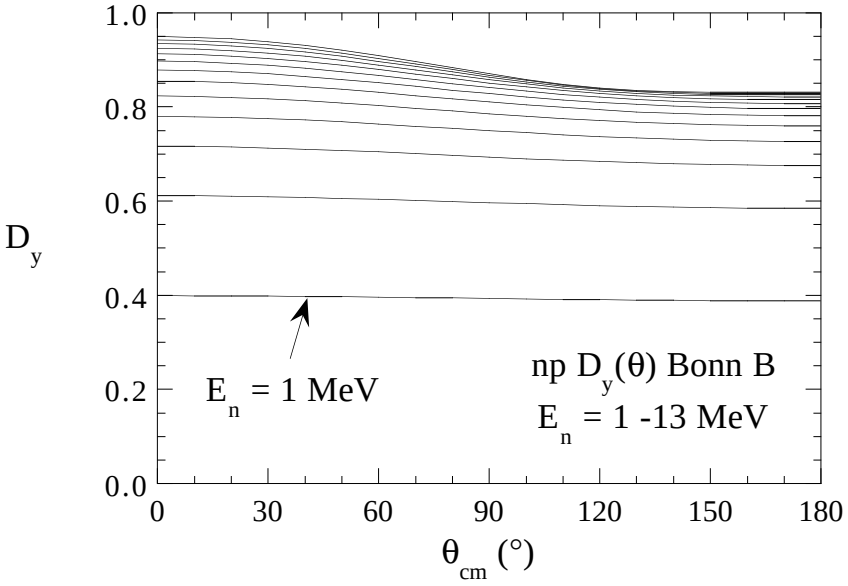

Figure 4.6: Depolarization library for *np* scattering as calculated from Bonn B. Library values are calculated from 1–13 MeV in 1 MeV steps. Phase shifts from Bonn B were used as input to SAID.

within the scatterer (`NPATH` = 2) and in the side-detector multiple-scattering process described below in Sec. 4.6. The effects due to spin rotation are fairly small and have been neglected.

4.5.4 Neutron-Detector Efficiency

Because it is possible for the neutron to interact within the detector, but not deposit its full energy, the neutron detection efficiency of the side detectors was simulated. The neutron detector efficiency was modeled by a simple, empirical formula and used to weight each scattering event within the side detectors. As all neutron detectors used in the experiment were of the same design, it was deemed sufficient to use this approximate efficiency. In the simulation both left and right detectors were identical with respect to efficiency and threshold. The equation used for the neutron detector efficiency was:

$$\text{Efficiency} = 0.7\left(1 - \frac{E_{bias}}{E_n}\right)\ e^{\frac{-E_n}{12}} \tag{4.30}$$

where E_{bias} is the lower-level bias in the neutron side detector and E_n is the incident neutron energy. The value for the bias was taken from the experimental settings and ranged from approximately 0.1–1.2 MeV depending on the energy and angle (see Tables 2.2 and 2.3 for side detector biases).

4.6 Polarization-Dependent Detector Efficiency

One further scattering process of particular interest was a multiple-scattering process that occurred in the side detectors. Due to the large amount of carbon in the NE213 liquid detectors, there is a significant probability for an incoming neutron to scatter first from carbon before scattering from hydrogen and being detected (the neutron must scatter from hydrogen in order to produce enough light to be detected). In fact, approximately 10% of the neutron detection efficiency of these detectors comes from double-scattering first from carbon and then from hydrogen. For polarized neutrons, this double-scattering results in an asymmetry caused by a modification to the detector efficiencies. This effect is referred to as the Polarization-Dependent Detector Efficiency (PDDE) and unlike the normal detector efficiency, this effect *does not cancel with spin flipping.*

The effect results from resonances in the n-^{12}C total cross section. Over the range of energies of interest to the present work, the total n-^{12}C cross section is shown in Fig. 4.7. These resonances can cause dramatic changes in the n-^{12}C analyzing power over very short energy intervals. Fig. 4.8 shows the effect on the analyzing power of one such resonance over the incident neutron energy range 6.25–6.333 MeV (the analyzing powers were calculated from from a phase-shift analysis of cross section data [Tor90]). Due to the finite size of the detectors, neutrons entering the side detectors from the scatterer will have some energy spread as a result of their scattering at slightly different angles. If this energy range contains a n-^{12}C $A_y(\theta)$ resonance, then the left and right detector efficiencies for polarized neutrons will be modified. To illustrate this, Fig. 4.9 shows the case where the scattered neutron energy range covered by the detectors contains one of these resonances. This example

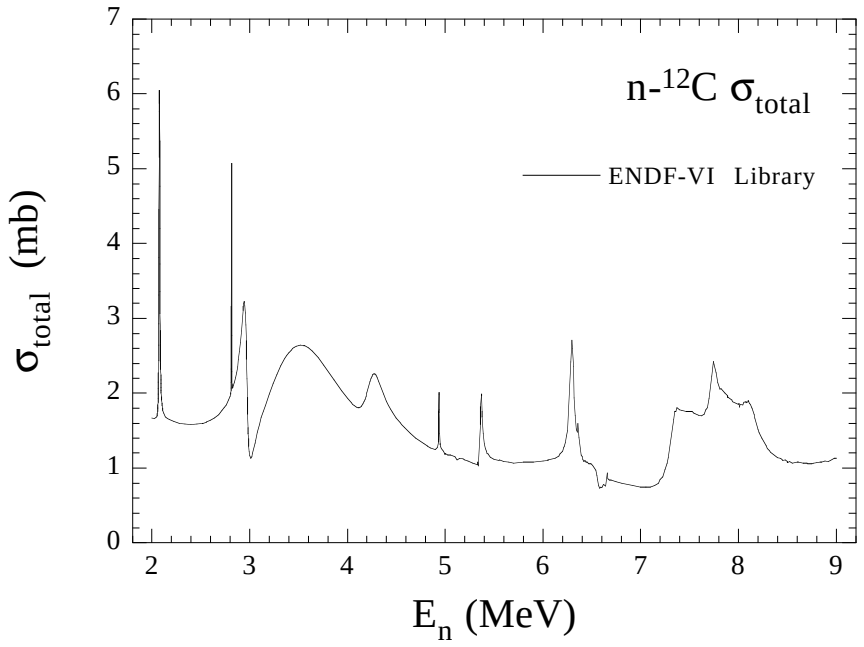

Figure 4.7: Resonances in the total n-^{12}C cross section. Cross section from ENDF-VI Library.

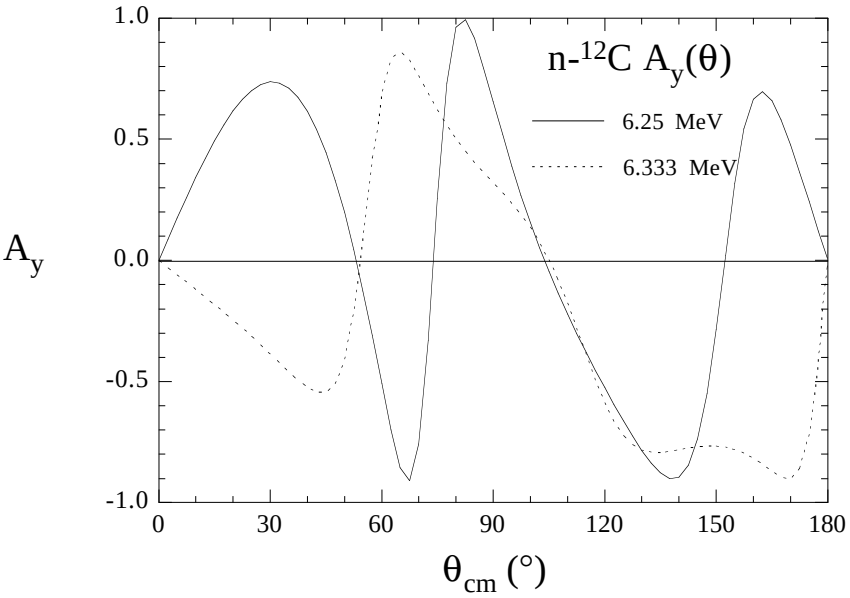

Figure 4.8: Resonance in the n-^{12}C analyzing power. The solid curve shows A_y at $E_n = 6.25$ MeV while the dotted curve is for $E_n = 6.333$ MeV.

assumes that the n-^{12}C analyzing power goes from a large positive value on the low-energy side of the detectors to a large negative value on the high-energy side. The "bow-ties" in the figure represent the relative amounts of polarized neutrons scattered from carbon at each side of a detector. For the spin-up case (upper half of Fig. 4.9) the left detector has a decreased efficiency ($-\delta$) because more neutrons scatter out of the detector before scattering from hydrogen and being detected. For the right detector the effect is reversed; this detector has an increased efficiency ($+\delta$).

When the neutron spin is flipped (lower half of Fig. 4.9) the efficiency enhancements are reversed for the left and right detectors. However, by examining at Eqn. 1.88, it can be seen that this efficiency effect does not cancel. Let δ represent the modification to the detector efficiency and assume that the effect is symmetric for each side. Then for the spin-up case, the yield in the left detector, $N_{L\uparrow}$ is replaced by $N_{L\uparrow} - \delta$. Similarly for the right side $N_{R\uparrow} \rightarrow N_{R\uparrow} + \delta$. For the spin-down case, $N_{L\downarrow} \rightarrow N_{L\downarrow} + \delta$ and $N_{R\downarrow} \rightarrow N_{R\downarrow} - \delta$. When these modified values are substituted into Eqn. 1.88, the result is

$$\alpha = \sqrt{\frac{(N_{L\uparrow} - \delta) \cdot (N_{R\downarrow} - \delta)}{(N_{L\downarrow} + \delta) \cdot (N_{R\uparrow} + \delta)}} \tag{4.31}$$

from which it can be seen that the effect does not cancel.

This effect has been understood for some time; see previous works by Tornow *et al.*[Tor88], Holslin [Hol88] and Weisel [Wei92]. The analysis of Weisel did correct the results for this effect, however, the n-^{12}C analyzing power is not well known in the energy ranges of these experiments. An accurate cross section and analyzing power library is crucial to the accuracy of the correction. Previous works relied mainly on the phase-shift analysis of Galati [Gal72]. For the present work the n-^{12}C cross section and analyzing power libraries used in Weisel's experiment [Tor90] were supplemented with a phase-shift analysis performed by Chen [Che94] at TUNL. The calculations were made in finer steps, particularly for the forward angles ($\theta_{cm} < 60^{\circ}$) where the n-^{12}C cross section is larger by an order of magnitude or more than at the more backward angles.

The calculation was performed similar to the other scattering processes. The PDDE

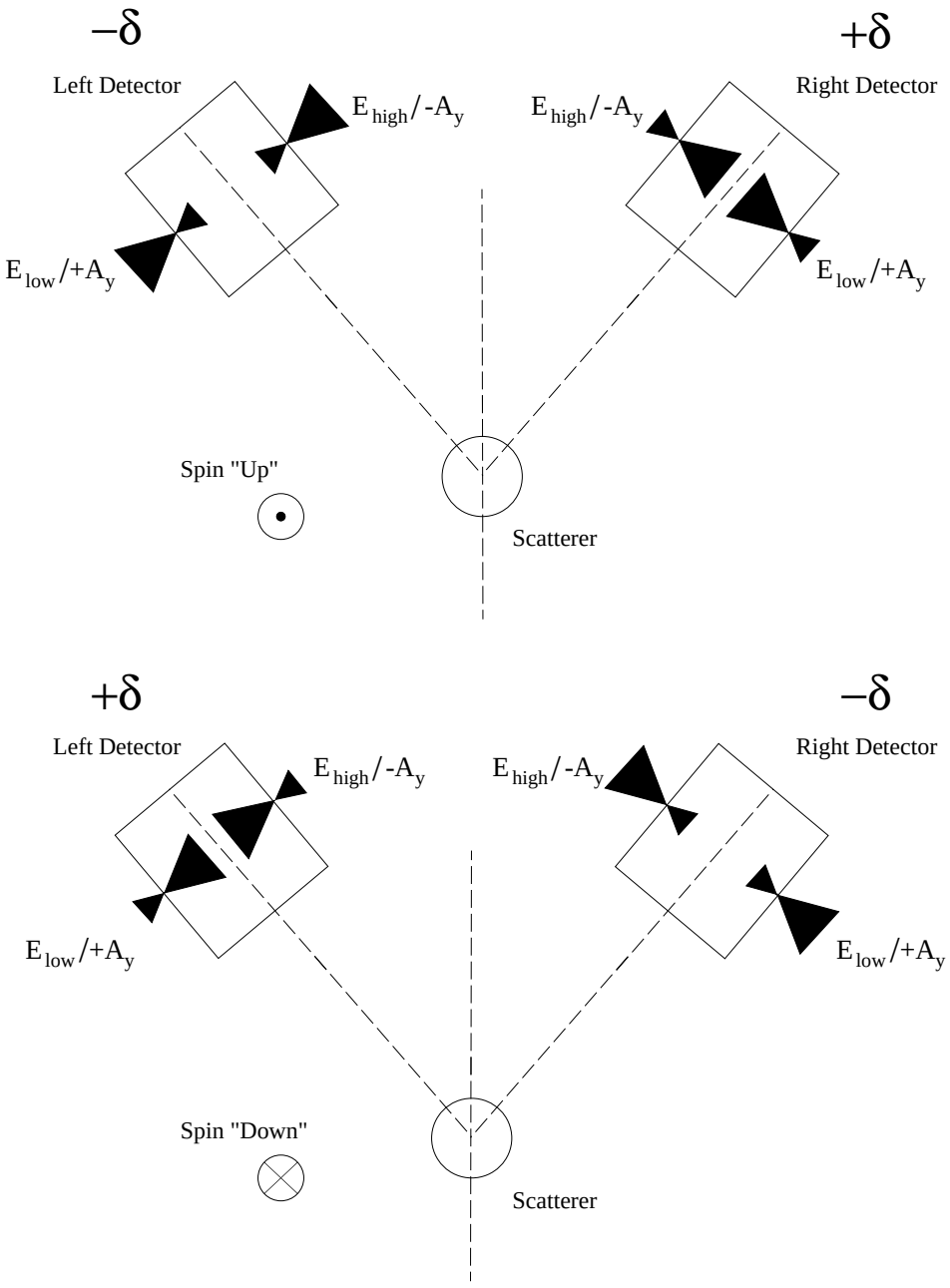

Figure 4.9: Polarization-dependent detector efficiency. The "bow-tie" diagram illustrates the relative amounts of polarized neutrons scattered to each side of the detectors, changing the efficiency for the detectors and giving rise to an asymmetry which does not cancel out.

yields were calculated as a separate process; in the scatterer, only single-scattering from hydrogen was considered. An additional reaction point (`P3C` for the left detector, `P4C` for the right detector) was chosen at random. As was the case with double-scattering in the scatterer, the distance between these points was checked to avoid a large weighting due to the $\frac{1}{r^2}$ dependence. If the second reaction point was within 0.3 cm of the first, it was rejected and a new point chosen.

To determine the contribution of the PDDE effect to the elastic np scattering, the process was calculated two ways. First it was calculated using the actual n-^{12}C analyzing powers to calculate the polarized cross section for the reaction. For the left side detector this was (similar to Eqn. 4.24)

$$\sigma^{lab}(\theta) = U\sigma_0^{cm}(\theta)\ [1 + \vec{p}\cdot\hat{n}\ A_y(\theta)], \tag{4.32}$$

where U is the kinematic conversion factor from the c-m system, σ_0^{cm} is the unpolarized cross section, and $\vec{p}$ is the neutron polarization corrected for depolarization effects (Sec. 4.5.3). Next the calculation was repeated; this time the beam was effectively "unpolarized" by setting the n-^{12}C analyzing powers to zero. The cross section was then just

$$\sigma^{lab}(\theta) = U\sigma_0^{cm}(\theta). \tag{4.33}$$

In both cases the event was also weighted with the attenuation (Sec. 4.5.1), detector volume and detector efficiency (Sec. 4.5.4). The asymmetries from the two calculations were then compared, and the difference between the two was used as the correction to the data (see Sec 4.8).

4.7 The Asymmetry and its Standard Deviation

At the end of each event, the weighting for that event was added to a total weighting, S. After N events randomly sampling the configuration space of the simulation, the total weighting was determined. By repeating this process M times, M different sums, S_1 through

S_M, were determined and from this distribution the most probable sum was calculated

$$\overline{S} = \frac{1}{M}\sum_{k=1}^{M} S_k. \tag{4.34}$$

The standard deviation of this sum, $\overline{S}$, was given by

$$\overline{\Delta S} = \left[\frac{\sum_{k=1}^{M}(S_k - \overline{S})^2}{M(M-1)}\right]^{\frac{1}{2}}. \tag{4.35}$$

In the current simulation typical values used were M=10 and N=300000. As was noted in Sec. 4.3 due to concerns of patterns in the random number generation used, several such calculations were made using different starting random seeds and the results were averaged together in order to achieve the required statistics.

This sum of weights is related to the number of neutrons detected in each of the side detectors. The sum could then be used to calculate the asymmetry for the simulation

$$\varepsilon = \frac{N_L - N_R}{N_L + N_R} \tag{4.36}$$

where N_L is the number of detected neutrons in the left detector and N_R is the number of detected neutrons in the right detector. The uncertainty in this asymmetry is

$$\Delta\varepsilon = \frac{2}{(N_L + N_R)^2}\sqrt{N_L^2(\Delta N_R)^2 + N_R^2(\Delta N_L)^2}, \tag{4.37}$$

where ΔN_L and ΔN_R are the standard deviations in the number of neutrons in each side detector. For the actual asymmetries used to correct the data, gates were set on the simulated proton light spectra as was done with the experimental data, but the error in the calculation was taken from the error calculated above.

4.8 Monte-Carlo Corrections

In addition to the total sum, for each event the neutron TOF, the proton recoil energy and the proton light were stored in a spectrum. The proton recoil light, in particular, was stored in a 512-channel spectrum, which allowed the simulated light output to be

compared directly with the experimental proton recoil spectra. This spectrum used the gates from the experiment to determine a yield from which the asymmetry was determined. This provided a more realistic determination of the np asymmetry than the total sum of the events. Additionally this light spectrum was later used in the analysis to determine the remaining residual background not accounted for by the Monte-Carlo simulation (see Sec. 4.9).

Fig. 4.10 shows the output of the Monte-Carlo simulation for the different scattering processes at $E_n = 12$ MeV and $\theta_{\rm lab} = 36^\circ$. Here the simulated output has been normalized to the data so the relative contribution of the multiple scattering and edge effects can be seen. As seen these processes contribute a very small amount to the total yield as compared to single scattering. But the corrections become important due to the small size of the np analyzing power. The dashed vertical lines in Fig. 4.10 show the extent of the most inclusive gate used in the analysis.

To correct the data for the multiple-scattering effects, the asymmetry for `NPATH` = 1 (single-scattering from hydrogen) was compared to the asymmetry from the sum of all modeled scattering processes (`NPATH` = 1, 2, 31 and 32). The total yield of neutrons in the left-side detector from all scattering processes was then

$$N_L^{(total)} = N_L^{(1)} + N_L^{(2)} + N_L^{(31)} + N_L^{(32)} \tag{4.38}$$

where the superscripts denote the `NPATH` variable. The total yield for the right side was determined similarly. The asymmetry (and then the analyzing power) was calculated for the `NPATH` = 1 case and for the total of all scattering processes

$$\begin{aligned} A_y^{(1)} &= \frac{1}{p_n}\left[\frac{N_L^{(1)} - N_R^{(1)}}{N_L^{(1)} + N_R^{(1)}}\right] \\ A_y^{(total)} &= \frac{1}{p_n}\left[\frac{N_L^{(total)} - N_R^{(total)}}{N_L^{(total)} + N_R^{(total)}}\right] \end{aligned} \tag{4.39}$$

where p_n is the magnitude of the incident neutron polarization in the experiment. The correction for multiple-scattering was determined by subtracting the analyzing power for

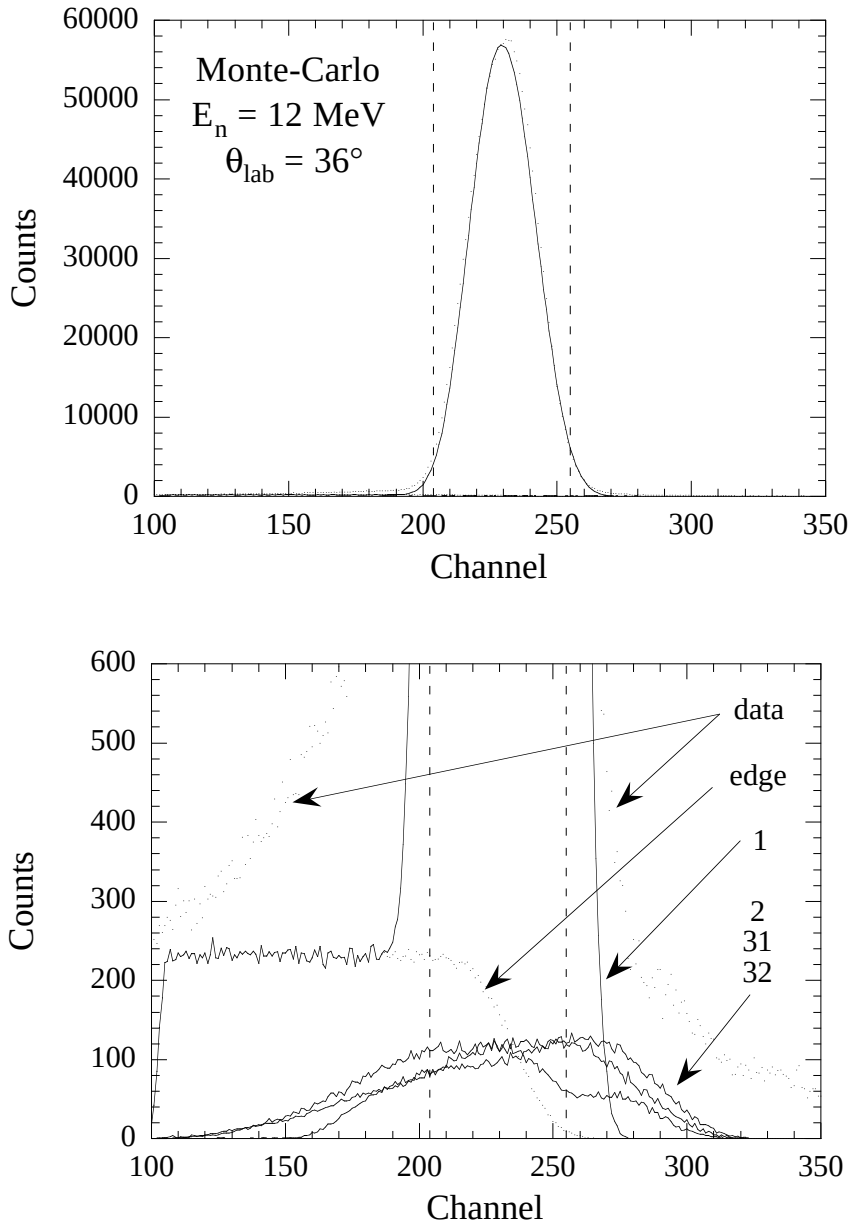

Figure 4.10: Multiple-scattering contributions at $E_n = 12$ MeV and $\theta_{\rm lab} = 36°$. The bottom figure shows an expanded view of the multiple scattering contribution to the total yield. The curve labeled "1" is the single-scattering spectrum, the curve labeled "edge" shows the contribution of edge effects to the single-scattering, and the three curves labeled "2,31,32" are the double-scattering processes. The dashed vertical lines show the limits of the 10% gate used to determine the yield.

the total of all scattering processes from the analyzing power of the single-scattering process

$$\text{Multiple Scattering Correction} = A_y^{(1)} - A_y^{(total)}. \tag{4.40}$$

This difference was then used to correct the experimentally-determined analyzing power. The multiple-scattering corrections for all angles are listed (for $E_n = 7.6$ MeV) in Table 5.2 for the 10% gate, 5.3 for the 30% gate, and 5.4 for the 50% gate. For $E_n = 12$ MeV, the corrections are found in Table 5.5 for the 10% gate, 5.6 for the 30% gate, and 5.7 for the 50% gate.

In order to determine the PDDE correction, the asymmetries were calculated in two ways (as described in Sec. 4.6); once where the polarized cross section was calculated using the true n-^{12}C $A_y(\theta)$ libraries and a second time where only the unpolarized cross section was used (the n-^{12}C$A_y(\theta)$ were set to zero in the code). In this case the correction was given by

$$\begin{aligned} A_y^{(pol)} &= \frac{1}{p_n}\left[\frac{N_L^{(pol)} - N_R^{(pol)}}{N_L^{(pol)} + N_R^{(pol)}}\right] \\ A_y^{(0)} &= \frac{1}{p_n}\left[\frac{N_L^{(0)} - N_R^{(0)}}{N_L^{(0)} + N_R^{(0)}}\right], \end{aligned} \tag{4.41}$$

where $N_L^{(pol)}$ is the left detector yield where the polarized cross section was used to calculate the neutron flux, $N_L^{(0)}$ is the left detector yield where only the unpolarized cross section was used, and similarly for the right side yields. Here p_n is the magnitude of the incident neutron polarization. The PDDE correction was then taken to be the difference between the two analyzing powers

$$\text{PDDE correction} = A_y^{(pol)} - A_y^{(0)}. \tag{4.42}$$

The corrections for the PDDE scattering process are listed in Tables 5.2–5.7 along with the other corrections.

4.9 Remaining Background

The comparison of the measured and calculated spectra showed that there was a remaining background present in all experimental spectra. To estimate this background it was necessary to first subtract all background that could be accounted for from the Monte-Carlo modeling. This was done in the following manner. The ratio of the Monte-Carlo simulation, within each of the three gates, to the data was determined. Then the total multiple-scattering contribution was summed together with the background due to edge effects and this total was normalized by this ratio. This sum was then subtracted from the data. To account for the remaining background, a least-squares fitting routine within the XSYS data analysis package was used to draw a linear background. Two points were chosen from the relatively flat background on the low-energy side of the recoil peak, and two additional points were chosen on the high-energy side. In some case where there was little high-energy tail, these points were essentially zero. A typical fitting and subtraction for $E_n = 12$ MeV and $\theta_{\rm lab} = 36^\circ$ is shown in Fig. 4.11. The dotted curve shown in the figure shows a more accurate fitting of the background; this fit was not used in the analysis due to the difficulty in producing this fit without introducing an additional asymmetry and due the fact that the correction from both background fits shown was essentially the same.

Since the Monte-Carlo simulation did not always accurately model the different gains and alignment of the each side detector, the calculations were shifted by the difference in the centroids of the right and left data peaks. Also the Monte-Carlo simulation was only calculated for a spin-up polarization state. Thus for the the spin-down polarization spectra, the opposite side spectra were used for subtraction, *i.e.*, for the right-side detector, spin-down spectra, the left-side Monte-Carlo spectra were used for subtraction, after being normalized to the right-side spin-down data. Similarly the right-side spin-up was properly normalized and then shifted in order to provide a subtraction for the left-side spin-down data.

A concern with this subtraction was introducing a false asymmetry into the data

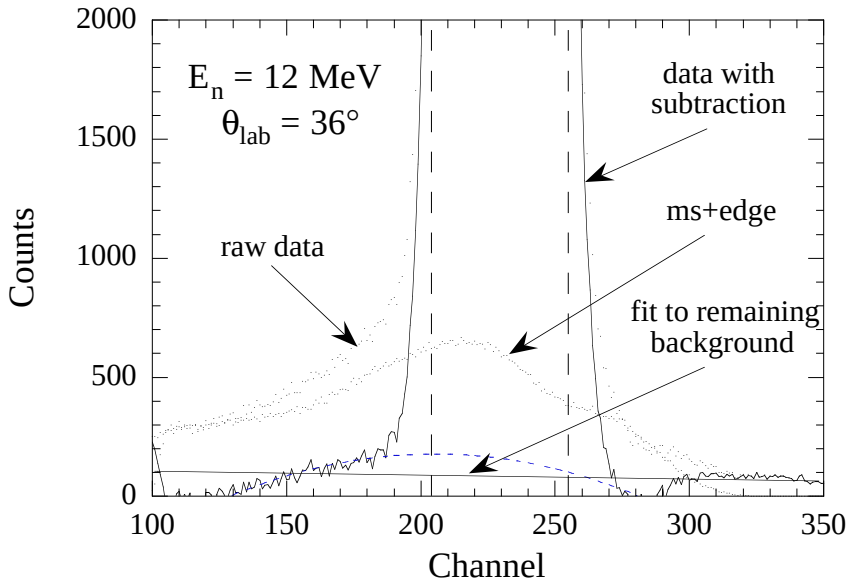

Figure 4.11: Remaining background $E_n = 12$ MeV and $\theta_{\rm lab} = 36°$. The curve labeled "ms+edge" is the sum of all three multiple-scattering processes as well as the single-scattering edge effects. This was normalized to the and then subtracted, the remaining events are shown by the solid curve. A flat background was then fitted to the remaining background using a least-squares fitting routine. The dotted curve shows an alternate choice of remaining background.

from the linear background, which was fitted to a statistically poor sample. It was therefore decided to calculate the backgrounds for each detector and spin state separately, but then to average the results together and then use this value for the remaining background. Remaining background corrections can be found in Tables 5.2–5.7.

Chapter 5

Results & Conclusions

The np $A_y(\theta)$ data measured in the present work are the statistically most accurate and complete angular distributions reported to date. The raw data were measured, in most cases, to a statistical accuracy of $\pm$ 0.0005. Corrections to the data were performed mainly through a Monte-Carlo simulation of the experiment. This simulation modeled the finite-geometry effects of the experiment as well as the effect of various multiple-scattering processes on the data. There were three corrections applied to each data point: a correction for multiple-scattering and finite-geometry effects, as calculated by the Monte-Carlo simulation (Sec. 4.8), a correction for the PDDE multiple-scattering process (Sec. 4.6), also calculated by the Monte-Carlo code, and a remaining background correction determined after subtracting the Monte-Carlo output from the experimental data (Sec. 4.9).

The final results for both energies are tabulated below. The tables show the uncorrected data along with all corrections at each of the three proton-recoil energy gates used in the analysis. The data at E_n = 7.6 MeV are given in Table 5.2 for the 10% gate, Table 5.3 for the 30% gate, and Table 5.4 for the 50% gate. At E_n = 12 MeV the data are given in Table 5.5 for the 10% gate, Table 5.6 for the 30% gate, and Table 5.7 for the 50% gate. The errors shown for the uncorrected data represent the statistical error in the measurements. The errors for the corrected data (in the columns labeled "Total") contain this statistical

error as well as the errors associated with each of the corrections.

The corrections were applied to these data in the following way. For each scattering process and background effect, an analyzing power correction was calculated (see Secs. 4.8 and 4.9), these corrections were then added to the raw analyzing power obtained in the experiment to give a final analyzing power:

$$A_y^{(Final)} = A_y^{(Raw)} + \delta A_y^{(MS)} + \delta A_y^{(PDDE)} + \delta A_y^{(Remain)}, \tag{5.1}$$

where $\delta A_y^{(MS)}$ is the correction for multiple-scattering processes, $\delta A_y^{(PDDE)}$ is the correction for the polarization-dependent detector efficiency effect and $\delta A_y^{(Remain)}$ is the correction for the remaining background. The errors associated with each correction were added in quadrature [Bev69] with the statistical error of the raw data to obtain the final error in the analyzing power:

$$dA_y^{(Final)} = \sqrt{\left[\Delta A_y^{(Raw)}\right]^2 + \left[\Delta\left(\delta A_y^{(MS)}\right)\right]^2 + \left[\Delta\left(\delta A_y^{(PDDE)}\right)\right]^2 + \left[\Delta\left(\delta A_y^{(Remain)}\right)\right]^2}. \tag{5.2}$$

The hope of this work is to provide a means of determining the value of the charged pion coupling constant, $g^2_{\pi^\pm}/4\pi$. As mentioned in Sec. 1.4 the analysis of Machleidt [Mac93] found that the lower value for the neutral pion coupling constant, $g^2_{\pi^o}/4\pi$, seems to be well supported by the Nijmegen phase-shift analysis [Sto93], but that a lower value for the charged coupling constant produces difficulties in reproducing the deuteron bound-state properties. As has been seen, the low-energy neutron-proton analyzing power, $A_y(\theta)$, shows a marked sensitivity to the value of $g^2_{\pi^\pm}/4\pi$, and for our analysis three potential models were provided [Mac96a].

These three potential models are all based on the recent CD-Bonn NN potential model [Mac96b]. These potential models were used to calculate phase shifts at the energies of interest, and these in turn were used as the input to Arndt's SAID code [Arn92] to calculate the analyzing powers. For each of these models, the neutral pion coupling constant was kept constant at $g^2_{\pi^o}/4\pi = 13.6$, but the charged pion coupling constant, $g^2_{\pi^\pm}/4\pi$, was

varied. Model A used a charged pion coupling constant of 13.6 and essentially reproduced the prediction of the Nijmegen phase-shift analysis. Model C used the old, larger value of $g^2_{\pi\pm}/4\pi = 14.4$, consistent with the older models. Finally Model B used a "compromise" value of $g^2_{\pi\pm}/4\pi = 14.0$.

Figs. 5.1 and 5.3 show the uncorrected data at the three gates compared to the predictions of the three theoretical potential models. The choice of curves here is consistent with those of Figs. 1.3 and 1.4 in Sec. 1.4. Model A is shown as a dotted curve, Model B by a solid curve and Model C by a dashed-dotted curve. The error bars shown in Figs. 5.1 and 5.3 reflect only the statistical error in the data. Figs. 5.2 and 5.4 show the corrected analyzing power measurements again compared to the three theoretical predictions. Here all corrections have been applied: the multiple-scattering, the PDDE correction and the remaining background correction. The error bars represent the statistical error of the measurement plus the errors associated with the corrections as calculated by Eqn. 5.2.

The $\pm$ 1.5% scale uncertainty due to the uncertainty in the absolute neutron polarization corresponds to about $\frac{1}{6}$ of the total error bar shown near $\theta_{cm} = 60^\circ$ at 7.6 MeV and to about $\frac{1}{3}$ of the total error bar shown in the same angular range at 12 MeV.

It is obvious from comparing Figs. 5.1 and 5.2 for the 7.6 MeV data and Figs. 5.3 and 5.4 for the 12 MeV data, that the corrections remove much of the scatter seen in the uncorrected data. However, even with the corrections, the data do not have a smooth shape that would be suggested by the theoretical predictions. For example, at $E_n = 12$ MeV it appears that our data point at $\theta_{cm} = 72^\circ$ is overcorrected, while our data point at $\theta_{cm} = 104^\circ$ is not corrected sufficiently to produce a smooth angular distribution. At $E_n = 7.6$ MeV due to the smaller magnitude of the analyzing power and the relatively larger errors, the over and undercorrected data points are even more pronounced.

Except at the forward angles, the largest corrections to the data come from the PDDE corrections. Unfortunately, the accuracy of these corrections is difficult to evaluate. Due to the lack of experimental n-^{12}C $A_y(\theta)$ data, the $A_y(\theta)$ values used for the correc-

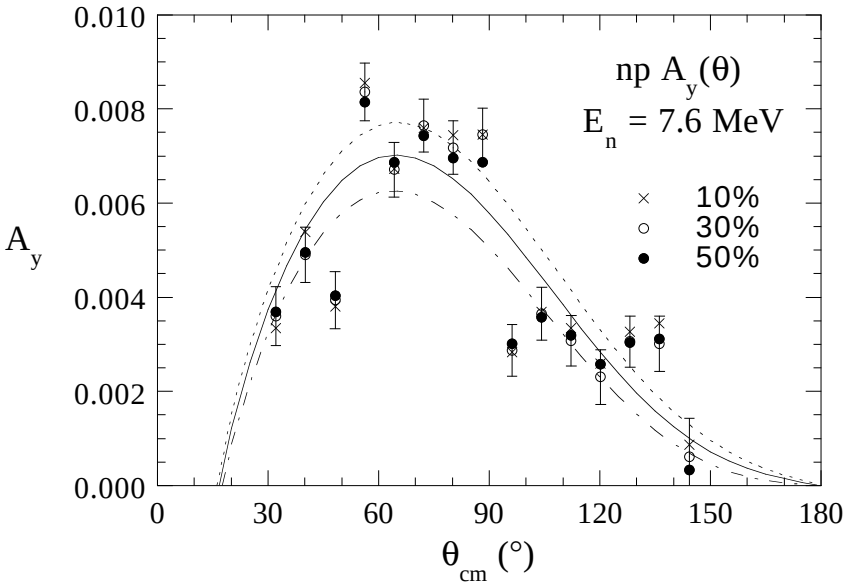

Figure 5.1: Raw data for $E_n = 7.6$ MeV shown with CD-Bonn curves. The neutral pion coupling constant is fixed at 13.6. For the charged coupling constant, the dotted curve uses 13.6 (Model A), the solid curve uses 14.0 (Model B) and the dashed-dotted curve uses 14.4 (Model C).

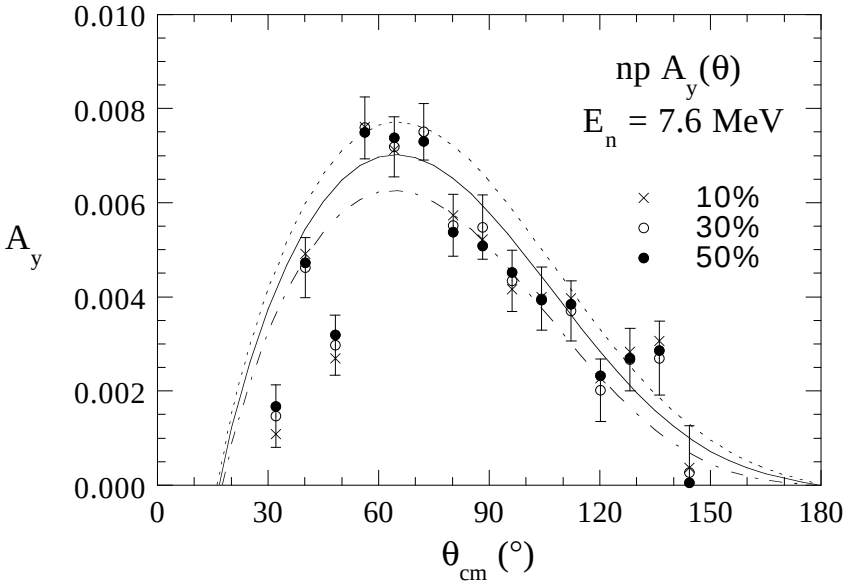

Figure 5.2: Corrected data for $E_n = 7.6$ MeV shown with CD-Bonn curves. The neutral pion coupling constant is fixed at 13.6. For the charged coupling constant, the dotted curve uses 13.6 (Model A), the solid curve uses 14.0 (Model B) and the dashed-dotted curve uses 14.4 (Model C).

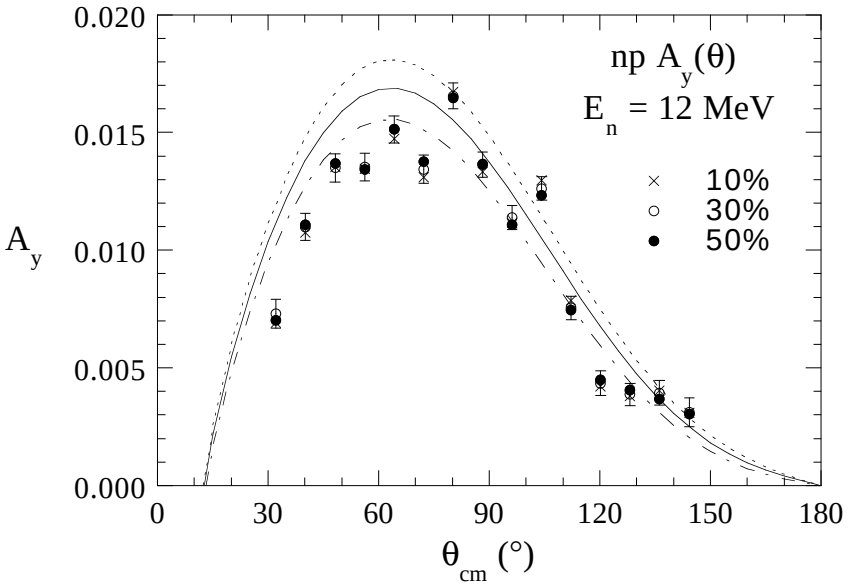

Figure 5.3: Raw data for $E_n = 12$ MeV shown with CD-Bonn curves. The neutral pion coupling constant is fixed at 13.6. For the charged coupling constant, the dotted curve uses 13.6 (Model A), the solid curve uses 14.0 (Model B) and the dashed-dotted curve uses 14.4 (Model C).

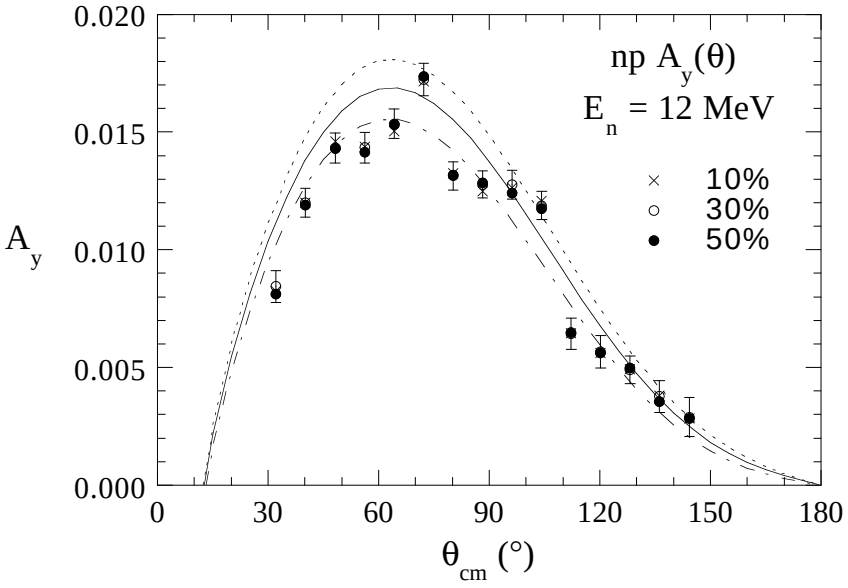

Figure 5.4: Corrected data for $E_n = 12$ MeV shown with CD-Bonn curves. The neutral pion coupling constant is fixed at 13.6. For the charged coupling constant, the dotted curve uses 13.6 (Model A), the solid curve uses 14.0 (Model B) and the dashed-dotted curve uses 14.4 (Model C).

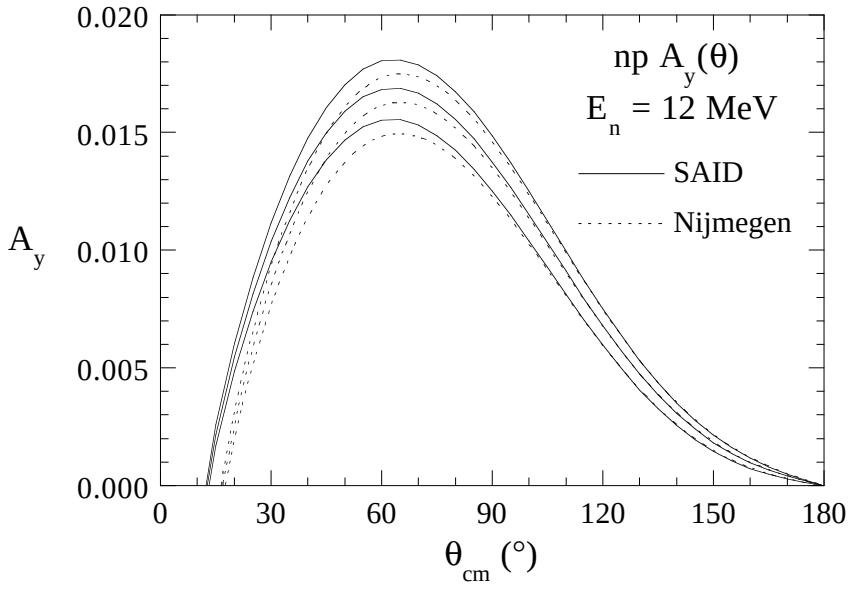

Figure 5.5: Comparison of SAID and Nijmegen predictions from CD-Bonn phase-shifts at $E_n = 12$ MeV. The solid curves are calculations made using SAID while the dotted curves were made using the Nijmegen code. The top two curves use for the charged pion coupling constant 13.6 (Model A), the center two use 14.0 (Model B) and the bottom two use 14.4 (Model C).

tions were obtained from n-^{12}C phase-shift analyses based primarily on cross-section data. Therefore the associated n-^{12}C $A_y(\theta)$ values may not be very accurate. This problem was known to exist before the present work was initiated. The PDDE effect had been discussed in the previous analyses of np $A_y(\theta)$ data by Tornow *et al.* [Tor88] and Holslin *et al.* [Hol88]. However, for the present work, better simulations of the PDDE corrections to the data will soon be available. In the Ph.D. work of Chris Roper, 38 n-^{12}C $A_y(\theta)$ angular distributions were measured in the energy region of interest for the present work [Rop98]. As soon as these data are completely analyzed, a new n-^{12}C phase-shift analysis will be performed to produce accurate n-^{12}C $A_y(\theta)$ values in the angular and energy range relevant to the present work. Only then will we expect to obtain smooth np $A_y(\theta)$ data and only then can one quote a realistic uncertainty to the PDDE corrections and to the final np data.

In the previous figures all theoretical calculations were performed by using the phase-

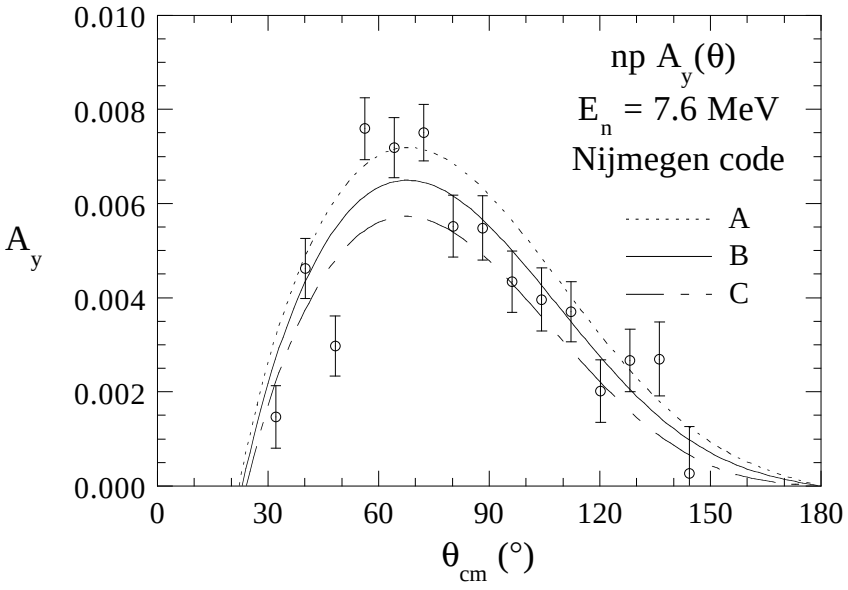

Figure 5.6: Corrected data at $E_n = 7.6$ MeV shown with CD-Bonn curves calculated from Nijmegen code. Models A, B and C refer to charged pion coupling constants of 13.6, 14.0 and 14.4, respectively. Data shown are from 30% gate.

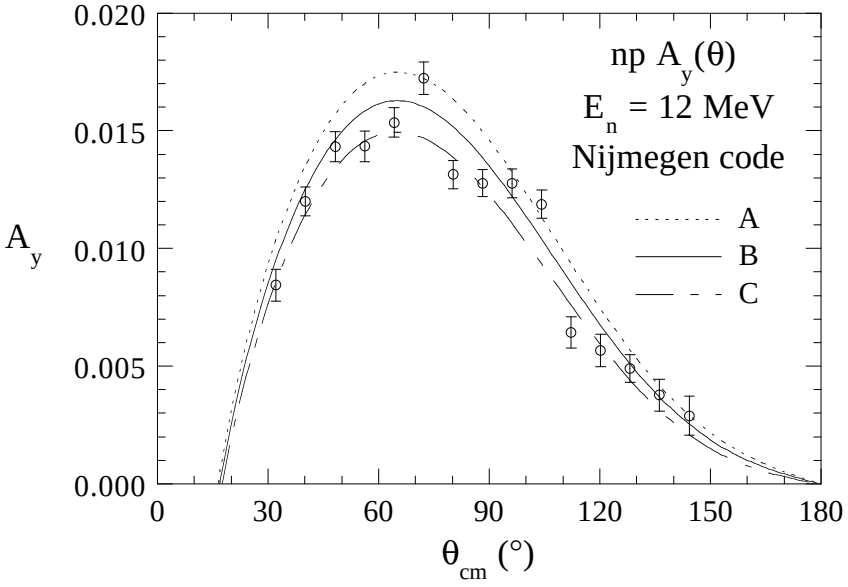

Figure 5.7: Corrected data at $E_n = 12$ MeV shown with CD-Bonn curves calculated from Nijmegen code. Models A, B and C refer to charged pion coupling constants of 13.6, 14.0 and 14.4, respectively. Data shown are from 30% gate.

shifts calculated from the CD-Bonn based potential models as input to the code SAID in order to obtain the analyzing power predictions. During the analysis it came to our attention that our analyzing power data at the very forward angles were not well represented by these calculations. The zero crossing in the np $A_y(\theta)$ at small angles is due to the Mott-Schwinger interaction, which results from the interaction of the neutron magnetic moment in the Coulomb field of the proton. Comparisons of our data with analyzing power predictions from the Nijmegen group suggested that the Nijmegen treatment of this interaction was more accurate than that of SAID. With this in mind, we asked the Nijmegen group [Ren96] to calculate the analyzing powers at $E_n = 7.6$ and 12 MeV using the phase shifts from the three models used in our analysis. A comparison of the predictions at $E_n = 12$ MeV is shown in Fig. 5.5. Here the solid curves represent the predictions of the three models as calculated by SAID, while the dotted curves were calculated using the Nijmegen code. It can be seen that in addition to the different zero-crossing of the analyzing power, the peak values near $\theta_{cm} = 60^\circ$ are somewhat smaller for the analyzing powers calculated with the Nijmegen code.

A comparison of the data to these predictions as calculated using the Nijmegen code can be see in Fig. 5.6 for 7.6 MeV and Fig. 5.7 for 12 MeV. The data shown in both cases are from the 30% gate. It is clear at both energies that the forward-angle data are better reproduced than by the SAID calculations shown in Figs. 5.2 and 5.4. The somewhat smaller peak values of the Nijmegen predictions would also support a somewhat larger value of the charged pion coupling constant.

To judge which model best fit the data, a χ^2 fit of the models to the data was performed. The χ^2 is defined by

$$\chi^2 = \sum_{i=1}^{15} \left[\frac{x_i^{model} - x_i^{exp}}{\Delta x_i^{exp}} \right]^2 , \tag{5.3}$$

where x_i^{model} are the model predictions, x_i^{exp} are the data and Δx_i^{exp} are the errors of the data points. The fit was performed at both energies and the results are shown in Figs. 5.8 and 5.8. Here the total χ^2 of the fit is plotted versus the value of $g_{\pi^\pm}^2/4\pi$ used by each

E_n (MeV)	Model	10%	30%	50%
7.6	A	112.8	89.7	68.3
7.6	B	76.3	57.7	42.8
7.6	C	65.9	49.2	36.8
12	A	231.2	194.1	183.1
12	B	107.6	88.1	83.6
12	C	64.1	52.8	47.5

Table 5.1: χ^2-fit of CD-Bonn models at $E_n = 7.6$ and 12 MeV. Numbers given are total χ^2 as given in Eqn. 5.3. The percentages refer to the different gates used to extract yields from the data.

model. At 7.6 MeV, despite the scatter, the data seem to prefer a larger value of $g^2_{\pi^\pm}/4\pi$ than predicted by the Nijmegen analysis. The smoother data at 12 MeV make an even stronger statement favoring a large value for $g^2_{\pi^\pm}/4\pi$. To test the dependence of the fit on the points where the PDDE effect were large, at 12 MeV, the fit was performed with the following points removed: 36° and 40° and also 52° and 56°. These points deviate significantly from the smooth shape of the analyzing power predicted by theory and resulted from either large or insufficient PDDE corrections. With these points removed, the total χ^2 of the fit improves, but also its minimum still favors the larger value of $g^2_{\pi^\pm}/4\pi$.

The accuracy of the np $A_y(\theta)$ data at $E_n = 7.6$ MeV may turn out to be insufficient to reach a clear-cut conclusion about the charged pion coupling constant. But only the future and final PDDE corrections will verify this statement. However, at $E_n = 12$ MeV, even without the improved PDDE corrections, it is clear from the predictions as calculated using SAID (Fig. 5.4) or using the Nijmegen code (Fig. 5.7) that the $A_y(\theta)$ predicted by Model A, which is based on the new, lower $g^2_{\pi^\pm}/4\pi$ of the Nijmegen analysis, is in contradiction with our data. In fact, the data prefer values between 14.0 and 14.2 for the value of the charged pion coupling constant.

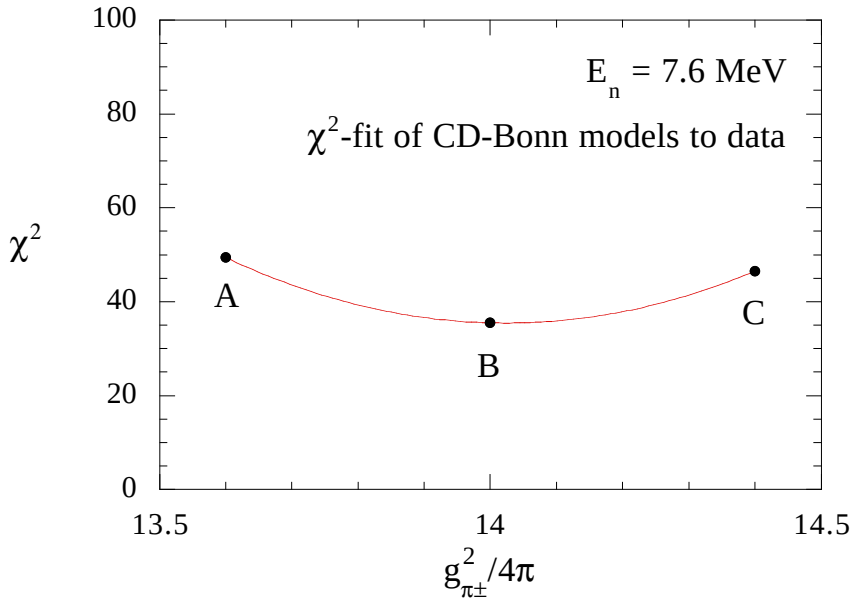

Figure 5.8: χ^2-fit of CD-Bonn models to data at $E_n = 7.6$ MeV. The solid dots are the total χ^2 for each model.

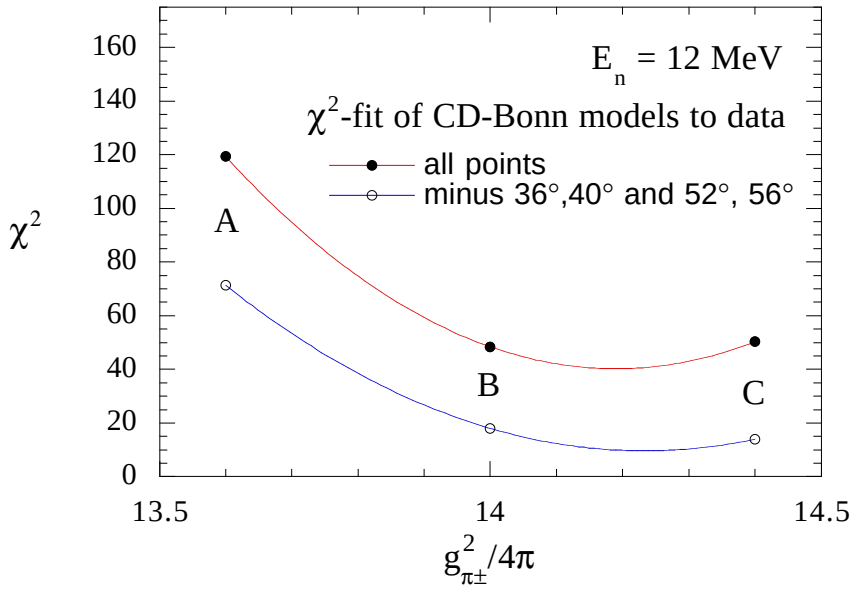

Figure 5.9: χ^2-fit of CD-Bonn models to data at $E_n = 12$ MeV. The solid dots represent the total χ^2 using all 15 data points. The open circles are the total χ^2 with 4 points, where the correction for the PDDE was deemed suspect, removed.

θ_{lab}	θ_{cm}	Raw	Mult. Scatt.	PDDE	Background	Total
16.0	32.1	0.00335 ± 0.00060	-0.00086 ± 0.00011	-0.00145 ± 0.00011	0.00005 ± 0.00000	0.00109 ± 0.00062
20.0	40.1	0.00539 ± 0.00058	-0.00072 ± 0.00013	0.00006 ± 0.00013	0.00018 ± 0.00000	0.00491 ± 0.00061
24.0	48.2	0.00380 ± 0.00057	-0.00088 ± 0.00012	-0.00031 ± 0.00014	0.00009 ± 0.00000	0.00270 ± 0.00060
28.0	56.2	0.00856 ± 0.00059	-0.00086 ± 0.00014	-0.00022 ± 0.00015	0.00013 ± 0.00000	0.00761 ± 0.00062
32.0	64.2	0.00673 ± 0.00054	-0.00082 ± 0.00017	0.00119 ± 0.00016	0.00002 ± 0.00000	0.00712 ± 0.00059
36.0	72.2	0.00759 ± 0.00055	-0.00090 ± 0.00013	0.00066 ± 0.00015	0.00002 ± 0.00000	0.00737 ± 0.00058
40.0	80.2	0.00745 ± 0.00053	-0.00080 ± 0.00022	-0.00097 ± 0.00023	0.00005 ± 0.00000	0.00573 ± 0.00062
44.0	88.2	0.00746 ± 0.00055	-0.00050 ± 0.00021	-0.00178 ± 0.00025	0.00004 ± 0.00000	0.00522 ± 0.00064
48.0	96.2	0.00284 ± 0.00052	-0.00016 ± 0.00025	0.00146 ± 0.00025	0.00002 ± 0.00000	0.00416 ± 0.00063
52.0	104.2	0.00369 ± 0.00054	-0.00002 ± 0.00024	0.00031 ± 0.00025	0.00002 ± 0.00000	0.00400 ± 0.00064
56.0	112.2	0.00335 ± 0.00052	-0.00025 ± 0.00024	0.00085 ± 0.00025	0.00002 ± 0.00000	0.00397 ± 0.00062
60.0	120.2	0.00259 ± 0.00055	-0.00036 ± 0.00017	0.00004 ± 0.00020	0.00000 ± 0.00000	0.00227 ± 0.00061
64.0	128.2	0.00327 ± 0.00052	-0.00038 ± 0.00029	-0.00006 ± 0.00029	0.00000 ± 0.00000	0.00283 ± 0.00066
68.0	136.2	0.00344 ± 0.00057	-0.00028 ± 0.00029	-0.00012 ± 0.00046	0.00002 ± 0.00000	0.00306 ± 0.00079
72.0	144.3	0.00087 ± 0.00077	-0.00034 ± 0.00031	-0.00016 ± 0.00047	0.00000 ± 0.00000	0.00037 ± 0.00095

Table 5.2: Final corrections for $E_n = 7.6$ MeV using 10% cut.

θ_{lab}	θ_{cm}	Raw	Mult. Scatt.	PDDE	Background	Total
16.0	32.1	0.00360 ± 0.00063	-0.00070 ± 0.00014	-0.00146 ± 0.00014	0.00003 ± 0.00000	0.00147 ± 0.00066
20.0	40.1	0.00490 ± 0.00059	-0.00051 ± 0.00019	0.00007 ± 0.00016	0.00016 ± 0.00000	0.00462 ± 0.00064
24.0	48.2	0.00394 ± 0.00060	-0.00073 ± 0.00015	-0.00030 ± 0.00016	0.00007 ± 0.00000	0.00298 ± 0.00064
28.0	56.2	0.00836 ± 0.00061	-0.00069 ± 0.00018	-0.00020 ± 0.00018	0.00012 ± 0.00000	0.00759 ± 0.00066
32.0	64.2	0.00671 ± 0.00058	-0.00069 ± 0.00021	0.00115 ± 0.00018	0.00002 ± 0.00000	0.00719 ± 0.00064
36.0	72.2	0.00765 ± 0.00056	-0.00077 ± 0.00016	0.00061 ± 0.00016	0.00002 ± 0.00000	0.00751 ± 0.00060
40.0	80.2	0.00718 ± 0.00057	-0.00071 ± 0.00023	-0.00098 ± 0.00025	0.00003 ± 0.00000	0.00552 ± 0.00066
44.0	88.2	0.00746 ± 0.00056	-0.00037 ± 0.00027	-0.00163 ± 0.00027	0.00002 ± 0.00000	0.00548 ± 0.00068
48.0	96.2	0.00287 ± 0.00055	-0.00013 ± 0.00024	0.00158 ± 0.00025	0.00002 ± 0.00000	0.00434 ± 0.00065
52.0	104.2	0.00365 ± 0.00056	-0.00003 ± 0.00025	0.00032 ± 0.00027	0.00002 ± 0.00000	0.00396 ± 0.00067
56.0	112.2	0.00308 ± 0.00054	-0.00023 ± 0.00022	0.00085 ± 0.00026	0.00000 ± 0.00000	0.00370 ± 0.00064
60.0	120.2	0.00231 ± 0.00058	-0.00033 ± 0.00022	0.00004 ± 0.00022	0.00000 ± 0.00000	0.00202 ± 0.00066
64.0	128.2	0.00306 ± 0.00054	-0.00032 ± 0.00025	-0.00007 ± 0.00030	0.00000 ± 0.00000	0.00267 ± 0.00067
68.0	136.2	0.00301 ± 0.00059	-0.00021 ± 0.00031	-0.00012 ± 0.00041	0.00002 ± 0.00000	0.00270 ± 0.00078
72.0	144.3	0.00062 ± 0.00081	-0.00021 ± 0.00033	-0.00016 ± 0.00047	0.00002 ± 0.00000	0.00027 ± 0.00099

Table 5.3: Final corrections for $E_n = 7.6$ MeV using 30% cut.

θ_{lab}	θ_{cm}	Raw	Mult. Scatt.	PDDE	Background	Total
16.0	32.1	0.00369 ± 0.00069	-0.00059 ± 0.00027	-0.00146 ± 0.00016	0.00003 ± 0.00000	0.00167 ± 0.00076
20.0	40.1	0.00495 ± 0.00065	-0.00045 ± 0.00027	0.00008 ± 0.00017	0.00014 ± 0.00000	0.00472 ± 0.00072
24.0	48.2	0.00404 ± 0.00064	-0.00064 ± 0.00021	-0.00030 ± 0.00019	0.00009 ± 0.00000	0.00319 ± 0.00070
28.0	56.2	0.00815 ± 0.00064	-0.00059 ± 0.00026	-0.00017 ± 0.00020	0.00010 ± 0.00000	0.00749 ± 0.00072
32.0	64.2	0.00687 ± 0.00060	-0.00062 ± 0.00026	0.00111 ± 0.00021	0.00002 ± 0.00000	0.00738 ± 0.00069
36.0	72.2	0.00743 ± 0.00060	-0.00070 ± 0.00023	0.00055 ± 0.00019	0.00002 ± 0.00000	0.00730 ± 0.00067
40.0	80.2	0.00696 ± 0.00060	-0.00065 ± 0.00029	-0.00097 ± 0.00030	0.00003 ± 0.00000	0.00537 ± 0.00073
44.0	88.2	0.00687 ± 0.00060	-0.00032 ± 0.00025	-0.00151 ± 0.00033	0.00004 ± 0.00000	0.00508 ± 0.00073
48.0	96.2	0.00301 ± 0.00058	-0.00011 ± 0.00027	0.00162 ± 0.00029	0.00000 ± 0.00000	0.00452 ± 0.00070
52.0	104.2	0.00358 ± 0.00060	-0.00001 ± 0.00034	0.00034 ± 0.00032	0.00002 ± 0.00000	0.00393 ± 0.00076
56.0	112.2	0.00319 ± 0.00057	-0.00018 ± 0.00031	0.00084 ± 0.00028	0.00000 ± 0.00000	0.00385 ± 0.00071
60.0	120.2	0.00258 ± 0.00061	-0.00030 ± 0.00025	0.00004 ± 0.00027	0.00000 ± 0.00000	0.00232 ± 0.00071
64.0	128.2	0.00304 ± 0.00058	-0.00027 ± 0.00026	-0.00008 ± 0.00036	0.00000 ± 0.00000	0.00269 ± 0.00073
68.0	136.2	0.00312 ± 0.00064	-0.00014 ± 0.00033	-0.00012 ± 0.00045	0.00000 ± 0.00000	0.00286 ± 0.00085
72.0	144.3	0.00034 ± 0.00089	-0.00014 ± 0.00038	-0.00015 ± 0.00048	0.00000 ± 0.00000	0.00005 ± 0.00108

Table 5.4: Final corrections for $E_n = 7.6$ MeV using 50% cut.

θ_{lab}	θ_{cm}	Raw	Mult. Scatt.	PDDE	Background	Total
16.0	32.1	0.00693 ± 0.00057	0.00115 ± 0.00016	0.00011 ± 0.00015	0.00005 ± 0.00000	0.00824 ± 0.00061
20.0	40.1	0.01074 ± 0.00056	0.00121 ± 0.00013	-0.00013 ± 0.00015	0.00018 ± 0.00000	0.01199 ± 0.00059
24.0	48.2	0.01354 ± 0.00059	0.00098 ± 0.00013	0.00000 ± 0.00014	0.00009 ± 0.00000	0.01461 ± 0.00062
28.0	56.2	0.01346 ± 0.00057	0.00062 ± 0.00013	0.00018 ± 0.00013	0.00013 ± 0.00000	0.01439 ± 0.00060
32.0	64.2	0.01474 ± 0.00053	0.00043 ± 0.00015	-0.00015 ± 0.00016	0.00002 ± 0.00000	0.01503 ± 0.00057
36.0	72.2	0.01311 ± 0.00055	0.00016 ± 0.00021	0.00386 ± 0.00020	0.00002 ± 0.00000	0.01715 ± 0.00062
40.0	80.2	0.01672 ± 0.00054	0.00001 ± 0.00019	-0.00353 ± 0.00013	0.00005 ± 0.00000	0.01325 ± 0.00059
44.0	88.2	0.01334 ± 0.00051	0.00005 ± 0.00016	-0.00095 ± 0.00017	0.00004 ± 0.00000	0.01248 ± 0.00056
48.0	96.2	0.01117 ± 0.00051	-0.00011 ± 0.00019	0.00155 ± 0.00019	0.00002 ± 0.00000	0.01263 ± 0.00058
52.0	104.2	0.01296 ± 0.00049	-0.00016 ± 0.00019	-0.00075 ± 0.00021	0.00002 ± 0.00000	0.01207 ± 0.00057
56.0	112.2	0.00787 ± 0.00048	0.00017 ± 0.00020	-0.00161 ± 0.00029	0.00002 ± 0.00000	0.00645 ± 0.00059
60.0	120.2	0.00421 ± 0.00050	0.00028 ± 0.00022	0.00113 ± 0.00027	0.00000 ± 0.00000	0.00562 ± 0.00061
64.0	128.2	0.00381 ± 0.00043	-0.00006 ± 0.00017	0.00117 ± 0.00024	0.00000 ± 0.00000	0.00492 ± 0.00052
68.0	136.2	0.00403 ± 0.00051	-0.00014 ± 0.00022	-0.00011 ± 0.00035	0.00002 ± 0.00000	0.00380 ± 0.00066
72.0	144.3	0.00309 ± 0.00059	-0.00008 ± 0.00032	-0.00016 ± 0.00045	0.00000 ± 0.00000	0.00285 ± 0.00081

Table 5.5: Final corrections for E_n = 12 MeV using 10% cut.

θ_{lab}	θ_{cm}	Raw	Mult. Scatt.	PDDE	Background	Total
16.0	32.1	0.00730 ± 0.00061	0.00098 ± 0.00022	0.00013 ± 0.00018	0.00003 ± 0.00000	0.00844 ± 0.00067
20.0	40.1	0.01099 ± 0.00058	0.00108 ± 0.00013	-0.00022 ± 0.00015	0.00016 ± 0.00000	0.01201 ± 0.00061
24.0	48.2	0.01350 ± 0.00060	0.00085 ± 0.00011	-0.00009 ± 0.00015	0.00007 ± 0.00000	0.01433 ± 0.00063
28.0	56.2	0.01353 ± 0.00058	0.00051 ± 0.00023	0.00018 ± 0.00014	0.00012 ± 0.00000	0.01434 ± 0.00064
32.0	64.2	0.01513 ± 0.00057	0.00034 ± 0.00022	-0.00014 ± 0.00017	0.00002 ± 0.00000	0.01535 ± 0.00063
36.0	72.2	0.01344 ± 0.00059	0.00013 ± 0.00027	0.00364 ± 0.00021	0.00002 ± 0.00000	0.01723 ± 0.00068
40.0	80.2	0.01655 ± 0.00055	0.00000 ± 0.00023	-0.00344 ± 0.00014	0.00003 ± 0.00000	0.01314 ± 0.00061
44.0	88.2	0.01363 ± 0.00053	0.00006 ± 0.00017	-0.00093 ± 0.00017	0.00002 ± 0.00000	0.01278 ± 0.00058
48.0	96.2	0.01139 ± 0.00052	-0.00009 ± 0.00026	0.00145 ± 0.00021	0.00002 ± 0.00000	0.01277 ± 0.00062
52.0	104.2	0.01262 ± 0.00050	-0.00014 ± 0.00025	-0.00062 ± 0.00022	0.00002 ± 0.00000	0.01188 ± 0.00060
56.0	112.2	0.00755 ± 0.00050	0.00023 ± 0.00030	-0.00135 ± 0.00031	0.00000 ± 0.00000	0.00643 ± 0.00066
60.0	120.2	0.00435 ± 0.00052	0.00021 ± 0.00033	0.00111 ± 0.00028	0.00000 ± 0.00000	0.00567 ± 0.00068
64.0	128.2	0.00388 ± 0.00047	-0.00008 ± 0.00026	0.00110 ± 0.00024	0.00000 ± 0.00000	0.00490 ± 0.00059
68.0	136.2	0.00394 ± 0.00052	-0.00009 ± 0.00024	-0.00010 ± 0.00037	0.00002 ± 0.00000	0.00377 ± 0.00068
72.0	144.3	0.00312 ± 0.00061	-0.00008 ± 0.00034	-0.00016 ± 0.00046	0.00002 ± 0.00000	0.00290 ± 0.00084

Table 5.6: Final corrections for E_n = 12 MeV using 30% cut.

θ_{lab}	θ_{cm}	Raw	Mult. Scatt.	PDDE	Background	Total
16.0	32.1	0.00703 ± 0.00064	0.00088 ± 0.00032	0.00017 ± 0.00019	0.00003 ± 0.00000	0.00811 ± 0.00074
20.0	40.1	0.01108 ± 0.00061	0.00099 ± 0.00022	-0.00031 ± 0.00017	0.00014 ± 0.00000	0.01190 ± 0.00067
24.0	48.2	0.01370 ± 0.00066	0.00071 ± 0.00023	-0.00019 ± 0.00017	0.00009 ± 0.00000	0.01431 ± 0.00072
28.0	56.2	0.01342 ± 0.00062	0.00044 ± 0.00014	0.00018 ± 0.00016	0.00010 ± 0.00000	0.01414 ± 0.00066
32.0	64.2	0.01513 ± 0.00058	0.00032 ± 0.00021	-0.00015 ± 0.00018	0.00002 ± 0.00000	0.01532 ± 0.00064
36.0	72.2	0.01376 ± 0.00061	0.00012 ± 0.00022	0.00346 ± 0.00023	0.00002 ± 0.00000	0.01736 ± 0.00069
40.0	80.2	0.01648 ± 0.00057	0.00000 ± 0.00020	-0.00333 ± 0.00017	0.00003 ± 0.00000	0.01318 ± 0.00063
44.0	88.2	0.01366 ± 0.00054	0.00005 ± 0.00020	-0.00090 ± 0.00017	0.00004 ± 0.00000	0.01285 ± 0.00060
48.0	96.2	0.01109 ± 0.00056	-0.00005 ± 0.00022	0.00137 ± 0.00024	0.00000 ± 0.00000	0.01241 ± 0.00065
52.0	104.2	0.01233 ± 0.00053	-0.00015 ± 0.00026	-0.00045 ± 0.00024	0.00002 ± 0.00000	0.01175 ± 0.00064
56.0	112.2	0.00746 ± 0.00053	0.00023 ± 0.00030	-0.00120 ± 0.00031	0.00000 ± 0.00000	0.00649 ± 0.00068
60.0	120.2	0.00450 ± 0.00056	0.00018 ± 0.00029	0.00095 ± 0.00031	0.00000 ± 0.00000	0.00563 ± 0.00070
64.0	128.2	0.00407 ± 0.00048	-0.00009 ± 0.00034	0.00099 ± 0.00026	0.00000 ± 0.00000	0.00497 ± 0.00064
68.0	136.2	0.00369 ± 0.00056	-0.00007 ± 0.00042	-0.00007 ± 0.00036	0.00000 ± 0.00000	0.00355 ± 0.00079
72.0	144.3	0.00303 ± 0.00066	-0.00006 ± 0.00049	-0.00014 ± 0.00055	0.00000 ± 0.00000	0.00283 ± 0.00099

Table 5.7: Final corrections for $E_n = 12$ MeV using 50% cut.

Bibliography

[Arn90] R. A. Arndt, Z. Li, L. D. Roper, and R. L. Workman. *Determination of the πNN Coupling Constant from Elastic Pion-Nucleon Scattering Data.* Phys. Rev. Letters, **65** (1990) 157–158.

[Arn92] R. A. Arndt. *Phase-Shift Analysis SM92*, 1992. Private Communication.

[Arn94] R. A. Arndt, I. I. Strakovsky, and R. L. Workman. *Update analysis of NN elastic scattering data to 1.6 GeV.* Physical Review C, **50** (1994) 2731–2741.

[Ber87] J. R. Bergervoet, P. C. van Campen, T. A. Rijken, and J. J. de Swart. *Determination of the $pp\pi^0$ Coupling Constant and Breaking of Charge Independence.* Phys. Rev. Letters, **59** (1987) 2255–2258.

[Ber90] J. R. Bergervoet, P. C. van Campen, R. A. M. Klomp, J.-L. de Kok, T. A. Rijken, V. G. J. Stoks, and J. J. de Swart. *Phase shift analysis of all proton-proton scattering data below T_{lab} = 350 MeV.* Physical Review C, **41** (1990) 1435–1452.

[Bev69] P. Bevington. *Data Reduction and Error Analysis for the Physical Sciences.* McGraw-Hill, New York, 1969.

[Bla52a] J. M. Blatt and L. C. Biedenharn. *Neutron-Proton Scattering with Spin-Orbit Coupling I. General Expresssions.* Physical Review, **86** (1952) 399–404.

[Bla52b] J. M. Blatt and L. C. Biedenharn. *The Angular Distribution of Scattering and Reaction Cross Sections.* Reviews of Modern Physics, **24** (1952) 258–272.

[Bla92] T. Black, 1992. TUNL computer code, PRECESS.

[Bow82] J. Bowsher, 1982. TUNL computer code, BABEL.

[Che94] Z. Chen, 1994. Private Communication.

[Cle95a] T. B. Clegg, W. M. Hooke, E. R. Crosson, A. W. Lovette, H. Middleton, H. J. Pfutzner, and K. A. Sweeton. *ECR and Cesium Ionizer Systems for the Triangle Universities Nuclear Laboratory Atomic Beam Polarized Ion Source.* Nuclear Instruments and Methods, **A357** (1995) 212–219.

[Cle95b] T. B. Clegg, H. J. Karwowski, S. K. Lemieux, R. W. Sayer, E. R. Crosson, W. M. Hooke, H. W. Lewis C. R. Howell, A. W. Lovette, H. J. Pfutzner, K. A. Sweeton, and W. S. Wilburn. *A New Atomic Beam Polarized Ion Source for the Triangle Universities Nuclear Laboratory: Overview, Operating Experience, and Performance.* Nuclear Instruments and Methods, **A357** (1995) 200–211.

[Din95] D. C. Dinge, T. B. Clegg, E. R. Crosson, and H. W. Lewis. *RF Transition Systems for the Triangle Universities Nuclear Laboratory Atomic Beam Polarized Ion Source.* Nuclear Instruments and Methods, **A357** (1995) 195–199.

[Dre77] W. Drenckhahn. *Untersuchung der Reaktion* $^{12}C(d,p)^{13}C$ *mit tensorpolarisierten Deuteronen.* Ph.D. thesis, Universität Erlangen-Nürnberg, 1977.

[Eri97] T. E. O. Ericson, B. Loiseau, J. Blomgren, N. Olsson, and J. Rahm. *The* πNN *Coupling Constant from Recent Precise np Charge Exchange Data.* In L. Kok, J. Bacelar, and A. Dieperink, editors, XV^{th} *International IUPAP Conference on Few Body Problems in Physics*, pages 47–48, 1997.

[Fai59] H. Faissner. *Polarisierte Nucleonen.* In S. Flügge and F. Trendelenburg, editors, *Ergebnisse der Exakten Naturwissenchaften*, pages 180–346. Springer-Verlag, Berlin, 1959.

[Gal72] W. Galati, J. D. Brandenberger, and J. L. Weil. *Scattering of Neutrons by Carbon from 3 to 7 MeV.* Physical Review C, **5** (1972) 1508–1529.

[Glo83] Walter Glöckle. *The Quantum Mechanical Few-Body Problem.* Springer-Verlag, Berlin, 1983.

[Gou81] C. R. Gould, L. L. Holzsweig, S. E. King, Y. C. Lau, R. V. Poore, N. R. Roberson, and S. A. Wender. *The XSYS Data Acquisition System at Triangle Unversities Nuclear Laboratory.* IEEE Transactions in Nuclear Science, **NS-28** (1981) 3708–3714.

[Hol88] D. Holslin, J. McAninch, P. A. Quin, and W. Haeberli. *New Test of Nucleon-Nucleon Potential Models.* Phys. Rev. Letters, **61** (1988) 1561–1564.

[Hos68] N. Hoshizaki. *Formalism of Nucleon-Nucleon Scattering.* Supplement of the Progress of theoretical Physics, **42** (1968) 107–159.

[Koc80] R. Koch and E. Pietarinen. *Low-Energy* πN *Partial Wave Analysis.* Nuclear Physics, **A336** (1980) 331–346.

[Kro81] P. Kroll. *Phenomenological Analysis of Nucleon-Nucleon Scattering.* In *Physics Data*, volume 22-1, pages 1–274, Karlsruhe, 1981. Fachinformationszentrum.

[Lac80] M. Lacombe, B. Loiseau, J. M. Richard, R. Vinh Mau, J. Côté, P. Pirès, and R. de Tourreil. *Parametrization of the Paris N-N potential.* Physical Review C, **21** (1980) 861.

[Lis73] H. Liskien and A. Paulsen. *Neutron Production Cross Sections and Energies for the Reactions T(p,n)^{3}He, D(d,n)^{3}He and T(d,n)^{4}He.* Nuclear Data Tables, **A11** (1973).

[Mac87] R. Machleidt, K. Holinde, and C. Elster. *The Bonn Meson-Exchange Model for the Nucleon-Nucleon Interaction.* Physics Reports, **149** (1987).

[Mac89] R. Machleidt. *The Meson Theory of Nuclear Forces and Nuclear Structure.* Advances in Nuclear Physics, **19** (1989) 189–376.

[Mac92] R. Machleidt, 1992. Private Communication.

[Mac93] R. Machleidt and G. Li. *Constraints on the πNN Coupling Constant from the NN System.* π-N Newsletter, **9** (1993) 37.

[Mac96a] R. Machleidt, 1996. Private Communication.

[Mac96b] R. Machleidt, F. Sammarruca, and Y. Song. *Nonlocal nature of the nuclear force and its impact on nuclear structure.* Physical Review C, **53** (1996) 1483–1487.

[Ren96] M. Rentmeester, 1996. Private Communication.

[Rob81a] N. R. Roberson, C. D. Bowman, J. D. Bowman, P. P. J. Delheij, C. M. Frankle, C. R. Gould, D. G. Haase, J. N. Knudson, G. E. Mitchell, R. N. Mortenson, S. I. Penttilä, H. Postma, S. J. Seestrom, J. J. Szymanski, S. A. Wender, S. H. Yoo, V. W. Yuan, and X. Zhu. *An apparatus and techniques of tests for fundamental symmetires in compound-nucleus scattering with epithermal polarized neutron beams.* IEEE Transactions in Nuclear Science, **NS-28** (1981) 3834–3837.

[Rob81b] N. R. Roberson and S. E. Edwards. *Interface for the TUNL VAX Data Acquisition Facility.* IEEE Transactions in Nuclear Science, **NS-28** (1981) 3834–3837.

[Rod90] N. L. Rodning and L. D. Knutson. *Asymptotic D-state to S-state ratio of the deuteron.* Physical Review C, **41** (1990) 898–909.

[Rop98] C. D. Roper, 1998. Private Communication.

[Sta57] H. P. Stapp, T. J. Ypsilantis, and N. Metropolis. *Phase-Shift Analysis of 310 MeV Proton-Proton Scattering Experiments.* Physical Review, **105** (1957) 302–310.

[Sta72] T. Stammbach and R. L. Walter. *R-Matrix Formulation and Phase Shifts for n-^{4}He and p-^{4}He Scattering for Energies up to 20 MeV.* Nuclear Physics, **A180** (1972) 225–240.

[Ste64] J. R. Stehn, M. D. Goldberg, B. A. Magurno, and R. Wiener-Chasman. *Neutron Cross Sections.* BNL 325, **I** (1964).

[Sto88] V. J. G. Stoks, P. C. van Campen, W. Spit, and J. J. de Swart. *Determination of the Residue at the Deuteron Pole in an np Phase-Shift Analysis.* Phys. Rev. Letters, **60** (1988) 1932–1935.

[Sto93] V. J. G. Stoks, R. A. M. Klomp, M. C. M. Rentmeester, and J. J. de Swart. *Partial-wave analysis of all nucleon-nucleon scattering data below 350 MeV.* Physical Review C, **48** (1993) 792–815.

[Tho88] Thorn EMI Gencom Inc., Fairfield, New Jersey. *Nuclear Enterprises Catalog*, 1988. [correction to Dietze (PTB)].

[Tor80] W. Tornow, P. W. Lisowski, R. C. Byrd, and R. L. Walter. *Analyzing Power Measurements for n-p Scattering Between 13.5 and 16.9 MeV.* Nuclear Physics, **A340** (1980) 34.

[Tor88] W. Tornow, C. R. Howell, M. L. Roberts, P. D. Felsher, Z. M. Chen, R. L. Walter, G. Mertens, and I. Šlaus. *Low-energy neutron-proton analyzing power and the new Bonn potential and Paris potential predictions.* Physical Review C, **37** (1988) 2326–2331.

[Tor90] W. Tornow, 1990. Private Communication.

[Tor94] W. Tornow, 1994. Private Communication.

[Vua89] B. Vuaridel, W. Grüebler, V. König, K. Elsener, P. A. Schmelzbach, M. Bittcher, D. Singy, I. Borbérly, M. Bruno, F. Cannata, and M. D'Agostino. *New Constraints on D-State Contributions to the Trinucleon Wave Functions.* Nuclear Physics, **A499** (1989) 429–452.

[Wei92] G. J. Weisel. *Analyzing Power Measurements for Neutron Scattering from ^{1}H and ^{209}Bi.* Ph.D. thesis, Duke University, 1992.

[Wil93] W. S. Wilburn. *Measurement of the Transverse Spin-dependent Total Cross Section Difference $\Delta\sigma_T$ for the Scattering of Polarized Neutrons from Polarized Protons.* Ph.D. thesis, Duke University, 1993.

[Wol52] L. Wolfenstein and J. Ashkin. *Invariance Conditions on the Scattering Amplitudes for Spin $\frac{1}{2}$ Particles.* Physical Review, **85** (1952) 947–949.

[Yuk35] H. Yukawa. *Interactions of Elementary Particles.* Proceeding of the Physico-Mathematical Society of Japan, **17** (1935) 48–57.

Biography

Richard T. Braun

Personal

- Born in Providence, Rhode Island, January 31, 1967

Education

- B.S. Physics, Duke University, Durham, North Carolina, 1989
- A.M. Physics, Duke University, Durham, North Carolina, 1992

Academic Positions

- Teaching Assistant, Duke University, 1989-1991
- Research Assistant, Duke University, 1991-1998

Memberships

- American Physical Society
- Division of Nuclear Physics

Journal Publications

- W. Tornow, R. T. Braun, and H. Witała. *Determination of the Neutron-Neutron Scattering Length a_{nn} from Kinematically Incomplete Neutron-Deuteron Breakup Data Revisited.* Few-Body Systems, **21** (1996) 97–130.
- W. Tornow, R. T. Braun, H. Witała, and N. Koori. *Evidence for large discrepancies between data and calculations for the kinematically incomplete neutron-deuteron breakup reaction.* Physical Review C, **54** (1996) 42–49.

- R. T. Braun, W. Tornow, D. E. González Trotter, C. R. Howell, C. D. Roper, F. Salinas, H. R. Setze, and R. L. Walter. *Neutron-Proton Analyzing Power at 12 MeV and charged πNN Coupling Constant.* In *14$^{\text{th}}$ International IUPAP Conference on Few Body Problems in Physics*, 1994.

- H. R. Setze, C. R. Howell, R. T. Braun, D. E. González Trotter, A. H. Hussein, C. D. Roper, F. Salinas, I. Šlaus, W. Tornow, B. Vlahovic, R. L. Walter, G. Mertens, J. M. Lambert, and H. Witała. *Cross-Section Measurements of the Space-Star Configuration in n-d Breakup at 13.0 MeV.* In *14$^{\text{th}}$ International IUPAP Conference on Few Body Problems in Physics*, 1994.

- C. R. Howell, W. Tornow, H. R. Setze, R. T. Braun, D. E. González Trotter, C. D. Roper, R. S. Pedroni, S. M. Grimes, C. E. Brient, N. Al-Niemi, and F. C. Goeckner. *Resolution of Discrepancy Between Backward Angle Cross-Section Data for Neutron-Deuteron Elastic Scattering.* Few-Body Systems, **16** (1994) 127–142.

- W. Tornow, R. T. Braun, and H. Witała. *Determination of the neutron-neutron scattering length from incomplete neutron-deuteron breakup experiments.* Physics Letters, **B318** (1993) 281–286.

- W. Tornow, C. R. Howell, R. T. Braun, Z. Chen, D. E. González Trotter, C. D. Roper, F. Salinas, H. R. Setze, R. L. Walter, and H. Witała. *Selected topics of the Few-Nucleon Research Program at TUNL.* Few-Body Systems Suppl., **8** (1991) 161.